

**Experimental and Theoretical Description of Two-Way Shape-  
Memory Behavior of Cross-Linked Linear High-Density and  
Short-Chain Branched Polyethylenes**

Dissertation

zur Erlangung des  
Doktorgrades der Ingenieurwissenschaften (Dr.-Ing.)

des

Zentrums für Ingenieurwissenschaften

der Martin-Luther-Universität  
Halle-Wittenberg,

vorgelegt

von Herrn M.Sc. Oleksandr Dolynchuk  
geb. am 14. April 1987 in Ternivka, Ukraine

Gutachter:                   1. Prof. Dr.-Ing. habil. Hans-Joachim Radosch  
                                  2. Prof. Dr.-Ing. Manfred Hermann Wagner

Datum der Verteidigung:   14.09.2015

Halle (Saale)

*This work is dedicated to my beloved Mom and Dad with thanks for always believing in me. All I have and will achieve are only possible due to their unconditional love and sacrifices.*

*The most beautiful thing we can experience is the mysterious. It is the source of all true art and science. He to whom this emotion is a stranger, who can no longer pause to wonder and stand rapt in awe, is as good as dead: his eyes are closed.*

Albert Einstein

## Abstract

Shape-memory polymers are highly innovative smart materials, which permit a number of novel engineering, medical, and pharmaceutical applications. Shape-memory phenomenon in polymers is their ability to fix one or several temporary shapes after application of a quasi-elastic deformation and to recover their original shape when exposed to the external stimuli, such as heat, irradiation, moisture, etc. Only cross-linked crystallizable polymers enabled observing both one-way irreversible and two-way invertible shape-memory effects. Such a unique behavior offers the widest opportunities for using cross-linked semicrystalline shape-memory polymers as thermally triggered actuators and sensors. Furthermore, the theoretical explanation and description of shape-memory effects are in absolute scientific interest as a reliable tool for the prediction and creation of shape-memory polymers with predetermined properties.

The present work attempts to provide a systematical analysis of the two-way shape-memory effect in cross-linked linear high-density polyethylene and ethylene-1-octene copolymers chosen as model objects and characterized by different crystallinity, crosslink density, and crystallization/melting temperatures. The formation of crystal structure and morphology of cross-linked linear and short-chain branched polyethylenes under study during the two-way shape-memory behavior were experimentally analyzed as well.

The theory of two-way shape-memory effect derived in the framework of the present work allowed calculation and detailed analysis of the free energy change of the samples of polyethylenes drawn under constant load and cooled down below crystallization temperature at constant cooling rate. The analysis of the free energy change performed in case of different crosslink density and deformation predicted the possible crystal morphology and orientation of crystallites generated at cooling under load. Experimentally determined crystallinity, type of crystalline structure as well as size and orientation of the crystallites were compared with theoretical predictions got by modeling the two-way shape-memory behavior of linear high-density and short-chain branched polyethylenes. All qualitative and quantitative characteristics of the two-way shape-memory effect, the experimental curves of temperature dependent strain as well as the features of generated crystalline structures are in excellent accordance with the results of theoretical analysis.

### **Acknowledgment**

*First and foremost I would like to express my deepest and sincerest gratitude to my advisor, Prof. Hans-Joachim Radusch, who has supported me throughout my thesis with his fatherly care, patience, and understanding whilst allowing me the room to work in my own way. I greatly appreciate his expertise and immense knowledge as well as thank him for encouraging my research and for allowing me to grow as a research scientist. One could not wish for a better or friendlier advisor.*

*Very special thanks go to Dr. Igor Kolesov, without whose continuous assistance and motivation, too, I would not have accomplished this thesis. Dr. Kolesov is the first who acquainted me with shape-memory phenomena as well as with real science as a whole and welcomed to perform this research. His guidance helped me in all the time of research as well as writing of this thesis. I deeply appreciate his priceless advice on all experiments I carried out. He has become a teacher who truly made a difference in my life.*

*Besides, I am very grateful to Prof. René Androsch for his kind assistance with wide-angle X-ray scattering measurements as well as for valuable discussions of obtained results and of their interpretation.*

*My sincere thanks also go to Prof. Manfred Stamm, Dr. Dieter Jehnichen, Dr. Petr Formánek, and Mrs. Uta Reuter from the Leibniz Institute of Polymer Research Dresden for their interest in my research and an extremely fruitful collaboration. The transmission electron microscopy and small-angle X-ray scattering investigations provided in this work became possible only due to their assistance and goodwill.*

*In addition, I am very grateful to all of my colleagues from the Center of Engineering Sciences at the Martin-Luther-University Halle-Wittenberg for all their kindness and support. Working with them was truly pleasant and enjoyable.*

*Last but not the least, I would like to thank my beloved family and friends for inspiring me, believing in me, and supporting me throughout my entire life. I doubt that I will ever be able to convey my appreciation fully, but I owe them my eternal gratitude.*

*Oleksandr Dolynchuk*



## Table of Contents

List of symbols and abbreviations.....	7
<b>1. Introduction.....</b>	<b>10</b>
<b>2. Literature Review.....</b>	<b>12</b>
2.1. Basics of shape-memory behavior.....	12
2.1.1. Shape-memory alloys.....	12
2.1.2. Shape-memory polymers.....	13
2.2. One-way shape-memory effect in polymeric materials.....	16
2.3. Two-way shape-memory effect in polymeric materials.....	21
2.4. The reversible shape-memory effect in polymeric materials.....	24
2.5. Modeling the shape-memory effect in polymeric materials.....	26
<b>3. Objectives.....</b>	<b>33</b>
<b>4. Molecular and structural based theoretical description of the two-way shape-memory effect.....</b>	<b>35</b>
4.1. The mechanical model.....	35
4.2. Model behavior at cooling below $T_c$ under constant load.....	38
4.2.1. Effect of entangled slipped molecules.....	38
4.2.2. Effect of crystallizing covalent network.....	44
4.2.3. The total strain as a function of temperature.....	54
4.3. Model behavior at heating above $T_m$ under constant load.....	55
<b>5. Investigation and modeling the shape-memory behavior of cross-linked polyethylene and ethylene-copolymers.....</b>	<b>58</b>
5.1. Materials and processing.....	58
5.2. Methods of materials characterization.....	59
5.2.1. Simultaneous DMTA and shape-memory tests under constant load.....	59
5.2.2. Differential scanning calorimetry.....	60
5.2.3. Two-way shape-memory behavior.....	60
5.2.4. Transmission electron microscopy.....	61
5.2.5. Wide- and small-angle X-Ray scattering.....	62
<b>6. Results and discussion.....</b>	<b>64</b>
6.1. Viscoelastic behavior and shape-memory effect under constant load.....	64
6.2. Melting and crystallization behavior of cross-linked polyethylenes.....	66

6.3. Two-way shape-memory behavior.....	68
6.3.1. Effect of loading.....	68
6.3.2. Effect of crosslink density.....	74
6.4. Crystal morphology of cross-linked polyethylenes.....	77
6.5. Crystal orientation.....	79
6.5.1. WAXS of cross-linked polyethylenes.....	79
6.5.1. SAXS of cross-linked polyethylenes.....	83
6.6. Modeling the two-way shape-memory behavior.....	88
6.6.1. Linear high-density and branched polyethylenes.....	88
6.6.2. Influence of loading.....	92
<b>7. Application aspects.....</b>	<b>99</b>
<b>8. Summary.....</b>	<b>103</b>
<b>References.....</b>	<b>106</b>

**List of symbols and abbreviations**

$T_{RT}$	reverse transformation temperature
$T_c$	crystallization temperature
$T_m$	melting temperature
$T_g$	glass transition temperature
$\lambda_0$	wavelength
$R_f$	strain fixity ratio
$R_r$	strain recovery ratio
$\varepsilon$	strain
$\varepsilon_{pr}$	programming strain
$\varepsilon_{rem}$	remaining strain
$\varepsilon_{rec,m}$	residual strain
$T_{pr}$	programming temperature
$T_{sw}$	switching temperature of shape-memory recovery
<b>F</b>	force
$T_m^{max}$	maximum melting temperature
$T_{low}$	the lowest temperature of shape-memory experiment
$T_{sep}$	temperature separating crystals in lower and higher thermally stable
$U$	activation energy of viscous flow
$l_0$	initial length
$\Delta l$	absolute deformation
$\sigma_0$	true stress
$\nu_e$	density of entangled molecules involved in the process of viscous flow
$R$	gas constant
$V_h$	activation volume of viscous flow
$V_m$	volume of flowing molecule
$k_B$	Boltzmann constant
$h$	Planck constant
$\sigma_{0N}$	nominal stress
$\varepsilon_{01}$	part of total strain stored by entangled slipped molecules
$\mathbf{r}_N$	end-to-end vector of a polymer chain
$N$	number of chain links
$b_0$	length of a chain link

$\Delta H_\mu$	enthalpy of fusion per link
$\chi_c$	crystallinity
$T_m^0$	equilibrium melting temperature
$U_{em}$	free energy of the interface between amorphous and crystalline regions
$U_e$	surface free energy of a crystal
$f$	number of crystal folds
$\psi$	number of links in a fold
$\Delta F$	free energy of crystallization
$\mathbf{l}$	crystal vector
$\lambda$	draw ratio
$a_0$	chain thickness
$\zeta$	number of links traversing a crystallite
$T_{sw}^c, T_{sw}^h$	switching temperatures of two-way SME at cooling and heating
$G_0, G_f$	fractions of network chains having 0 and $f$ folds in a crystal
$\nu_c$	crosslink density of covalent polymer network
$\alpha_c, \alpha_a$	linear expansion coefficients of the crystalline and amorphous phases
$\bar{M}_w$	mass-average molecular mass
$E'$	storage modulus
$c_p(T)$	apparent specific heat capacity as a function of temperature
$\varepsilon_{ini}$	initial strain
$\varepsilon_{cr}$	creep strain
$\Delta\varepsilon_{inc}, \Delta\varepsilon_{dec}$	strain increment and strain decrement
$I$	intensity
$q$	scattering vector
$\chi$	azimuthal angle
$\gamma_{eff}$	two-way shape-memory effectiveness factor
$\gamma_{rec}$	two-way shape-memory recovery factor
$W_{sp}$	specific work
$ d\varepsilon/dt _{max}^c$	strain rate peak at cooling
$ d\varepsilon/dt _{max}^h$	strain rate peak at heating
$L$	long period
$a, b, c$	axes of the unit cell
$d(hkl)$	interplanar spacing between neighboring $(hkl)$ -planes

$\varphi_{hkl,Z}$	angle between the normal of the $(hkl)$ -plane and stretch direction $Z$
$e_a, e_b$	cosines of the angles between the unit vector normal to the $(hk0)$ -plane and the $a$ -axis or $b$ -axis
$\varphi_{a,Z}, \varphi_{b,Z}, \varphi_{c,Z}$	angles between axes $a, b, c$ of the unit cell and stretch direction $Z$
$L_c, L_a$	thicknesses of crystalline and amorphous sublayers
$\Theta_{rel}$	relative orientation degree
SME	shape-memory effect
HDPE	high-density polyethylene
EOC/EOCs	ethylene-1-octene copolymer/copolymers
PE/PEs	polyethylene/polyethylenes
MSP	multi-step programming
OSP	one-step programming
PCL	poly( $\epsilon$ -caprolactone)
TOR	trans-polyoctenamer
PVAc	poly(vinyl acetate)
PLA	poly(lactic acid)
PDA	polydopamin
PPD	poly( $\omega$ -pentadecalactone)
EOC30	ethylene-1-octene copolymer with 30 hexyl branches per 1000 C
EOC60	ethylene-1-octene copolymer with 60 hexyl branches per 1000 C
DHBP	2,5-bis(t-butylperoxy)-2,5-dimethylhexane
MFI	melt-flow index
DMTA	dynamic-mechanical thermal analysis
DSC	differential scanning calorimetry
PTFE	polytetrafluoroethylene
ATHAS	advanced thermal analysis system
TEM	transmission electron microscopy
WAXS	wide-angle X-Ray scattering
SAXS	small-angle X-Ray scattering
FWHM	full width at half maximum
CPU	central processing unit

## 1. Introduction

The first research in the field of polymeric shape-memory materials has been known since 1984 [1]. But actual intensive investigation of the shape-memory effect (SME) in polymers began only in the early 2000s from the works of Lendlein and coworkers [2]. Basically, polymer materials show SME if they can be deformed and fixed into a temporary shape and recover their original permanent shape on exposure to external stimuli like heat, light, moisture, electric and magnetic fields. The main preconditions for observing the thermally initiated SME in polymers are the existence of a stable physical or covalent network and a thermal transition, e.g. glass transition or melting, which serves as switching mechanism in shape-memory recovery. The rapid development of the shape-memory phenomenon along with achievements in understanding the basic principles of its reproduction led to discovery of numerous polymers and polymer-based systems showing shape-memory properties. This enabled a myriad of potential applications for shape-memory polymers, such as space self-deploying systems, smart textiles, self-repairing auto bodies, heat-shrinkable tubes and films, biosensors, stents and microtubing for therapeutic actuators, self-healing, etc. [3]

The cross-linked crystallizable polymers attract particular attention regarding their applications as shape-memory materials, since they also reveal the two-way invertible SME in contrast to amorphous polymers demonstrating only the one-way irreversible shape-memory behavior. Polyethylene is considered to be very promising shape-memory material in this connection because of its suitable thermal and mechanical properties, low costs, highly developed industrial production, uncomplicated processing and cross-linking. Furthermore, a simple chemical structure along with abundant knowledge of the relevant material constants of polyethylene make it the model object to study an effect of both programming parameters and structural peculiarities on the shape-memory performance. Only deep understanding the physical background of SME can ensure reliable and successful applications of polymeric shape-memory materials.

The thesis contains comprehensive study of the two-way invertible SME in linear high-density polyethylene (HDPE) and ethylene-1-octene copolymers (EOCs) having different number of short branches. A separate chapter deals with theoretical description and explanation of two-way invertible SME in cross-linked crystallizable polymers. Up to now theoretical approaches to describe shape-memory phenomenon in polymers were rather based on the constitutive mechanical modeling and usually did not comprise sufficient physical

substantiation, while introduced parameters were meaningless. The thesis focuses on the physically grounded modeling, which takes into account main peculiarities of cross-linked semicrystalline polymers as shape-memory materials. The crystallization/melting of covalent polymer network and viscoelastic flow of entangled macromolecules are considered to be two basic mechanisms involved in the shape-memory behavior. Though the crystallizable covalent network is assumed to play a key role in shape-memory phenomena, the effect of viscoelastic deformation of entangled molecules on the shape-memory performance has to be also accounted to provide precise modeling the thermo-mechanical response of real materials. The theoretical consideration aims not only to get a good accordance between fitting and experimental curves of the temperature dependent strain obtained during two-way SME. The proper theoretical analysis has to enable consistent description of the essential characteristics of the crystalline structure generated during the two-way shape-memory behavior of crystallizable polymer networks.

The experimental determination of an influence of loading and crosslink density on the two-way shape-memory performance of linear high-density and short-chain branched polyethylenes (PEs) possessing different crystallinity, crystallization and melting temperatures, and stiffness is a special focus of the present work. Besides, the thesis aims the experimental evaluation of crystallinity, crystal morphology, size and orientation of the crystallites formed during the two-way shape-memory behavior of cross-linked PEs. Deep understanding the aforementioned characteristics of the crystals generated in the course of the two-way shape-memory behavior is a key issue to tailor the shape-memory properties to requirements. Moreover, the comparison between predicted and empirically obtained characteristics of the crystalline structure of PEs allows thorough verification of the theory of the two-way SME derived in the framework of the present study. Finally, adequate and reliable theoretical description of the shape-memory behavior enables a prediction of ways to create the shape-memory polymeric materials with desired properties.

## 2. Literature Review

### 2.1. Basics of shape-memory behavior

#### 2.1.1. Shape-memory alloys

SME was first found for Au–47.5 at% Cd alloy by Ölander in 1932 [4] and later developed by Chang and Read in 1951 [5]. The progress in the material base led to discovery of many metallic alloys revealing shape-memory properties thereafter. The most popular shape-memory alloy nowadays is Ti–Ni, also known as *Nitinol*, which was discovered by Buehler in 1963 [6]. Because of the peculiar feature in remembering the original shape, the shape-memory alloys are being used as various actuators in electric appliances, pipe couplings, automobile applications, medical implants and guidewires, etc. [7].

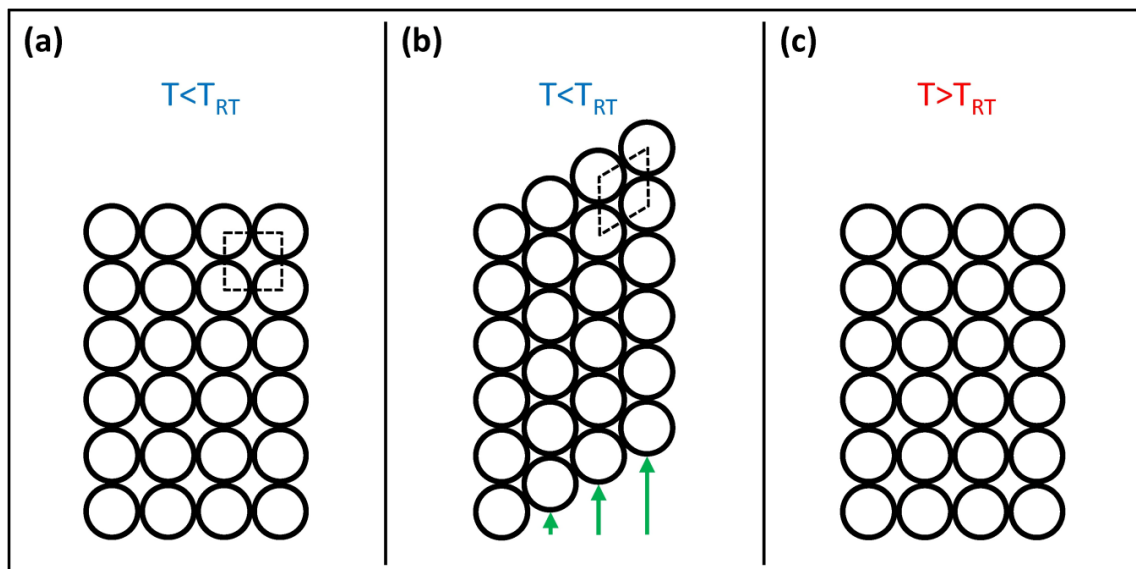


**Figure 1:** Schematic representation of the parent phase (a,c) and the martensite (b) induced by shear (green arrows). Heating above the reverse transformation temperature  $T_{RT}$  initiates the reverse transformation to the parent phase (c) [7].

The shape-memory behavior of a metallic alloy means its deformation to the temporary shape and a recovery of the original shape at heating to a critical temperature designated as the reverse transformation temperature  $T_{RT}$ . Recoverable shape changing in metallic alloys is based on the martensitic transformation, which is a diffusionless displacive phase transition



[7]. The martensitic transformation occurs due to the cooperative movement of atoms induced by different types of deformation like shear, stretching, bending. Figure 1 shows schematically the position of atoms in the parent phase (Figure 1a,c) and in the martensite (Figure 1b) induced by a shear-like deformation with a direction pointed by green arrows in Figure 1b. Generally, the parent phase is a cubic high-temperature phase, whereas the martensite is a low-temperature phase and has a lower symmetry. The dashed square and parallelogram in Figure 1a and 1b illustrates a difference of the symmetries of the parent phase and the martensite, respectively. Besides, depending on a type and direction of deformation, different variants of the martensite with different symmetries can be formed from the same cubic parent phase.

As illustrated in Figure 1, at the temperature below  $T_{RT}$  the shear initiates the martensitic transformation (Figure 1b) and, correspondingly, an alloy is deformed into a temporary shape. Thus, the martensitic transformation is a principal mechanism of shape fixing in shape-memory alloys. If the temperature is higher  $T_{RT}$ , the martensite becomes unstable and reverts to the parent phase in the original orientation (Figure 1c) that provides the recovery of an alloy to an initial permanent shape. So, shape-memory recovery in metallic alloys occurs due to the cooperative movement of atoms, and even though the single relative atomic displacement is small in comparison with inter-atomic distance, a macroscopic shape changing appears [7].

However, the maximal recoverable deformation in shape-memory alloys is still limited to only 10-11% in case of a deformation below  $T_{RT}$ . Furthermore, a relative expensiveness and scantiness of the components prevent the shape-memory alloys to be widely used for everyday applications.

### **2.1.2. Shape-memory polymers**

In the last decades SME in polymeric materials was the research object of many original papers and reviews [3,8–15]. To reveal SME polymers should possess a covalently cross-linked or a stable physical network and the switching mechanism is required. The latter provides the fixation of a temporary shape as well as releases entropic forces stored in a network, whereby the shape recovery proceeds. The switching mechanism can be crystallization/melting, the glass transition, and the formation/cleavage of chemical bonds. The main types of stimuli able to trigger shape changing of polymeric materials are heat, electric and magnetic fields, light, moisture [3,9–13,15].

The mechanism underlying the shape fixing and shape recovery induced by temperature

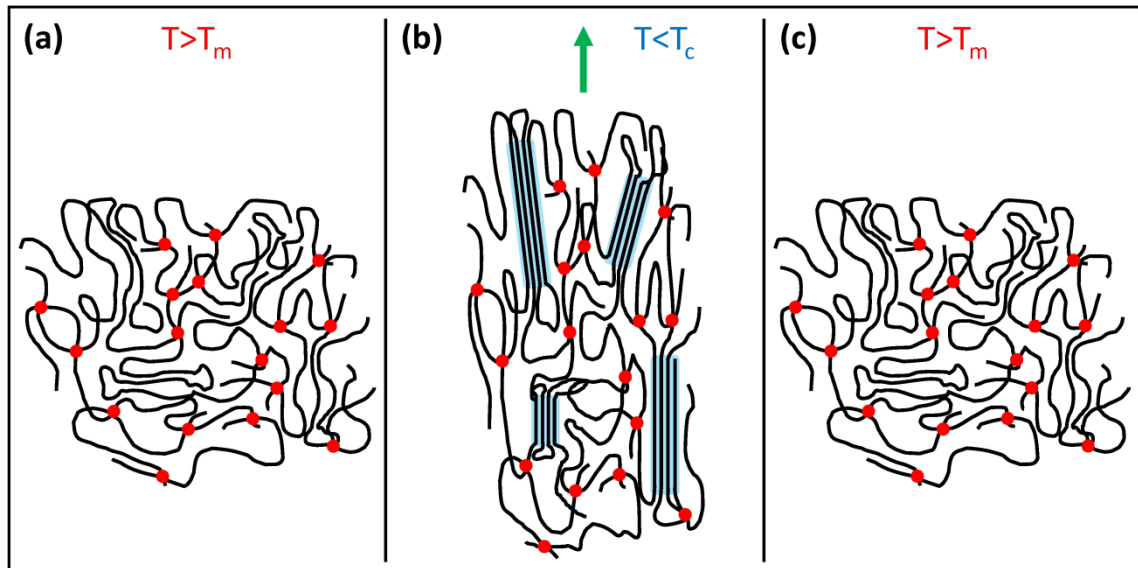


**Figure 2:** Molecular mechanism of fixing the temporary shape (b) at cooling below crystallization temperature  $T_c$  and a recovery of the initial permanent shape (c) at heating above melting point  $T_m$  in crystallizable covalent polymer network. Green arrow in (b) indicates the direction of deformation to the temporary shape, red points represent the crosslink points [14].

variation in a crystallizable covalent network is schematically shown in Figure 2. As the temperature is raised above melting point  $T_m$ , the covalent network is totally amorphous and comprises no crystals. Applying the deformation produces the entropic elastic forces driving to recover nonperturbed undeformed state. The cooling of deformed covalent network below crystallization temperature  $T_c$  results in forming crystals, which store the entropic driving forces. Thus, crystallization provides fixing the temporary shape (Figure 2b). Upon subsequent heating of unconstrained covalent network above  $T_m$  crystals melt releasing stored entropic forces, which act to restore the initial state of the network and to recover the permanent shape of a polymer (Figure 2c). The glass transition in amorphous networks plays the same role as crystallization/melting being considered as the switching mechanism of SME. The cooling and heating of the amorphous network below and above glass transition temperature  $T_g$ , respectively, trigger the cooperative segmental mobility of the network chains. Thereby the elastic forces can be stored and released enabling shape changing of a polymer.

Besides, triggering the shape recovery on exposure to electric and magnetic fields is based on Joule heating of polymer composites consisting of electro-conductive and magneto-inductive particles like carbon nanotubes [16–18] and iron(III)oxide cores [19–21], respectively, incorporated into amorphous or semicrystalline polymer matrix. Hence, an application of electromagnetic field results eventually in the indirect thermally induced SME. Note that the usage of carbon nanotubes, magnetite particles or other hard fillers significantly increases the storage modulus as compared to pure polymer matrix [14].

In the meantime, the shape-memory behavior of polymeric materials can be also realized without any temperature effect. As reported by Lendlein *et al.* [22], the incorporation of photoresponsive molecular switches such as cinnamic acid or cinnamylidene acetic acid into a permanent covalent polymer network enables shape fixing and shape recovery of such polymeric system when exposed to light at room temperature. Namely, deformed polymer is irradiated with ultraviolet light of wavelength  $\lambda_0 > 260$  nm that initiates the formation of covalent bonds between photosensitive functional groups and, correspondingly, fixes deformed polymer network chains in their uncoiled conformation. Upon subsequent ultraviolet irradiation of  $\lambda_0 < 260$  nm, the covalent bonds created within the photoresponsive groups are reversibly cleaved and the system recovers its permanent shape. So, the switching mechanism in this case has a fully chemical nature.

In addition, the shape-memory behavior can be observed upon immersing the amorphous polymers, mostly polyurethanes, in solvents like water, ethanol, etc. [15,23–27]. Basically, solvent diffusion into programmed polymer sample results in the cleavage of hydrogen bonds, whereby a solvent acts as a plasticizer and causes lowering the glass transition temperature below ambient temperature. This enables softening of the amorphous polymer due to the glass transition and induces the shape recovery. Though the glass transition here is considered to be the switching mechanism in shape changing, the plasticizing effect of a solvent plays a primary role, therefore the origin of such shape-memory phenomenon is rather chemical [15]. Note that lowering the glass transition temperature depends on the solvent uptake, which strictly correlates with the immersion time. Thereby the kinetics of shape changing can be heavily altered in this case.

Thus, depending on the origin of external stimuli the shape-memory polymeric materials can be classified in the thermo-, photo-, and chemo-responsive groups. In majority of publications, which consider shape-memory behavior of polymers and polymer-based systems, the subject of investigation is thermo-responsive polymeric materials. According to the availability of thermal transitions in relevant temperature ranges, and to the existence of

stable crosslink points or entanglements within thermo-responsive polymeric materials, they can be divided into following pairs – amorphous and crystallizable polymer systems, in which glass transition or melting/crystallization is responsible for the switching mechanism, as well as covalent and physical polymer networks, respectively. The most research activities in the field of shape-memory polymeric materials are focused on uniform and heterogeneous covalent networks on the basis of crystallizable polymers, because just crystallizable polymer networks in addition to one-way irreversible SME enable producing also two-way invertible SME, in contrast to amorphous polymer networks where glass transition serves as the switching mechanism.

## **2.2. One-way shape-memory effect in polymeric materials**

One-way irreversible SME arises predominantly from thermal triggering of recovery of pre-deformed shape-memory polymeric material occurred at temperature in the range of such thermal phenomenon as melting or glass transition, i.e. being a thermally induced SME. The remarkable appearance of thermally induced one-way SME is realizable for polymeric materials, which possess either a stable covalent or a physical network (entanglements or block-copolymer domains) and reveal at least one of the mentioned thermal transitions.

The main stages of one-way irreversible SME are shown in diagram in Figure 3. The initial (*permanent*) shape can be transferred to the *temporary* shape by means of deformation (e.g. stretching) of a specimen at the programming temperature  $T_{pr}$  above melting or glass transition temperature (step 1 in Figure 3) depending on shape-memory polymer type. Formation of crystalline structure or vitrification during the subsequent cooling (step 2 in Figure 3) under constant load fixes this *temporary* shape so well that it remains nearly unchanged also after unloading of a sample at low (room) temperature (step 3 in Figure 3). The entropy-elastic and viscoelastic forces originate from deformation in a rubber-elastic state and are stored inside the *temporary* shaped sample during its cooling to temperature below crystallization or glass transition point. Described procedure is referred to *programming* and is necessary for the observation of one-way SME. *Programming* can be performed either at constant strain or at constant loading force. Programmed samples keep their *temporary* shape until temperature is below their glass transition or melting temperatures ( $T_g$  or  $T_m$ ), which are usually higher than room temperature [3,8–12].

At heating of programmed samples the stored entropic and viscoelastic forces serve as the driving force of a recovery of the *temporary* shape back to the *permanent* (initial) shape,

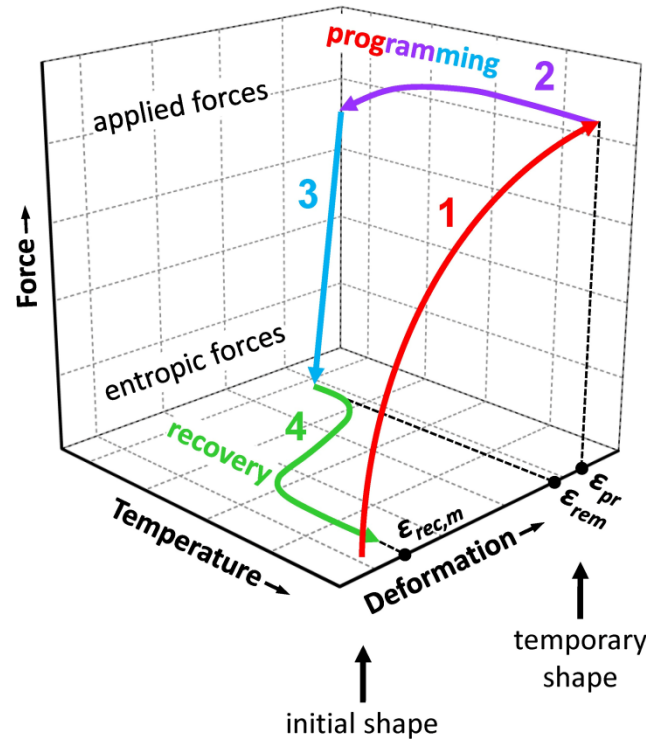


**Figure 3:** The main stages of thermally induced one-way SME in polymeric materials: 1) deformation to the temporary shape at temperature above  $T_g$  or  $T_m$ ; 2) cooling in deformed state below  $T_g$  or  $T_c$ ; 3) unloading at the lowest temperature; 4) unconstrained thermally induced recovery of the initial shape.

whereas the melting or glass transition fulfills the function of triggering or switching mechanism [3,8–12] as shown schematically in Figure 3 (step 4). To repeat such shape-memory behavior, the *programming* step is needed again; therefore, this phenomenon is called one-way *irreversible* SME.

The ability of shape-memory polymer to fix the *temporary* shape and to restore the *permanent* (initial) shape are characterized by the strain fixity ratio  $R_f$  and strain recovery ratio  $R_r$ , which are defined according to [8] as follows:

$$R_f = \frac{\varepsilon_{rem}}{\varepsilon_{pr}}, \quad R_r = \frac{\varepsilon_{pr} - \varepsilon_{rec,m}}{\varepsilon_{pr}}, \quad (1)$$

where  $\varepsilon_{pr}$  is the programming strain, i.e. strain produced by deformation during step 1 of programming as shown in Figure 3,  $\varepsilon_{rem}$  is the remaining strain after cooling to the lowest temperature of an experiment and after subsequent unloading (steps 2 and 3 in Figure 3), and  $\varepsilon_{rec,m}$  is the residual strain measured after thermally induced shape-memory recovery

(shrinkage) at the maximum temperature of an experiment. In case of ideal shape-memory behavior the relations  $\varepsilon_{rem} = \varepsilon_{pr}$  and  $\varepsilon_{rec,m} = 0$  are valid.

If strain recovery is recorded at constant heating rate, the relation between temperature and measuring time is linear. In this connection, the kinetics of shape-memory recovery can be described by means of the recovery rate, i.e. the first derivative of recovery strain with respect to time  $d\varepsilon_{rec}/dt$ . Hence, the absolute peak value of recovery rate  $|d\varepsilon_{rec}/dt|_{max}$  is employed to characterize the maximum shape-memory recovery kinetics. The switching temperature  $T_{sw}$ , as a further important characteristic of SME, is mostly estimated as the temperature, which corresponds to the peak of recovery rate, in contrast to such other definitions of  $T_{sw}$ , as for example a temperature defined by the equation  $\varepsilon_{rec}(T_{sw}) \cdot 100\% = 0.5 \cdot R_r$  [28–29].

Furthermore, polymer networks possessing several crystalline phases with different crystallization/melting temperatures enable observing not only singular but also multiple shape-memory behavior. Multiple switchable shape-memory polymeric materials, which evince triple-shape behavior, have been developed heretofore as presented by Bellin *et al.* [30]. The main disadvantage of such shape-memory polymers is a need for the application of special *multi*-step programming (MSP) process in order to produce the appearance of more or less considerable shape-memory recovery steps during heating at two or more different temperatures [30]. Later it was demonstrated by Behl *et al.* [31] that complex multiphase AB copolymer networks created on the basis of poly( $\varepsilon$ -caprolactone) (PCL) and poly(cyclohexyl methacrylate) with suitable compositions show a pronounced triple-shape behavior with good shape-memory characteristics after simple *one*-step programming (OSP) process. Figure 4 is presented to illustrate the differences between MSP and OSP [32].

Disadvantages of MSP as compared to OSP process are technical complexity, diffuse indistinct steps and peaks of shape-memory recovery strain and rate, respectively, as well as relatively low values of strain fixity  $R_f$  and strain recovery  $R_r$  ratios. This undesirable effect during MSP has to be expected as a consequence of the drastic increase of irreversible deformation part caused by plastic deformation of already crystallized phase in the second and third programming steps. Polymeric materials, which reveal multiple SME, are considered to be highly innovative smart materials with numerous significant applications [30–31]. Because of their great importance, shape-memory polymeric materials with relatively low switching temperatures  $T_{sw}$ , which are nearly equal to melting temperatures of their crystalline phases, are a matter of particular interest.

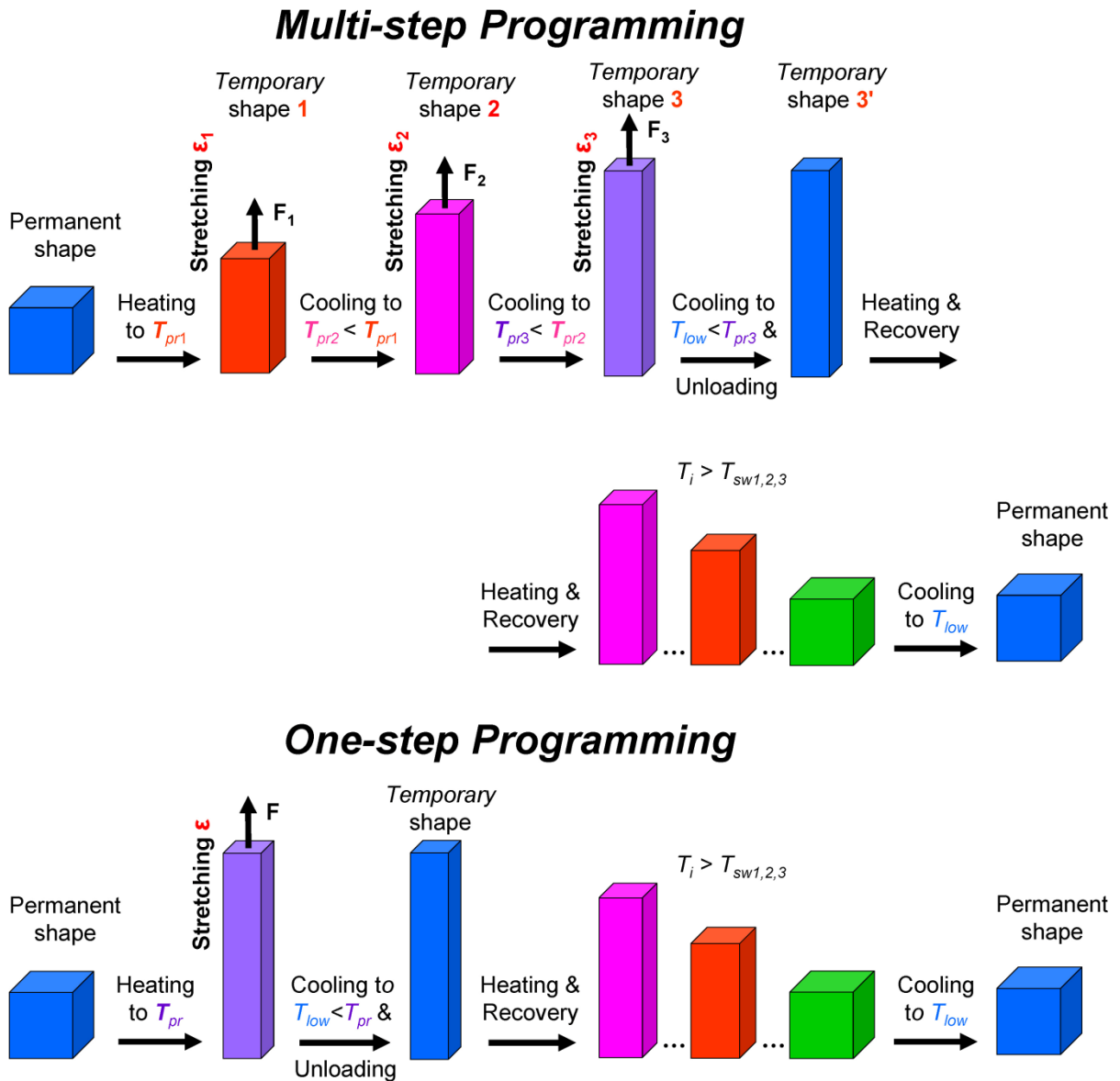


**Figure 4:** Multiple one-way shape-memory behavior of polymeric materials, which are programmed during either MSP (top) or OSP (bottom) process.  $T_{pr}$  is referred to the programming temperature,  $T_{sw}$  is switching temperature of the shape-memory recovery [32].

As an alternative to an expensive synthesis of complex interpenetrating networks and copolymers, multiple SME can be also produced in covalent networks on the basis of polymer blends, if suitable phase morphology could be generated [33–35]. The distinct occurrence of the triple-shape effect in polymer composites on the basis of electrospun PCL fibers embedded in an epoxy-based copolymer thermoset system was reported by Luo and Mather [33]. The temperature dependence of shape-memory recovery strain obtained for this system

both after two-step programming as well as after OSP exhibit two well observable steps/decrements in temperature ranges of glass transition of epoxy-matrix and of PCL melting.

For blends of linear and short-chain branched PEs cross-linked by peroxide an appreciable multiple shape-memory behavior with relatively low characteristics could be achieved only by MSP process [34]. It is assumed that this is caused by the high affinity of blend components in molten state and, correspondingly, by insufficiently segregated crystalline phases of different thermal stability, also indicated by results of differential scanning calorimetry investigations [34]. Also, heterogeneous blends of PEs and thermodynamically incompatible trans-polyoctenamer (TOR) with suitable compositions cross-linked via high energy electrons irradiation show pronounced triple-shape behavior with high performance and even weakly pronounced quadruple-shape behavior after simple OSP process [35].

Similarly, the pronounced triple-shape behavior in bending mode was described independently by Cuevas *et al.* [36] in blend of TOR and linear PE (20 wt% TOR/20 wt% PE) cross-linked by 1–3 wt% dicumyl peroxide. However, the triple-shape behavior in this case was achieved by two-step programming process as well as overall programming deformation  $\varepsilon_{pr}$  was limited to only 19.5%.

Note that initially the binary uncross-linked melt-miscible [9,14] and melt-immiscible polymer blends [28] were used in order to obtain shape-memory polymeric materials with relatively stable physical network. In these blends the crystalline domains with higher thermal stability play a role of physical crosslinks, whereas the domains of amorphous or less stable crystalline phase serve as switching segments. The blends of poly(vinyl acetate) (PVAc) with poly(lactic acid) (PLA) and PVAc or poly(methyl methacrylate) with poly(vinylidene fluoride) are indicative of melt-miscible polymer blends [9,14]. Blends of maleated PE with nylon/polyamide 6 as disperse phase can be cited as an example of melt-immiscible polymer blends [28].

It should be also noted that SME depicted by Xie [37] as multiple SME cannot be considered as a true multiple shape-memory behavior because of the use of special temperature program, which consists of temperature soak (isothermal) segments in addition to temperature ramps during shape-memory recovery measurements. Number and location of these isothermal segments and steps in shape-memory recovery curves show an explicit correlation, which points to the kinetic nature of mentioned steps. The similar drawbacks are contained in some recently published papers [38–39]. One-way ‘triple’-shape behavior of crystallizable covalent networks on the basis of PE/polypropylene blends with co-



continuous phase morphology and on the basis of PCL grafted by 0.5–2.0 wt% of polydopamin (PDA) was evaluated as ‘pronounced’ and ‘good’, respectively, using temperature dependencies of shape-memory recovery of these networks after their two-step programming [38–39]. However, this interpretation cannot be recognized as shape-memory behavior because used temperature-time program contained the isothermal segment between two temperature ramps just within temperature range where the first step of shape-memory recovery strain arises.

Because of the applications of shape-memory polymeric materials in medicine and pharmacology as intended, for instance, by Lendlein and coworkers [10–11,40] and Mather and coworkers [3,9], the biodegradable polyester-based shape-memory polymers have been a matter of particular interest [41]. Furthermore, as mentioned by Karger-Kocsis and coworkers [41–42], the potential applications for shape-memory polymers exist in nearly every area of daily life: from self-repairing car bodies to kitchen utensils, from switches to sensors, from intelligent packing to tools.

### **2.3 Two-way shape-memory effect in polymeric materials**

More than 60 years ago Flory [43–44] and Mandelkern with coworkers [45–46] have predicted and observed the *anomalous* elongation of a polymer network accompanying its crystallization from the oriented “molten” state. Such an anisotropic state of “molten” polymer network, e.g. of cross-linked PE, characterized by a marked orientation of the molecular chains, can be caused by the application of sufficiently high uniaxial extension [45–46]. The surprising macroscopic elongation of a pre-deformed polymer network taking place during its crystallization under load (at a constant force) is denoted as “*anomalous*” because crystallization leads to the considerable toughening of any cross-linked and uncross-linked polymeric materials.

Recently, Mather and coworkers have reported on the dual *two-way* SME in TOR cross-linked by dicumyl peroxide and in a chemical/physical double-network on the basis of PCL and polyhedral oligosilesquioxane, respectively [47–48]. Later Pandini *et al.* [49–50] and Kolesov *et al.* [51] have investigated the two-way SME in single cross-linked linear [49–51] as well as three-arm and four-arm star PCL [49–50]. Principally, the dual two-way SME is revealed as the considerable increment and decrement of strain in the course of non-isothermal crystallization and subsequent melting under constant load, correspondingly [47–48].

Generally, the thermally induced two-way invertible SME in tensile mode can be initiated only in crystallizable covalent polymer networks, which are loaded by suitable constant force. The two-way SME can be observed for preloaded polymer networks in repeating thermal cycles “cooling-heating”. Figure 5 illustrates a conventional two-way shape-memory experiment. Primary heating to the programming temperature  $T_{pr}$  above melting point  $T_m$  and loading of the fully amorphous covalent network result in an initial elastic stretching. At cooling of pre-deformed sample below crystallization temperature  $T_c$  the oriented crystallization of the covalent network leads to an anomalous elongation (creep) of the specimen. The subsequent melting of crystalline phase triggers the shrinkage of a specimen, which results in mechanical work carried out against an external force. In contrast to the one-way *irreversible* SME, the two-way *invertible* SME can be reproduced repeatedly as long as a sample is loaded and temperature change is enough to cause consecutive crystallization and melting of the sample.

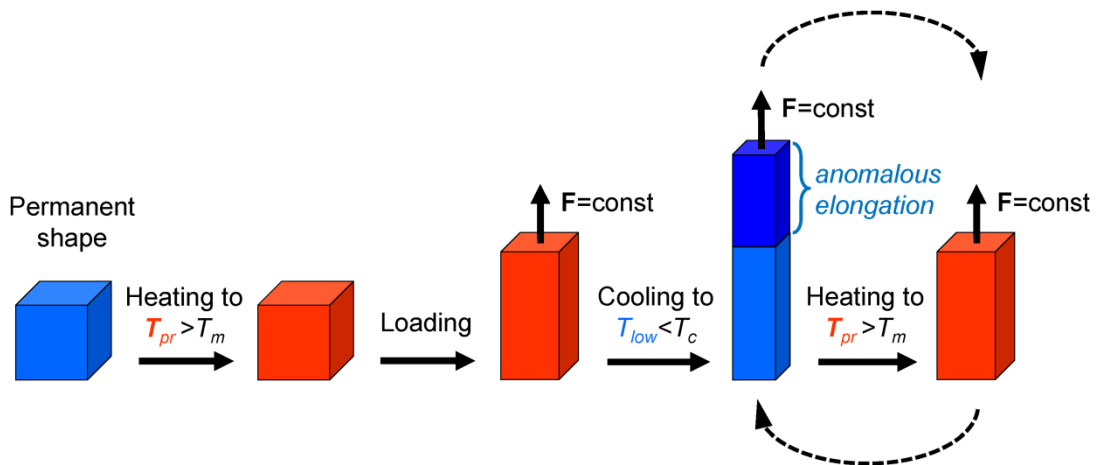


**Figure 5:** The thermally induced two-way invertible shape-memory behavior of cross-linked crystallizable polymers loaded by a constant force  $F$ . Dashed arrows indicate the invertibility of shape changing under constant load by only temperature variation.

Thus, the general manifestation of the two-way SME is on the one hand the anomalous elongation of a sample, which is initiated by the non-isothermal crystallization during cooling under load (at a constant force), and on the other hand the expected contraction of a sample

during heating under the same load triggered by melting of the oriented crystalline phase and by release of the entropy-elastic forces.

The performance of both one- and two-way SME in cross-linked crystallizable polymers strongly depends on the properties of the covalent polymer network and the crystalline structure, which has to be generated in the specimen during isometric programming or shape-memory non-isothermal creep. In the first instance, these are  $T_c$  and  $T_m$  values, crystallinity as a function of temperature, which are dependent on crystal size and perfection, as well as crosslink density and related mechanical properties of the network, such as storage modulus, strain at break, and unrecoverable residual strain  $\varepsilon_{rec,m}$  [52–53]. Particularly, melting and crystallization temperatures  $T_c$  and  $T_m$  serve as shape-memory switching temperatures, whereas crosslink density and crystallinity of the network are responsible for the magnitude of elastic forces produced by loading and for the ability to store the elastic forces, respectively [3,12–14,30–33].

The thermally induced two-way SME with marked triple-shape behavior under suitable load was demonstrated for polymer networks synthesized on the basis of crystallizable segments of poly( $\omega$ -pentadecalactone) (PPD) and PCL by Zotzmann et al. [54]. Both crystallization and melting of specified segment types occur at two different temperatures and are responsible for two increments and two decrements of strain at corresponding temperatures.

The two-way SME in PCL-PDA graft polymer network was reported by Bai et al. [39]. However, these networks demonstrated only negligible values of increment and decrement of SM creep and recovery strain, respectively, which amount merely few percents (3–4%) in spite of relatively large load of 1.3–2.0 MPa [39]. Therefore the practical application of these polymer networks as actuators or sensors should be hardly realizable.

Another strategy to produce the two-way triple-shape behavior in polymeric materials was realized by Kolesov *et al.* [51]. The main focus of the work clearly lies on research of HDPE/PCL and EOC/TOR blends cross-linked by 2,5-bis(t-butylperoxy)-2,5-dimethylhexane and TOR/HDPE blends cross-linked via high energy electrons irradiation. The existence of two crystalline phases with different thermal stability and possessing different melting and crystallization temperatures in heterogeneous polymer networks results in the two-way triple-shape behavior of such networks. Moreover, the performed investigations pointed to crucial effect of phase morphology of cross-linked polymer blends on multiplicity of their shape-memory behavior in addition to the influence of blend content, crystallinity and crosslink density of blend phases as well as of processing conditions.

Some current papers [55–57] containing results of the two-way SME in polymer composites consider other types of the thermally induced invertible shape actuation based on quite different physical principles as described above. So, the thermally induced reversible bending of active asymmetric layered polymer composites-laminates reported by Basit *et al.* [55] and Imai [56] occurs similarly to the well-known bimetallic strip effect in unconstrained as well as constrained state and under load [55–56].

#### **2.4. The reversible shape-memory effect in polymeric materials**

Lately, Westbrook *et al.* [57] described the thermally induced reversible bending of free-standing polymer composite composed of cross-linked pre-deformed TOR strips embedded into the poly(ethylene glycol)dimethacrylate matrix, which was cured by ultraviolet irradiation afterwards. Also, Wu *et al.* [58] reported on the reversible deformation in tensile mode of free-standing interpenetrating networks consisting of crystallizable poly( $\epsilon$ -caprolactone)diol and amorphous poly(tetramethylene ether) glycol segments. The reversible shape changing in both cases [57–58] is apparently caused by the internal stresses stored in the semicrystalline phase of the polymer system during its preparation.

Similarly, Lendlein and coworkers [59–60] detected the so-called *reversible bidirectional* SME under stress-free conditions in cross-linked poly[ethylene-co-(vinyl acetate)] and copolymers on the basis of PPD and PCL. Though the general performance of the aforementioned reversible shape actuation [57–60] of free-standing polymeric materials is the same, the reversible SME discovered by Lendlein and coworkers requires initial programming and has another molecular origin. As shown in Figure 6, to observe the reversible SME a sample of cross-linked semicrystalline polymer is heated to the programming temperature required for melting of all crystalline phases or crystal populations including that has a maximum melting temperature ( $T_{pr} > T_m^{max}$ ). Then totally amorphous covalent network is deformed from an initial *permanent* to a *temporary* shape by applying a constant deformation, cooled down in constant deformed state below the crystallization temperature ( $T_{low} < T_c$ ), and released from an external load keeping its temporary shape until temperature is constantly low. Further heating to the specifically chosen temperature below maximum melting point ( $T_{sep} < T_m^{max}$ ) results in partial melting of crystalline phase or crystal population of lower thermal stability and, correspondingly, in a partial recovery of the programming deformation. In the meantime, some part of the programming deformation is still “memorized” and the sample is deformed due to the presence of remained part of oriented crystalline phase/-s.

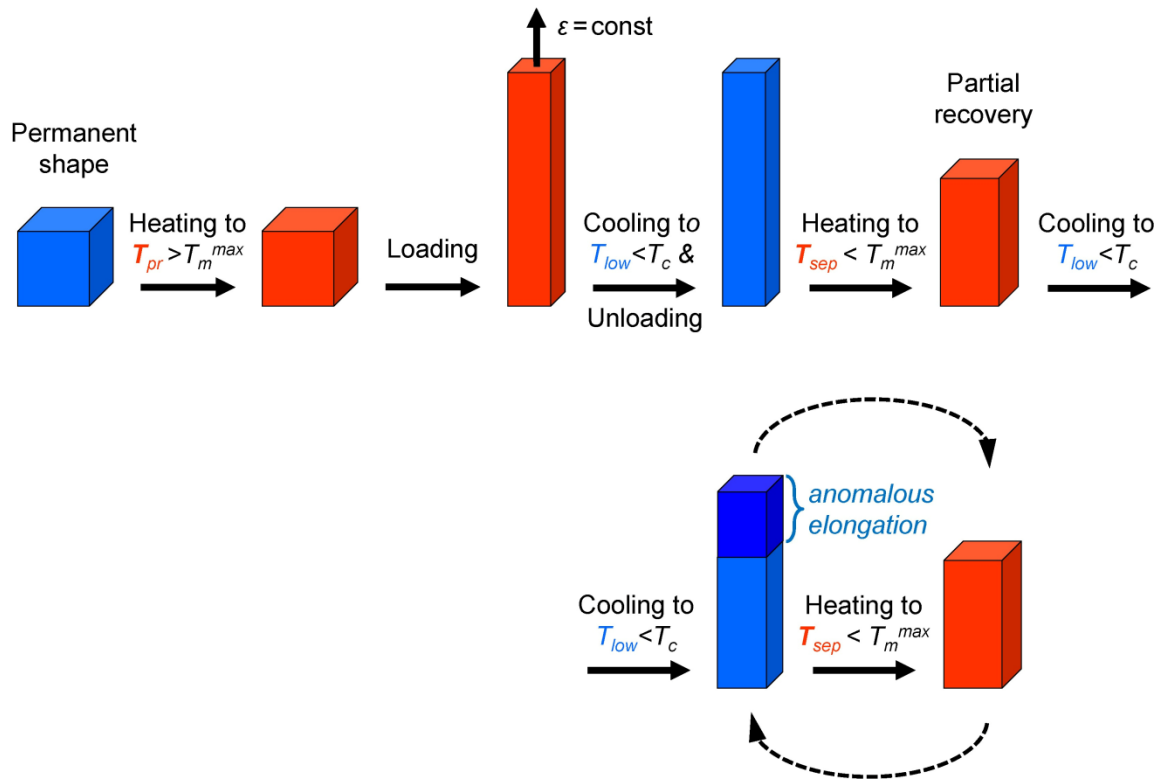


**Figure 6:** The thermally induced reversible bidirectional shape-memory behavior of free-standing cross-linked crystallizable polymers programmed by a constant deformation. Dashed arrows indicate the reversibility of shape changing under stress-free conditions by only temperature variation.

So, temperature  $T_{sep}$  lies between lower and upper bounds of the melting temperature range and separates crystal populations in lower and higher thermally stable ones. The actual reversible SME appears afterwards as an elongation of pre-deformed sample during non-isothermal crystallization at cooling to the  $T_{low}$  below  $T_c$  and the subsequent contraction during heating to the  $T_{sep}$  under stress-free conditions [59–60]. The reversible shape changing at this stage can be produced repeatedly by only temperature variation. Note that no force is applied to a polymer sample now, and this is main advantage of the reversible SME in comparison to the two-way SME requiring constant load. Apparently, the origin of the reversible SME is the same as that of the two-way SME, namely, the elongation in the course of non-isothermal crystallization is caused by the directed growth of crystals as well as sample contraction is initiated by melting of the oriented crystalline phase [51].

The distinct manifestation of the reversible SME was also shown in binary and ternary polymer blends on the basis of HDPE and EOCs with different degree of branching [61]. Received results allowed development of the strategy for further improving the performance of the reversible shape-memory behavior in polymer blends. Namely, the enhanced manifestation of the reversible SME can be observed when a high-temperature crystalline phase is enough elastic and does not prevent the oriented growth of crystals with lower crystallization temperature. In the meantime, a blend component with higher crystallization/melting temperature has to possess enough high crystallinity and to be well coupled with other phase/-s in order to store a deformation, which is sufficient to cause just oriented crystallization of low-temperature blend component/-s that is the basis for the reversible SME.

Summarizing, the novel reversible shape-memory behavior of cross-linked crystallizable polymers, which was discovered by Lendlein and coworkers [59–60], enables adjusting both switching temperature and actuation strain value directly during programming process and is more promising in comparison with the results of Westbrook *et al.* and Wu *et al.* [57–58], since the later implies tailoring the shape-memory properties only during complicated material synthesis. Furthermore, cross-linked polymer blends are regarded as a new class of shape-memory actuators with a lot of advantages, such as wide range of working temperatures, simple processing, and mainly, extensive possibilities for tailoring the thermal and mechanical properties of such shape-memory actuators to industrial requirements by altering blend composition, crosslink density, phase morphology, etc.

Though some specific investigation has been already performed, there is still a lack in experimental and, especially, theoretical study of both two-way and reversible shape-memory phenomena. However, only deep and comprehensive knowledge on the physical background of the reversible shape changing in polymeric materials can ensure a successive development of their producing and applications. The corresponding study is of great academic and industrial interest.

## **2.5. Modeling the shape-memory effect in polymeric materials**

The rapid development and discovery of novel manifestations of shape-memory behavior of polymeric materials require precise and adequate physically grounded modeling the shape-memory phenomena. However, only a small number of scientific publications deals with theoretical description of SME, [62–83] especially in cross-linked semicrystalline polymers [64–65,74,76–77,80]. The most attention was given to modeling the one-way SME [62–

79,81–83] and majority of authors considered predominantly amorphous shape-memory polymers with the glass transition as a switching mechanism and entangled macromolecules as a network [62–63,66–73,75,78–79,81–83].

The constitutive modeling reported by Tobushi *et al.* [62] was the first attempt to describe the thermally induced recovery in amorphous polymers. So, Tobushi *et al.* [62] derived a one-dimensional constitutive model, where the stress-strain relationship is described by modified standard linear approach as follows:

$$\dot{\varepsilon} = \frac{\dot{\sigma}}{E} + \frac{\sigma}{\mu} - \frac{\varepsilon - \varepsilon_S}{\lambda} + \alpha \dot{T}, \quad (2)$$

where  $\varepsilon$ ,  $\sigma$ ,  $T$  are strain, stress, and temperature, respectively;  $E$ ,  $\mu$ ,  $\lambda$ ,  $\alpha$  denote modulus of elasticity, viscosity, retardation time, and coefficient of thermal expansion;  $\varepsilon_S$  represents the irrecoverable residual strain after one-way shape-memory recovery. Also, the authors tried to expand their theory for a case of large deformations by introducing a non-linear term expressed by a power function of stress. The temperature dependence of the coefficients  $E$ ,  $\mu$ ,  $\lambda$  was introduced on the basis of empirically obtained expression:

$$x = x_g \left[ a \left( \frac{T}{T_g} - 1 \right) \right], \quad (3)$$

where  $x_g$  is the value of  $x$ , that is  $E$ ,  $\mu$ ,  $\lambda$ , at  $T = T_g$ ; the exponent  $a$  is assumed to be constant for each coefficient. The presented model was used to fit the experimental data of the temperature dependent shape-memory recovery strain of polyurethanes. The results of fitting showed a tolerable accordance between the theory and the experimental findings.

Perhaps, the most cited paper on modeling the one-way SME in amorphous polymers is the work of Liu *et al* [63]. Here the authors derived a three-dimensional small-strain internal state variable constitutive model, which is claimed to quantify the storage and release of the entropic deformation during thermo-mechanical processes. The fraction of the material, which freezes a temporary entropy state, is a function of temperature and can be determined by fitting the free strain recovery response. The most essential assumption made by authors is coexisting of so-called “frozen” and “active” phases in a sample of the amorphous shape-memory polymer, as shown in Figure 7. According to Liu *et al.* [63], the frozen phase, which is composed of frozen C–C bonds, implies that the conformational rotation of polymer chains corresponding to the high temperature entropic deformation is completely locked, whereas the internal energetic change, such as the stretching or small rotation of the polymer bonds, can occur. Besides, any further conformational motion of the material is impossible in the

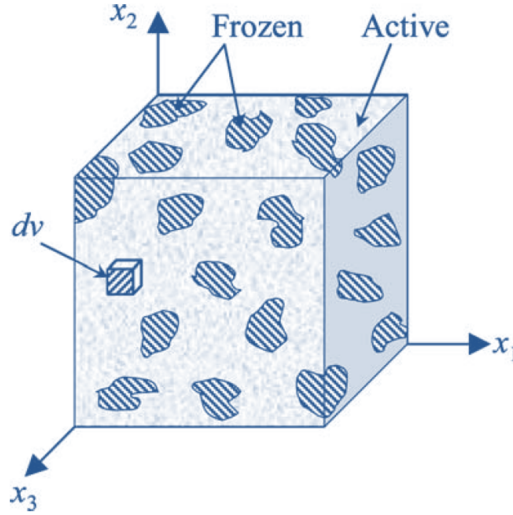


**Figure 7:** Schematic model of the micromechanics foundation of the three-dimensional shape memory polymer reported by Liu *et al* [63]. Existence of two extreme phases in the polymer is assumed. The model represents a polymer in the glass transition state with a predominant active phase.

frozen phase, which is the major phase of a polymer in the glassy state below  $T_g$ . On the contrary, the active phase of the model in Figure 7 consists of active C–C bonds, so the free conformational motion can potentially occur. A change in the ratio of these two phases triggered by the glass transition during a thermo-mechanical cycle provides the shape changing and shape recovery, so the one-way shape-memory behavior can be captured. However, such an assumption is inconsistent with the common interpretation of the glass transition, since it results in the immobilization of macromolecular chain segments and in triggering their *cooperative* mobility below and above the glass transition temperature  $T_g$ , respectively, and relates to *all* polymer chains, which are a part of amorphous phase [84]. In this connection, existing of immobilized “frozen” phase dispersed in continuous “active” rubbery phase seems to be speculative and physically unrealizable. Moreover, temperature dependence for the frozen volume fraction  $\phi_f$  is expressed as follows:

$$\phi_f = \frac{1}{1+c_f(T_h-T)^n}. \quad (4)$$

According to Liu *et al.* [63], the phenomenological Equation (4) is “based on the experimental result” and was not explained and grounded anywhere in the text. In addition, the authors



assumed linear elastic behavior of polymers that strictly limits their theory to very small deformations comparable with simple thermal expansion/contraction. The fitting of the recoverable strain as a function of temperature, which was measured for epoxy resin and limited to less than 11%, revealed poor accordance between the model and the experimental results. Hence, the approach of Liu *et al.* cannot be concerned as efficient and fruitful in modeling the shape-memory behavior of amorphous polymers. In the meantime, it can be the case for crystallizable polymers, where crystalline and amorphous phases coexist below melting point  $T_m$  and therefore such polymers are called *semicrystalline*.

Chen and Lagoudas [66–67] tried to extend the approach of Liu and coworkers [63] to a case of large deformations. But the fitting they provided was performed for the same experimental findings for epoxy resin limited to small deformation as reported by Liu *et al.* [63]. Thus, the potential of the presented theoretical treatment was not properly verified.

Yu *et al.* [72] tried to model the “multiple shape-memory behavior” reported by Xie [37], which however cannot be recognized as a true shape-memory phenomenon that was discussed above. Therefore the model of Yu *et al.* has no relation to the real thermally induced one-way SME.

Additionally, some authors compare results calculated on the basis of proposed approaches only with the experimental data received by Liu *et al.* for amorphous resin at the programming deformations below 11% [69,71,78], while other works include only theoretical investigation without any comparison with experimental results [64–65,70]. Summarizing, the common drawback of the discussed theoretical considerations of the one-way SME in polymers is their engineering-mechanical focus and almost neglect of the molecular mechanism underlying the shape-memory phenomenon. The authors were more concentrated on the mechanics of the recoverable shape changing and did not take into account the physics, i.e. physical reasons, which cause and mainly determine the shape-memory behavior of polymers. The used assumptions and equations frequently do not imply and do not comprise sufficient physical background. For instance, Ge and coworkers employed *Kohlrausch–Williams–Watts* (KWW) stretch exponential function to describe the relaxation modulus “regardless of the physical origin” as they wrote [73]; the same physically ungrounded utilization of KWW function contains another paper of the authors [75]. Note that KWW function is frequently used to describe the relaxation behavior of the storage modulus undergoing just the *glass-rubber transition* [84].

Heuchel *et al.* [79] were concentrated on the description of shape-memory behavior of polymers at the programming process, that is, during loading at temperature above melting/glass transition, but not during the thermally induced recovery.

Only several scientific groups have tried their theoretical modeling the one-way shape-memory behavior for cross-linked crystallizable polymers in case of deformation about 100% and more [76–78]. Nevertheless, there are some circumstances, which complicate description of the shape-memory recovery on the basis of these approaches. For example, Khonakdar and coworkers [76–77] employed without sufficient physical substantiation a primitive mechanical model containing a Kelvin element and a dashpot with the nonlinear temperature dependent viscosity:

$$\eta = \eta_0 U(T) + (Ae^{-E_p/RT} - \eta_0)U(T - T_r), \quad (5)$$

where  $U(T)$  and  $U(T - T_r)$  are step functions,  $T$  is temperature,  $T_r$  is recovery onset temperature (i.e. switching temperature),  $A$  is a pre-exponential factor,  $E_p$  is the activation energy,  $\eta_0$  is the viscosity below  $T_r$ . However, the physical sense of Equation (5), the introduction and explicit form of the step functions were not defined and described. Moreover, according to Equation (5), viscosity of a dashpot increases with increasing temperature above  $T_r$  ( $T > T_r$ ). Such dependence is completely absurd, especially with respect to polymeric materials. Additionally, the basic principles, which Khonakdar and coworkers used for the model, are highly questionable. So, at the primary exposition of their mechanical model [76] the authors obtained the equation describing the time dependent stress relaxation during programming by constant deformation:

$$\sigma = \sigma_0 \left(1 + \frac{\eta_1}{\eta_2}\right) / \left(1 + \frac{\eta_1}{\eta_2} + \frac{t}{\tau}\right), \quad (6)$$

here  $\eta_1$  and  $\eta_2$  are viscosities of two dashpots,  $t$  is time, and  $\tau$  is relaxation time. The simple analysis of Equation (6) shows that stress has strictly *hyperbolic* dependence on time, but the authors claimed *step-like* behavior of stress with time, which was illustrated in the corresponding plot as well. This obvious contradiction casts doubts on the paper's integrity and value. It is a great pity that several excellent reviews on SME in polymeric materials [3,14] referenced to the aforementioned works of Khonakdar and coworkers but did not point to such inadmissible mistakes.

Wang *et al.* [78] presented the modeling approach similar to that of Liu *et al.* [63] but focused on the description of SME in crystallizable polymers. The authors used the modified Avrami equation as expression for the temperature dependent frozen volume fraction  $\phi_f$  and

fitted the experimental results of one-way SME obtained for amorphous epoxy resin, where the glass transition serves as a switching mechanism. Since the Avrami equation describes the crystallization kinetics [85], its use in case of shape changing caused by the glass transition seems to be inconsistent and contradictory.

Ge *et al.* [74] tried to model the shape-memory behavior of elastomeric composites developed by Westbrook and coworkers [57] as discussed above. Though the elastomeric composites demonstrate the thermally induced reversible shape actuation, in fact Ge *et al.* [74] did not deal with the two-way SME at all. The most significant manifestation of the two-way shape-memory behavior is the anomalous elongation of a material under load during non-isothermal crystallization at cooling. Though the authors were concentrated on modeling the both free and constrained recovery, they neither concern the aforementioned anomalous elongation of a material experimentally nor theoretically. If a polymeric material under load does not reveal the anomalous elongation during non-isothermal crystallization, the subsequent constrained recovery is not the manifestation of the two-way SME. The molecular mechanism of the anomalous elongation was not considered anywhere in the paper. In addition, the authors tried their modeling for the specific shape-memory composites consisting of an elastomeric matrix reinforced by a semicrystalline polymer fiber network [57].

Up to now only one publication is known dealing with modeling the two-way SME in cross-linked semicrystalline polymers [80]. However, the authors used constitutive mechanical or engineering modeling and the anomalous elongation under constant load during non-isothermal crystallization was not physically explained as well as proposed assumptions remained unclear. Namely, Westbrook *et al.* [80] assumed that the stretch induced crystalline phase will contribute to the deformation of a sample. It should be emphasized that the anomalous elongation induced by crystallization is a central object of the two-way shape-memory phenomenon and cannot be simply postulated. A proper modeling the two-way SME in cross-linked crystallizable polymers must give clear explanation and description of such unique behavior, in which crystallization plays a key role. Obviously, mechanical modeling cannot satisfy this condition and therefore is inappropriate.

Finally, molecular dynamic simulations of shape-memory amorphous PLA and poly[(*rac*-lactide)-*co*-glycolide] developed by Ghobadi and coworkers [81–83] stand separately. The authors attempted to compute the programming process and moisture-induced shape recovery of single PLA macromolecule. Unfortunately, such modeling did not imply any experimental verification of the proposed assumptions. Besides, the test conditions was chosen evidently

physically unrealizable, as both cooling and heating runs occurred with a rate higher than  $10^{11}$   $\text{K}\cdot\text{s}^{-1}$ . Additionally, fitting of the relaxation processes during unloading and recovery was based on a simple mathematical model expressed by the equation consisting of one or two exponential decay functions [82–83]. The physical grounds of using such equation were not properly described and explained.

### 3. Objectives

The present work aims to develop a physically grounded theoretical approach that would be able to disclose and explain the drastic elongation of cross-linked semicrystalline polymers under load at cooling below crystallization temperature  $T_c$ , as the most essential manifestation of the two-way SME, in terms of molecular orientation, crystal morphology, and its change in the course of crystallization. The analytical model should enable the evaluation of such essential characteristics of the crystal structure as crystallinity, crystal thickness, and orientation of crystal chains. The influence of entangled slipped macromolecules on the shape-memory performance should be also taken into account to ensure precise modeling the thermo-mechanical response of a real material. Furthermore, the model has to provide successful fitting of the temperature dependent strain of loaded PEs samples measured during cooling-heating cycles.

Specific goal of the work is the detailed experimental analysis of the effect of loading and crosslink density on the two-way shape-memory performance of linear HDPE and short-chain branched EOCs characterized by different crystallinity, crystallization and melting temperatures, and stiffness. Dynamic-mechanical thermal analysis is used to study simultaneously the temperature dependence of storage modulus accompanied by the macroscopic elongation and contraction of PEs samples during non-isothermal crystallization and melting, respectively. Thorough analysis of the temperature dependent strain measured during the two-way shape-memory behavior of PEs requires introduction of proper empirical parameters of such a peculiar thermo-mechanical behavior.

Melting and crystallization behavior of two sets of PEs specimens – undeformed and stretched after occurrence of the anomalous elongation under constant load – is investigated by differential scanning calorimetry. Enthalpy-based crystallinity of underformed and stretched samples is calculated on the basis of measured heat capacity curves.

Transmission electron microscopy is employed to compare the morphology of crystals generated at cooling below  $T_c$  in undeformed PEs samples and stretched samples crystallized under constant load. The transmission electron microscopy images allow estimating the relative orientation of crystals formed in the stretched PEs specimens as well.

Wide- and small-angle X-ray scattering of stretched PEs under study enables precise analysis of the orientation of both crystal unit cell and crystal texture relative to the direction of applied load as well as estimation of crystal thickness. Moreover, wide-angle X-ray

scattering allows studying an evolution of the orientation of the unit cell of crystals generated during the two-way shape-memory behavior of HDPE under different loads.

Fitting of the temperature dependent strain measured during the two-way shape-memory behavior of PEs is based on the derived theory of the two-way SME. Values of fitting parameters are used to evaluate the relevant characteristics of crystal structure like crystallinity, crystal thickness, the orientation of crystal chains as well as its evolution with increasing load. Comparison between the theoretical values of these characteristics and their experimental estimations got by differential scanning calorimetry, transmission electron microscopy, and X-ray scattering enables substantial and reliable verification of the theory of the two-way SME.

## 4. Molecular and structural based theoretical description of the two-way shape-memory effect

### 4.1. The mechanical model

The mechanical behavior of cross-linked polymers in rubber state (above melting point  $T_m$  or glass transition temperature  $T_g$ ) and in case of a small extension ( $1 < \text{draw ratio} \leq 1.2$ ) is well described by the statistical mechanical theory of rubber elasticity [86], but an increase of the extension leads to deviation from this theory. Up to now different molecular mechanisms like loose chain ends, temporary and permanent chain entanglements, and intramolecular crosslink points were considered to explain the divergence between the classical statistical theory and experiments [86–87]. Although all these mechanisms contribute to the total deformation, the present work considers chain entanglements as the most probable mechanism, which influences the shape-memory behavior. On this account, the three-element mechanical model with non-Newtonian dashpot presented in Figure 8 was chosen for the

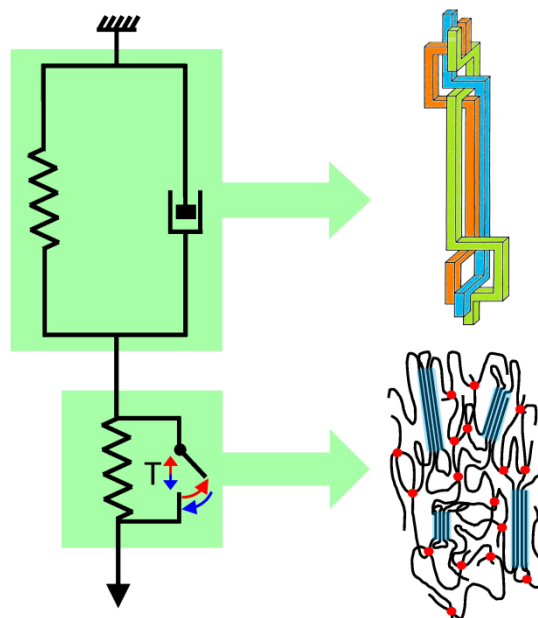


**Figure 8:** *The three-element mechanical model proposed for the description of thermo-mechanical behavior of cross-linked crystallizable polymers. Kelvin-Voigt element represents entangled slipped macromolecules, while lower spring is responsible for the crystallizable covalent polymer network.*

description of thermo-mechanical behavior of cross-linked crystallizable polymers under constant load at cooling/heating runs.

The possibility of using such a model in case of creep/recovery process has been already pointed out in the works of Eyring and coworkers [88] and Ziabicki [89]. However, in this work just non-isothermal creep and recovery of cross-linked polymers under constant load is considered and following specifications of elements in the model are proposed [90–91].

Firstly, a spring and a dashpot connected in parallel called Kelvin-Voigt element [88] represent slipped entangled molecular chains containing loops and ends (Figure 8). In order to explain the mechanism of shape fixing and recovery in this case, the Eyring's rate theory of viscoelastic deformation is employed [88]. The viscous flow of entangled macromolecules is thermally activated process characterized by the activation energy  $U$ . The activation energy  $U$  is defined as a minimal energy, which a system should possess to enable the viscous flow. To be more exact, the activation energy equals the height of symmetrical potential energy barrier, which separates equilibrium positions of flow units. Even in the absence of stress individual flow units surmount energy barrier exchanging their old equilibrium positions for the new ones, but such exchanging is statistically balanced, so that no flow is observed. After applying a force the energy barrier is not symmetrical anymore, and the number of individual flow units moving in the direction of applied force is larger than in the opposite direction. The flow of individual units is accompanied by stretching of the entangled molecules and results in macroscopic deformation. However, stretched state of macromolecules is not thermodynamically favorable, because stretching decreases entropy, whereby the free energy increases. Cooling to the lower temperature causes both the reduction of kinetic energy of macromolecules in mobile amorphous phase and mainly the formation of immobilized ordered domains due to crystallization. At low temperature the number of molecules in different equilibrium states is not statistically balanced but they do not possess enough energy to surmount the energy barrier. Thus the temporary sample shape is fixed. Further heating results in melting of immobilized crystalline phase and in increase of the kinetic energy of flow units. They move to become statistically distributed over the equilibrium positions and to minimize the free energy that results in strain recovery [91].

Secondly, the covalent network is represented by the second lower spring assuming that crystallization occurs in the network and affects on the network tensile modulus [90–91]. Generally speaking, the crystallization takes place both in the network and beyond, but just crystallization of the covalent network makes a principal contribution to the mechanical



properties of cross-linked polymers. A trigger switch is connected in parallel with the second spring in order to illustrate shape fixing and shape recovery of the covalent network caused by its crystallization and melting, respectively.

Thus, the model accounts two basic molecular mechanisms involved in the shape-memory behavior of cross-linked crystallizable polymers – the viscous flow of entangled macromolecules and crystallization/melting of the covalent polymer network [90–91]. It should be emphasized that such composition and definitions of elements in the model presented here are able to describe temperature dependent creep and recovery of cross-linked semicrystalline polymeric materials in case of a large deformation what is mentioned above.

Figure 9 illustrates the behavior of the model in response to main stages of the two-way SME in cross-linked crystallizable polymers [92–93]. Note that though the model in Figure 9b–d exemplifies typical two-way shape-memory phenomenon, both the anomalous elongation during non-isothermal crystallization at cooling and subsequent strain recovery during melting at heating are *not postulated*. As it will be shown below, the two-way shape-memory behavior is derived as a possible event of the thermo-mechanical response of cross-

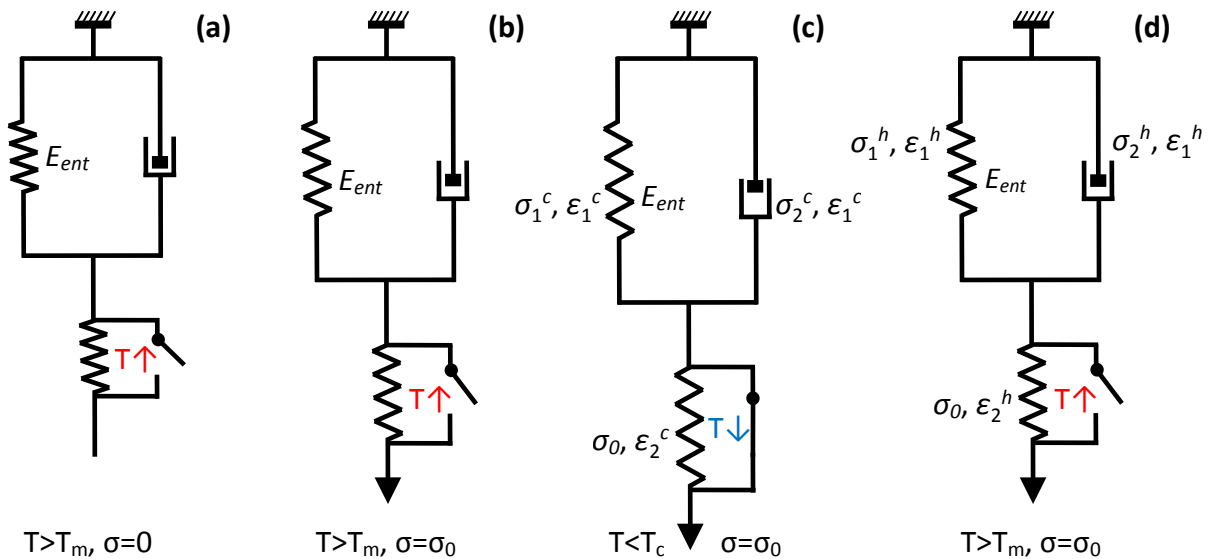


**Figure 9:** The three-element model describing stages of the two-way SME in cross-linked semicrystalline polymers: heating above melting point  $T_m$  (a), applying a constant load and initial stretching (b), cooling below crystallization temperature  $T_c$  accompanied with the anomalous elongation (c), heating above melting temperature  $T_m$  accompanied with strain recovery (d) [92–93].

linked polymeric materials under constant load and is not the only case.

Hereinafter, for all elements of the model in Figure 9 as  $\varepsilon_i$  is designated Cauchy or engineering strain related to the initial total length of a sample as follows:

$$\varepsilon_i = \frac{\Delta l_i}{l_0}, \quad (7)$$

where  $\Delta l_i$  is the absolute deformation of the  $i$ -th element,  $l_0$  is the initial total length of a sample in a state shown in Figure 9a. Upper indices for Cauchy strains and stresses in Figure 9c–d are used to denote cooling and heating runs, respectively.

According to the model presented in Figure 9c–d and to the designations given by Equations (7) stresses and strains are arranged as follows:

$$\sigma_0 = \sigma_1^c + \sigma_2^c, \quad \varepsilon^c = \varepsilon_1^c + \varepsilon_2^c; \quad (8a)$$

$$\sigma_0 = \sigma_1^h + \sigma_2^h, \quad \varepsilon^h = \varepsilon_1^h + \varepsilon_2^h, \quad (8b)$$

where,  $\sigma_0$  is true stress applied to a sample,  $\varepsilon$  is the total strain of the model as a function of temperature.

## 4.2. Model behavior at cooling below $T_c$ under constant load

### 4.2.1. Effect of entangled slipped macromolecules

The viscoelastic flow of entangled polymer chains in the course of cooling below crystallization temperature  $T_c$  is represented by Kelvin-Voigt element in Figure 9c. Since a single molecule may be regarded as possessing an elasticity governed by Hooke's law (stress proportional to strain) [87] the stress-strain relationship of a spring in Kelvin-Voigt element is described as  $\sigma_1^c = E_{ent} \cdot \varepsilon_1^c$ . Also, supposing that expression for the tensile modulus derived in the theory of rubbery elasticity of phantom network is valid for a single entangled molecule, modulus  $E_{ent}$  can be written:

$$E_{ent} = \frac{3}{2} \nu_e RT, \quad (9)$$

where  $\nu_e$  is the density of entangled molecules involved in the process of viscous flow,  $R$  is the gas constant,  $T$  is the absolute temperature. Thus, stress acting on a spring is as follows:

$$\sigma_1^c = \frac{3}{2} \nu_e RT \varepsilon_1^c. \quad (10)$$

According to Eyring's rate theory of viscoelastic deformation [88] a dashpot in Kelvin-

Voigt element is described as:

$$\dot{\varepsilon}_1^c = 2 \frac{V_h}{V_m} \cdot \frac{k_B T}{h} \cdot \exp\left(-\frac{U}{k_B T}\right) \cdot \sinh\left(\frac{V_h \sigma_2^c}{2k_B T}\right), \quad (11)$$

here  $V_h$  is the volume of the hole swept out by the motion or activation volume [88],  $V_m$  is the volume of flowing molecule,  $U$  is the activation free energy of the process,  $k_B$  is the Boltzmann constant,  $h$  is the Planck constant, point over strain denotes time derivative. Stress acting on a dashpot can be rewritten using Equations (8a) and (10):

$$\sigma_2^c = \sigma_0 - \sigma_1^c = \sigma_0 - \frac{3}{2} \nu_e R T \varepsilon_1^c. \quad (12)$$

Substituting Equation (12) in (11) implies:

$$\dot{\varepsilon}_1^c = 2 \frac{V_h}{V_m} \cdot \frac{k_B T}{h} \cdot \exp\left(-\frac{U}{k_B T}\right) \cdot \sinh\left(\frac{V_h \sigma_0}{2k_B T} - \frac{3}{4} \frac{V_h}{k_B} \nu_e R \varepsilon_1^c\right). \quad (13)$$

Now, one can estimate the values of hyperbolic sine in (13). In the range  $\sigma_0 < 2 \cdot 10^6$  Pa,  $V_h < 10 \text{ nm}^3$ ,  $T < 500$  K,  $\nu_e < 100 \text{ mol} \cdot \text{m}^{-3}$ ,  $\varepsilon_1^c < 3$  hyperbolic sine can be approximated as follows:

$$\sinh\left(\frac{V_h \sigma_0}{2k_B T} - \frac{3}{4} \frac{V_h}{k_B} \nu_e R \varepsilon_1^c\right) \approx \frac{V_h \sigma_0}{2k_B T} - \frac{3}{4} \frac{V_h}{k_B} \nu_e R \varepsilon_1^c, \quad (14)$$

here approximation percent error  $\delta_{ap} < 0.1$  % that ensures sufficiently precise consideration.

Using approximation (14) Equation (13) can be rewritten:

$$\dot{\varepsilon}_1^c = \frac{V_h^2}{V_m h} \cdot \exp\left(-\frac{U}{k_B T}\right) \cdot \left(\sigma_0 - \frac{3}{2} \nu_e R T \varepsilon_1^c\right). \quad (15)$$

In case of constant cooling rate  $\frac{dT}{dt} = -\gamma$  strain rate is defined as:

$$\dot{\varepsilon}_1^c = \frac{d\varepsilon_1^c}{dt} = -\gamma \frac{d\varepsilon_1^c}{dT}. \quad (16)$$

Also, true stress  $\sigma_0$  can be expressed through nominal stress  $\sigma_{0N}$  defined as a force divided by the *original* cross-sectional area:

$$\sigma_0 = \sigma_{0N} (1 + \varepsilon_1^c). \quad (17)$$

Since applied force is constant during shape-memory experiment,  $\sigma_{0N}$  remains constant as well. Substituting expressions (16) and (17) in Equation (15) it enables:

$$\frac{d\varepsilon_1^c}{dT} = \frac{V_h^2}{V_m \gamma h} \cdot \exp\left(-\frac{U}{k_B T}\right) \cdot \left(\frac{3}{2} \nu_e R T \varepsilon_1^c - \sigma_{0N} (1 + \varepsilon_1^c)\right). \quad (18)$$

Based on the experimental results the activation volume  $V_h$  can be assumed weakly dependent on the temperature and in the first approximation its temperature dependence can be ignored [94]. Thereby Equation (18) is a non-homogeneous first-order linear differential equation. For the sake of simplicity, the following is denoted:

$$A \triangleq \frac{3 V_h^2 R}{2 V_m \gamma h} \nu_e, \quad B \triangleq \frac{V_h^2}{V_m \gamma h} \sigma_{0N}. \quad (19)$$

Thus, the differential equation (18) can be rewritten as follows:

$$\frac{d\varepsilon_1^c}{dT} + (B - A \cdot T) \cdot \exp\left(-\frac{U}{k_B T}\right) \varepsilon_1^c + B \cdot \exp\left(-\frac{U}{k_B T}\right) = 0. \quad (20)$$

The solution of the linear differential equation (20) is sought in the product form [95]:

$$\varepsilon_1^c = u(T) \cdot v(T). \quad (21)$$

This implies to write Equation (20) as:

$$\left[ v'_T + (B - A \cdot T) \cdot \exp\left(-\frac{U}{k_B T}\right) v \right] \cdot u + u'_T \cdot v + B \cdot \exp\left(-\frac{U}{k_B T}\right) = 0, \quad (22)$$

where  $v'_T$  and  $u'_T$  denote the first derivatives with respect to temperature. Generally,  $v = v(T)$  is any function that satisfies the “truncated” equation [95]:

$$v'_T + (B - A \cdot T) \cdot \exp\left(-\frac{U}{k_B T}\right) v = 0. \quad (23)$$

The solution of Equation (23) is the first part of the solution of the principal differential equation (22), which allows obtaining the temperature dependent strain  $\varepsilon_1^c = \varepsilon_1^c(T)$  as an ultimate goal of this section.

So, Equation (23) is a first-order differential equation with separable variables, it can be rewritten as:

$$\int \frac{dv}{v} = -B \cdot \int \exp\left(-\frac{U}{k_B T}\right) dT + A \cdot \int T \exp\left(-\frac{U}{k_B T}\right) dT. \quad (24)$$

Integral in the left part of Equation (24) is a tabulated and equals  $\int \frac{dv}{v} = \ln v$ . On the contrary, both integrals in the right part of (24) are nontrivial and their solution requires particular mathematical treatment.

**I.** Using integration by substitution and by parts the first integral in the right part of (24) is solved:

$$\begin{aligned} \int \exp\left(-\frac{U}{k_B T}\right) dT &= \left\{-\frac{U}{k_B T} = y; T = -\frac{U}{k_B y}; dT = \frac{U}{k_B y^2} dy\right\} = \frac{U}{k_B} \int \frac{1}{y^2} e^y dy = \\ &= -\frac{U}{k_B} \frac{1}{y} e^y + \frac{U}{k_B} \int \frac{1}{y} e^y dy = \{[96]\} = T \cdot \exp\left(-\frac{U}{k_B T}\right) + \frac{U}{k_B} \cdot \text{Ei}\left(-\frac{U}{k_B T}\right). \end{aligned} \quad (25)$$

Here  $\text{Ei}\left(-\frac{U}{k_B T}\right)$  is the integral exponential function defined as [97]:

$$\text{Ei}(x) = \int_{-\infty}^x \frac{e^t}{t} dt. \quad (26)$$

For  $x < 0$  the integral exponential function can be written as  $\text{Ei}(x) = \text{li}(e^x)$ , where  $\text{li}(z)$  is the integral logarithm [97]:

$$\text{li}(z) = \int_0^z \frac{dt}{\ln(t)}. \quad (27)$$

When  $z \ll 1$ , the integral logarithm can be approximated as  $\text{li}(z) \approx \frac{z}{\ln(1/z)}$  [97]. In the wide range of temperatures  $250 < T$  [K]  $< 600$  and activation energies  $50 < U$  [kJ · mol<sup>-1</sup>]  $< 200$ , which are more than acceptable for observing the shape-memory behavior in polymers, the Boltzmann factor possesses values  $10^{-42} < \exp\left(-\frac{U}{k_B T}\right) < 10^{-5}$ . Hence, the integral exponential function  $\text{Ei}\left(-\frac{U}{k_B T}\right)$  can be expressed as follows:

$$\text{Ei}\left(-\frac{U}{k_B T}\right) = \text{li}\left[\exp\left(-\frac{U}{k_B T}\right)\right] \approx \frac{\exp\left(-\frac{U}{k_B T}\right)}{\ln\left[\exp\left(-\frac{U}{k_B T}\right)\right]} = \frac{k_B T}{U} \cdot \exp\left(-\frac{U}{k_B T}\right). \quad (28)$$

Substitution of expression (28) in (25) implies the final solution of the first integral in the right part of (24):

$$\int \exp\left(-\frac{U}{k_B T}\right) dT = T \cdot \exp\left(-\frac{U}{k_B T}\right) + T \cdot \exp\left(-\frac{U}{k_B T}\right) = 2T \cdot \exp\left(-\frac{U}{k_B T}\right) \quad (29)$$

**II.** The second integral in the right part of (24) is solved:

$$\begin{aligned} \int T \exp\left(-\frac{U}{k_B T}\right) dT &= \left\{-\frac{U}{k_B T} = y; T = -\frac{U}{k_B y}; dT = \frac{U}{k_B y^2} dy\right\} = -\frac{U^2}{k_B^2} \int \frac{1}{y^3} e^y dy = \\ &= -\frac{U^2}{k_B^2} \left[-\frac{1}{2y^2} e^y + \frac{1}{2} \int \frac{1}{y^2} e^y dy\right] = -\frac{U^2}{k_B^2} \left[-\frac{1}{2y^2} e^y - \frac{1}{2y} e^y + \frac{1}{2} \int \frac{1}{y} e^y dy\right] = \\ &= -\frac{U^2}{k_B^2} \left[-\frac{k_B^2 T^2}{2U^2} \exp\left(-\frac{U}{k_B T}\right) + \frac{k_B T}{2U} \exp\left(-\frac{U}{k_B T}\right) + \frac{1}{2} \text{Ei}\left(-\frac{U}{k_B T}\right)\right]. \end{aligned} \quad (30)$$

Using Equations (26)–(28) and the same approximation for the integral logarithm as mentioned above the final solution of the second integral in the right part of (24) is as follows:

$$\begin{aligned} \int T \exp\left(-\frac{U}{k_B T}\right) dT &= -\frac{U^2}{k_B^2} \left[ -\frac{k_B^2 T^2}{2U^2} \exp\left(-\frac{U}{k_B T}\right) + \frac{k_B T}{U} \exp\left(-\frac{U}{k_B T}\right) \right] = \\ &= \frac{UT}{2k_B} \left[ \frac{k_B T}{U} - 2 \right] \cdot \exp\left(-\frac{U}{k_B T}\right). \end{aligned} \quad (31)$$

So, the solution of the differential equation (24) is given by:

$$\ln v = -2BT \cdot \exp\left(-\frac{U}{k_B T}\right) + A \frac{UT}{2k_B} \left[ \frac{k_B T}{U} - 2 \right] \cdot \exp\left(-\frac{U}{k_B T}\right). \quad (32)$$

Besides, the relevant ranges of temperatures and activation energies considered above impose constraints on the exponent of the Boltzmann factor as well:  $\frac{k_B T}{U} \ll 1$ . Thereupon the solution (32) can be rewritten as:

$$v = \exp\left[-\left(2B + A \frac{U}{k_B}\right) \cdot T \cdot \exp\left(-\frac{U}{k_B T}\right)\right]. \quad (33)$$

Thus, expression (33) is the first part of the solution of the principal differential equation (22). The second part is sought in the function  $u = u(T)$  by solving a linear differential equation with separable variables:

$$u'_T \cdot v + B \cdot \exp\left(-\frac{U}{k_B T}\right) = 0. \quad (34)$$

Using solution (33) Equation (34) is transformed:

$$u'_T = -B \cdot \exp\left(-\frac{U}{k_B T}\right) \cdot \exp\left[\left(2B \frac{U}{k_B} + A \frac{U^2}{k_B^2}\right) \cdot \frac{k_B T}{U} \cdot \exp\left(-\frac{U}{k_B T}\right)\right]. \quad (35)$$

Again for the sake of simplicity it is denoted:

$$C \triangleq 2B \frac{U}{k_B} + A \frac{U^2}{k_B^2}. \quad (36)$$

So, after separation of variables and substitution the definition (36) Equation (35) is expressed:

$$u = -B \cdot \int \exp\left(-\frac{U}{k_B T}\right) \cdot \exp\left[C \frac{k_B T}{U} \cdot \exp\left(-\frac{U}{k_B T}\right)\right] dT. \quad (37)$$

To find the function  $u = u(T)$  the integral in (37) is analytically calculated as:

$$\begin{aligned}
& \int \exp\left(-\frac{U}{k_B T}\right) \cdot \exp\left[C \frac{k_B T}{U} \cdot \exp\left(-\frac{U}{k_B T}\right)\right] dT = \left\{-\frac{U}{k_B T} = y; T = -\frac{U}{k_B y}; dT = \frac{U}{k_B y^2} dy\right\} = \\
& = \frac{U}{k_B} \int \frac{1}{y^2} e^y e^{\frac{-C}{y} e^y} dy = \left\{\frac{1}{y^2} = -\left(\frac{1}{y} - \frac{1}{y^2}\right) + \frac{1}{y}\right\} = -\frac{U}{k_B} \int \left(\frac{1}{y} - \frac{1}{y^2}\right) e^y e^{\frac{-C}{y} e^y} dy + \\
& + \frac{U}{k_B} \int \frac{1}{y} e^y e^{\frac{-C}{y} e^y} dy = -\frac{U}{k_B} \int e^{\frac{-C}{y} e^y} d\left(\frac{1}{y} e^y\right) + \frac{U}{k_B} \int \frac{1}{y} e^y e^{\frac{-C}{y} e^y} dy = \frac{U}{k_B} \frac{1}{C} e^{\frac{-C}{y} e^y} + \\
& + \frac{U}{k_B} \int \frac{1}{y} e^y e^{\frac{-C}{y} e^y} dy = \left\{d\Omega = \frac{1}{y} e^y dy; \Omega = \int \frac{1}{y} e^y dy = \text{Ei}(y) = \text{li}(e^y) \approx -\frac{1}{y} e^y\right\} = \\
& = \frac{U}{k_B} \frac{1}{C} e^{\frac{-C}{y} e^y} + \frac{U}{k_B} \int e^{C\Omega} d\Omega = \frac{U}{k_B} \frac{1}{C} e^{\frac{-C}{y} e^y} + \frac{U}{k_B} \frac{1}{C} e^{\frac{-C}{y} e^y} + c_0 = 2 \frac{U}{k_B} \frac{1}{C} e^{\frac{-C}{y} e^y} + c_0 = \\
& = 2 \frac{U}{k_B} \frac{1}{C} \exp\left[C \frac{k_B T}{U} \cdot \exp\left(-\frac{U}{k_B T}\right)\right] + c_0, \tag{38}
\end{aligned}$$

where  $c_0$  is the constant of integration. Thus, using designation (36) the function  $u = u(T)$  is expressed:

$$u = -\frac{2BUk_B}{2BUk_B + AU^2} \exp\left[\left(2B + A \frac{U}{k_B}\right) \cdot T \cdot \exp\left(-\frac{U}{k_B T}\right)\right] + c_0. \tag{39}$$

Now, going back to the temperature dependent strain implies substituting the received solutions (33) and (39) in (21):

$$\varepsilon_1^c = -\frac{2BUk_B}{2BUk_B + AU^2} + c_0 \cdot \exp\left[-\left(2B + A \frac{U}{k_B}\right) \cdot T \cdot \exp\left(-\frac{U}{k_B T}\right)\right]. \tag{40}$$

Imposing constraint  $\varepsilon_1^c(T = 0) = \varepsilon_{01} = \text{const}$ , where  $\varepsilon_{01}$  is the part of total strain stored by entangled slipped molecules, on the differential equation (18) expression (40) is transformed into:

$$\varepsilon_1^c = -\frac{2BUk_B}{2BUk_B + AU^2} + \left(\varepsilon_{01} + \frac{2BUk_B}{2BUk_B + AU^2}\right) \cdot \exp\left[-\left(2B + A \frac{U}{k_B}\right) \cdot T \cdot \exp\left(-\frac{U}{k_B T}\right)\right]. \tag{41}$$

Finally, reverting through designations (19) to the original molecular parameters the temperature dependent strain caused by viscoelastic flow of entangled macromolecules is expressed as follows:

$$\varepsilon_1^c = -\frac{\sigma_{0N}}{\sigma_{0N} + 3/4 v_e U} + \left(\varepsilon_{01} + \frac{\sigma_{0N}}{\sigma_{0N} + 3/4 v_e U}\right) \cdot \exp\left[-\frac{2V_h^2}{V_m} \cdot \frac{\sigma_{0N} + 3/4 v_e U}{\gamma h} T \cdot \exp\left(-\frac{U}{RT}\right)\right]. \tag{42}$$

#### 4.2.2. Effect of crystallizing covalent network

The effect of crystallization of covalent network under constant load on the shape-memory performance of semicrystalline polymers is considered in this section. A theory of the stress-induced crystallization of cross-linked polymers developed by Gaylord *et al.* [98–99] is used to describe the behavior of covalent polymer network at cooling during the two-way SME. Though a thermodynamic approach presented below is based on the Gaylord's theory, it allows calculating the free energy change of a network deformed under constant load (not constant deformation) and cooled down below crystallization temperature  $T_c$  at a constant cooling rate, i.e. in non-isometric and non-isothermal conditions, respectively. These criteria distinguish the present approach from the aforementioned theory of the stress-induced crystallization.

Following Gaylord [99], a polymer chain linking two neighboring crosslink points is represented by a non-Gaussian distribution function:

$$W(\mathbf{r}_N) = \left(\frac{3}{2\pi N b_0^2}\right)^{3/2} \cdot \exp\left(-\frac{3r_N^2}{2N b_0^2}\right) \cdot \left(1 - \frac{3}{4N} + \frac{3r_N^2}{2N^2 b_0^2} - \frac{9r_N^4}{20N^3 b_0^4}\right), \quad (43)$$

where  $\mathbf{r}_N$  is the end-to-end vector of a polymer chain containing  $N$  links, each of length  $b_0$ . Note that expression (43) is obtained as an approximation of the statistical theory of networks of non-Gaussian flexible chains developed by Wang and Guth [100] in case of  $N \gg 1$  and  $r_N \ll Nb$ .

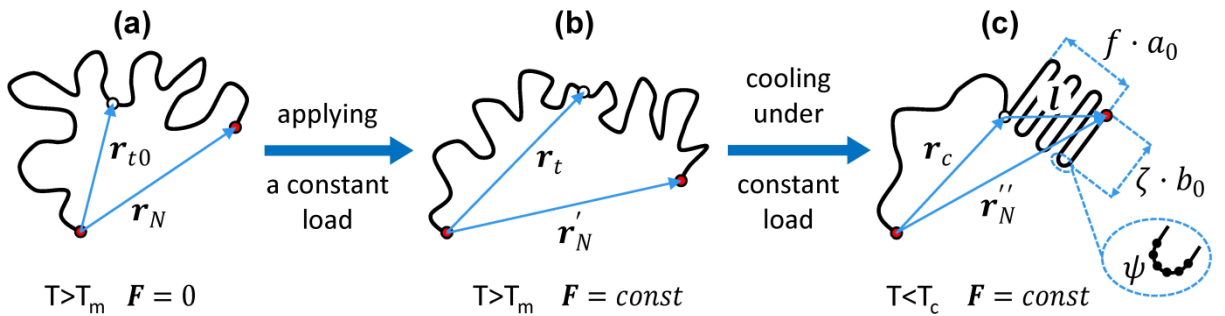


**Figure 10:** The schematic crystallization of a network chain under load: amorphous, undeformed chain (a); chain deformed by applying a constant load (b); chain crystallized under constant load (c). Red points represent crosslink points; white imagined point divides the chain into amorphous and crystallized subchains [92–93].



Figure 10 illustrates schematically the change of a network chain loaded by constant force in amorphous state (Figure 10b) and crystallized after cooling below crystallization temperature  $T_c$  (Figure 10c). According to Gaylord *et al.* [98–99], the total free energy of the network chain deformed by applying a constant load and cooled below  $T_c$  consists of three terms:

- 1) the free energy change arising from transferring links from the amorphous region to the crystal,  $-N\chi_c\Delta H_\mu \left(1 - \frac{T}{T_m^0}\right)$ , where  $\Delta H_\mu$  is the enthalpy of fusion per link,  $\chi_c$  is the crystallinity,  $T_m^0$  is the equilibrium melting temperature;
- 2) the free energy of the interface between amorphous and crystalline regions  $U_{em}$ , and  $fU_e$  – the surface free energy of a crystal with  $f$  folds, each with  $\psi$  links (see designations in Figure 10c) and surface energy  $U_e$ ;
- 3) the entropy change  $\Delta S$  in the remaining  $N\theta = (N - N\chi_c - \psi f)$  links of the chain, which spanned the distance  $r_{t0}$  in the undeformed, amorphous network and which span the distance  $r_c$  after crystallization occurs. If the  $N\theta$  links of amorphous subchain follows non-Gaussian statistics given by Equation (43) then the corresponding free energy change can be written as  $\Delta F_{entr} = -T\Delta S = -RT[\ln W(\mathbf{r}_c) - \ln W(\mathbf{r}_{t0})]$ .

Thus, using Equation (43) for the entropy change the free energy of crystallization is expressed as:

$$\begin{aligned} \Delta F_f(T, \chi_c) = & -N\chi_c\Delta H_\mu \left(1 - \frac{T}{T_m^0}\right) + U_{em} + fU_e + \frac{3RT}{2Nb^2} \left[\frac{1}{\theta} - \frac{1}{N\theta^2}\right] [\langle r_c^2 \rangle - \langle r_{t0}^2 \rangle] + \\ & + \frac{9RT}{20N^3\theta^3b^4} [\langle r_c^4 \rangle - \langle r_{t0}^4 \rangle]. \end{aligned} \quad (44)$$

The angle brackets indicate that mean value of the vectors of the amorphous subchain is considered. The task is to calculate all mean values in (44) and express the solutions in terms of molecular and structural parameters depicted in Figure 10c.

The mean value  $\langle r_{t0}^2 \rangle$  in (44) can be evaluated from the internal link calculation as follows:

$$\begin{aligned} \langle r_{t0}^2 \rangle = & \int_{-\infty}^{\infty} r_{t0}^2 \cdot W(\mathbf{r}_{t0}) d\mathbf{r}_{t0} = \\ = & \left(\frac{3}{2\pi N\theta b_0^2}\right)^{3/2} \cdot \left[\left(1 - \frac{3}{4N\theta}\right) \cdot \int_{-\infty}^{\infty} r_{t0}^2 \cdot \exp\left(-\frac{3r_{t0}^2}{2N\theta b_0^2}\right) d\mathbf{r}_{t0} + \right. \end{aligned}$$

$$+ \frac{3}{2N\theta b_0^2} \int_{-\infty}^{\infty} r_{t0}^4 \cdot \exp\left(-\frac{3r_{t0}^2}{2N\theta b_0^2}\right) d\mathbf{r}_{t0} - \frac{9}{20N^3\theta^3 b_0^4} \int_{-\infty}^{\infty} r_{t0}^6 \cdot \exp\left(-\frac{3r_{t0}^2}{2N\theta b_0^2}\right) d\mathbf{r}_{t0} \Big]. \quad (45)$$

Initially, let us consider the first integral in (45). The square of the end-to-end vector  $r_{t0}^2$  can be expressed in terms of its projections in the Cartesian coordinate system:

$$r_{t0}^2 = x_{t0}^2 + y_{t0}^2 + z_{t0}^2. \quad (46)$$

The polynomial (46) enables to write the first integral in (45) in the following form:

$$\begin{aligned} \int_{-\infty}^{\infty} r_{t0}^2 \cdot \exp\left(-\frac{3r_{t0}^2}{2N\theta b_0^2}\right) d\mathbf{r}_{t0} &= \iiint_{-\infty}^{\infty} x_{t0}^2 \cdot \exp\left(-\frac{3(x_{t0}^2+y_{t0}^2+z_{t0}^2)}{2N\theta b_0^2}\right) dx_{t0} dy_{t0} dz_{t0} + \\ &+ \iiint_{-\infty}^{\infty} y_{t0}^2 \cdot \exp\left(-\frac{3(x_{t0}^2+y_{t0}^2+z_{t0}^2)}{2N\theta b_0^2}\right) dx_{t0} dy_{t0} dz_{t0} + \\ &+ \iiint_{-\infty}^{\infty} z_{t0}^2 \cdot \exp\left(-\frac{3(x_{t0}^2+y_{t0}^2+z_{t0}^2)}{2N\theta b_0^2}\right) dx_{t0} dy_{t0} dz_{t0}. \end{aligned} \quad (47)$$

All integrals in (47) are of the same type and are calculated as follows [96]:

$$\int_{-\infty}^{\infty} q^{2n} e^{-Pq^2} dq = \frac{(2n-1)!!}{(2P)^n} \sqrt{\frac{\pi}{P}} \quad (48)$$

for  $P > 0$  and  $n = 0, 1, 2 \dots$  that is exactly our case. Using solution (48) the integral (47) equals:

$$\int_{-\infty}^{\infty} r_{t0}^2 \cdot \exp\left(-\frac{3r_{t0}^2}{2N\theta b_0^2}\right) d\mathbf{r}_{t0} = \left(\frac{2\pi N\theta b_0^2}{3}\right)^{3/2} N\theta b_0^2. \quad (49)$$

Similarly, higher powers of the end-to-end vector  $r_{t0}^4$  and  $r_{t0}^6$  in (45) can be expressed in terms of their projections. Substitution of the obtained polynomials in (45) implies integrals of the type (48), which equal:

$$\int_{-\infty}^{\infty} r_{t0}^4 \cdot \exp\left(-\frac{3r_{t0}^2}{2N\theta b_0^2}\right) d\mathbf{r}_{t0} = \left(\frac{2\pi N\theta b_0^2}{3}\right)^{3/2} \cdot \frac{5N^2\theta^2 b_0^4}{3}, \quad (50a)$$

$$\int_{-\infty}^{\infty} r_{t0}^6 \cdot \exp\left(-\frac{3r_{t0}^2}{2N\theta b_0^2}\right) d\mathbf{r}_{t0} = \left(\frac{2\pi N\theta b_0^2}{3}\right)^{3/2} \cdot \frac{35N^3\theta^3 b_0^6}{9}. \quad (50b)$$

Thus, substituting solutions (49)–(50) in (45) the mean value  $\langle r_{t0}^2 \rangle$  becomes:

$$\langle r_{t0}^2 \rangle = N\theta b_0^2. \quad (51)$$

The vector  $\mathbf{r}_c$  can be written in terms of the end-to-end vector  $\mathbf{r}_N''$  and the vector  $\mathbf{l}$  characterizing the crystallite (Figure 10c):

$$\mathbf{r}_c = \mathbf{r}_N'' - \mathbf{l}, \quad (52a)$$

$$r_c^2 = r_N''^2 + l^2 - 2\mathbf{r}_N'' \cdot \mathbf{l}. \quad (52b)$$

Assuming affine deformation of the chain from the initially isotropic, amorphous state results in

$$\langle r_N''^2 \rangle = (\lambda_x^2 + \lambda_y^2 + \lambda_z^2) \frac{\langle r_N^2 \rangle}{3}, \quad (53)$$

where  $\lambda_x$  is the extension ratio in the  $x$  direction. Based on the internal link calculation (51) the mean value  $\langle r_N^2 \rangle$  equals  $\langle r_N^2 \rangle = Nb_0^2$ .

Following Gaylord *et al.* [98–99], one can assume that crystal vector  $\mathbf{l}$  lies *along* the direction of applied force, in the same direction as the  $x$  component of the end-to-end vector  $\mathbf{r}_N''$ , irrespective of the morphology of the crystallite. This assumption enables to take into account only the  $x$  component of the  $\mathbf{r}_N'' \cdot \mathbf{l}$  term in Equation (52b) and to write:

$$\langle \mathbf{r}_N'' \cdot \mathbf{l} \rangle = \lambda_x l \langle x_N \rangle, \quad (54)$$

where the mean value  $\langle x_N \rangle$  implies

$$\langle x_N \rangle = \int_{-\infty}^{\infty} x_N \cdot W(\mathbf{r}_N) d\mathbf{r}_N = 2 \int_0^{\infty} |x_N| \cdot W(\mathbf{r}_N) d\mathbf{r}_N. \quad (55)$$

Similarly to the internal link calculation performed above, the expression (55) can be expanded into integrals of the type (48), when the exponent in the power function is even, and into the gamma functions  $\Gamma(n)$  [96], when the exponent is odd and higher than 1:

$$\Gamma(n) = \int_0^{\infty} \frac{x^{n-1}}{e^x} dx = (n-1)!. \quad (56)$$

Thus, after calculating the mean value  $\langle x_N \rangle$  is as follows:

$$\langle x_N \rangle = \frac{Nb_0}{3} \sqrt{\frac{6}{\pi N}} \left(1 + \frac{1}{20N}\right). \quad (57)$$

In case of affine uniaxial deformation the mean value  $\langle r_c^2 \rangle$  is expressed:

$$\langle r_c^2 \rangle = \left(\lambda_2^2 + \frac{2}{\lambda_2}\right) \frac{Nb_0^2}{3} + l^2 - \frac{2}{3} \sqrt{\frac{6}{\pi N}} Nb_0 l \lambda_2 \left(1 + \frac{1}{20N}\right), \quad (58)$$

where subscript in  $\lambda_2$  refers to the mechanical model and corresponding designations presented in Figure 9.

As shown in Figure 10c, the crystal vector  $\mathbf{l}$  can be expressed in terms of the crystallite thickness  $\zeta \cdot b_0$ , and the length of the crystallite along the fold surface  $f \cdot a_0$ , where  $a_0$  is the chain thickness and  $\zeta$  is the number of links traversing the crystallite:

$$\zeta = \frac{N\chi_c}{(f+1)}. \quad (59)$$

So, the vector  $\mathbf{l}$  can be expressed for the general case of an  $f$ -folded crystallite as:

$$l = \sqrt{f^2 a_0^2 + \beta \zeta^2 b_0^2} = \varphi b_0, \quad (60a)$$

$$\varphi = \sqrt{\frac{f^2 a_0^2}{b_0^2} + \beta \zeta^2} \quad \begin{array}{l} \beta = 1, \text{ even folds} \\ \beta = 0, \text{ odd folds} \end{array} \quad (60b)$$

Equations (60) disclose the assumption about parallelism of the applied force and the crystal vector  $\mathbf{l}$ , namely, number of folds  $f$  and parameter  $\beta$  control the orientation of the crystallite relative to applied force. The odd number of folds ( $f = 1, 3, \dots$ ) results in perpendicular orientation of chains in the crystallite to the external force, whereas even number of folds corresponds to the case when the orientation of chains in crystal is parallel to the stretch direction ( $f = 0$ ) or makes an acute angle with it ( $f = 2, 4, \dots$ ). This important condition will be employed in further consideration.

The calculation of  $\langle r_{t0}^4 \rangle$  and  $\langle r_c^4 \rangle$  strictly follows the same manner used for the evaluation of  $\langle r_{t0}^2 \rangle$  and  $\langle r_c^2 \rangle$ , namely  $\langle r_{t0}^4 \rangle$  equals:

$$\begin{aligned} \langle r_{t0}^4 \rangle &= \langle (x_{t0}^2 + y_{t0}^2 + z_{t0}^2)^2 \rangle = \\ &= \int_{-\infty}^{\infty} (x_{t0}^2 + y_{t0}^2 + z_{t0}^2)^2 \cdot W(\mathbf{r}_N) d\mathbf{r}_N = \frac{N^2 \theta^2 b_0^4}{3} \left( 5 - \frac{2}{N\theta} \right). \end{aligned} \quad (61)$$

The mean value  $\langle r_c^4 \rangle$  is expressed by using (52b):

$$\langle r_c^4 \rangle = \langle r_N''^4 \rangle + 2l^2 \langle r_N''^2 \rangle + l^4 + 4\lambda_2^2 l^2 \langle x_N^2 \rangle - 4\lambda_2 l \langle r_N''^2 x_N \rangle - 4\lambda_2 l^3 \langle x_N \rangle. \quad (62)$$

Each mean value in Equation (62) except for  $\langle x_N \rangle$  already ascertained in (57) can be transformed by the procedure shown in (53)–(54) and calculated as:

$$\langle r_N''^4 \rangle = \langle \left( x_N''^2 + y_N''^2 + z_N''^2 \right)^2 \rangle = \langle \left( \lambda_2^2 x_N^2 + \frac{1}{\lambda_2} y_N^2 + \frac{1}{\lambda_2} z_N^2 \right)^2 \rangle =$$

$$\begin{aligned}
 &= \int_{-\infty}^{\infty} \left( \lambda_2^2 x_N^2 + \frac{1}{\lambda_2} y_N^2 + \frac{1}{\lambda_2} z_N^2 \right)^2 \cdot W(\mathbf{r}_N) d\mathbf{r}_N = \\
 &= \left( \lambda_2^4 + \frac{4}{3} \lambda_2 + \frac{8}{3\lambda_2^2} \right) \frac{N^2 b_0^4}{3} \left( 1 - \frac{2}{5N} \right), \tag{63a}
 \end{aligned}$$

$$\begin{aligned}
 \langle r_N''^2 \rangle &= \left( \lambda_2^2 + \frac{2}{\lambda_2} \right) \frac{1}{3} \langle r_N^2 \rangle = \left( \lambda_2^2 + \frac{2}{\lambda_2} \right) \frac{1}{3} \int_{-\infty}^{\infty} r_N^2 \cdot W(\mathbf{r}_N) d\mathbf{r}_N = \\
 &= \left( \lambda_2^2 + \frac{2}{\lambda_2} \right) \frac{N b_0^2}{3}, \tag{63b}
 \end{aligned}$$

$$\langle x_N^2 \rangle = \int_{-\infty}^{\infty} x_N^2 \cdot W(\mathbf{r}_N) d\mathbf{r}_N = \frac{N b_0^2}{3}, \tag{63c}$$

$$\begin{aligned}
 \langle r_N''^2 x_N \rangle &= \langle (x_N''^2 + y_N''^2 + z_N''^2) x_N \rangle = \langle \lambda_2^2 x_N^3 + \frac{1}{\lambda_2} x_N y_N^2 + \frac{1}{\lambda_2} x_N z_N^2 \rangle = \\
 &= \int_{-\infty}^{\infty} \left( \lambda_2^2 x_N^3 + \frac{1}{\lambda_2} x_N y_N^2 + \frac{1}{\lambda_2} x_N z_N^2 \right) \cdot W(\mathbf{r}_N) d\mathbf{r}_N = \\
 &= \left( \lambda_2^2 + \frac{1}{\lambda_2} \right) \frac{2N^2 b_0^3}{9} \sqrt{\frac{6}{\pi N}} \left( 1 - \frac{3}{20N} \right), \tag{63d}
 \end{aligned}$$

The solutions (57) and (63) are now substituted in (62), whereby  $\langle r_c^4 \rangle$  implies:

$$\begin{aligned}
 \langle r_c^4 \rangle &= \frac{N^2 b_0^4}{3} \left[ \left( 1 - \frac{2}{5N} \right) \left( \lambda_2^4 + \frac{4}{3} \lambda_2 + \frac{8}{3\lambda_2^2} \right) + \frac{2l^2}{N b_0^2} \left( \lambda_2^2 + \frac{2}{\lambda_2} \right) + \frac{4l^2}{N b_0^2} \lambda_2^2 + \frac{3l^4}{N^2 b_0^4} - \right. \\
 &\left. - \frac{8l\delta}{3b_0} \left( 1 - \frac{3}{20N} \right) (\lambda_2^3 + 1) - \frac{4l^3\delta}{N b_0^3} \left( 1 + \frac{1}{20N} \right) \lambda_2 \right], \tag{64}
 \end{aligned}$$

where  $\delta = \sqrt{\frac{6}{\pi N}}$ .

Finally, using received solutions (51), (58), (61), (64), approximation  $N \gg 1$ , and designation for  $l$  following from (60a) the free energy of crystallization of an  $f$ -folded, semicrystalline chain can be rewritten as:

$$\begin{aligned}
 \Delta F_f(\chi_c, T, \lambda_2) &= -N \chi_c \Delta H_\mu \left( 1 - \frac{T}{T_m^0} \right) + U_{em} + f U_e + \frac{RT}{2\theta} \left[ 1 - \frac{1}{N\theta} \right] \cdot \left[ \lambda_2^2 - \right. \\
 &\left. - 2\varphi\delta \left( 1 + \frac{1}{20N} \right) \lambda_2 + \frac{2}{\lambda_2} + \frac{3\varphi^2}{N} - 3\theta \right] + \frac{3RT}{20N\theta^3} \left[ \lambda_2^4 + \frac{4}{3} \lambda_2 + \frac{3\varphi^4}{N^2} + \frac{8}{3} \frac{1}{\lambda_2^2} + \frac{6\varphi^2}{N} \lambda_2^2 \right. \\
 &\left. + \frac{4\varphi^2}{N} \frac{1}{\lambda_2} - \frac{8}{3} \varphi\delta (\lambda_2^3 + 1) - \frac{4}{N} \varphi^3 \delta \lambda_2 - \theta^2 \left( 5 - \frac{2}{N\theta} \right) \right]. \tag{65}
 \end{aligned}$$

In order to express the free energy of crystallization as a function of temperature  $T$  and draw ratio  $\lambda_2$ , the Ozawa equation normalized by the switching transition temperature at cooling  $T_{sw}^c$  [78,101], which is assumed to be crystallization temperature in the present consideration, is used as a function for the crystallinity  $\chi_c$  supposing constant cooling rate:

$$\chi_c = A \cdot \exp \left[ -K \left( \frac{T}{T_{sw}^c} \right)^m \right], \quad (66)$$

where  $A$  is the crystallinity at  $T \rightarrow 0$ ,  $K$  and  $m$  are materials constants related to the cooling rate and rate of crystallization, respectively.

Further analysis requires detailed consideration the free energy of crystallization (65). For this purpose HDPE is used as the model object. To calculate the free energy of crystallization  $\Delta F_f(T, \lambda_2)$  as a function of temperature and draw ratio for different values of chain links  $N$  and folds  $f$  in case of cross-linked HDPE the appropriate values for the parameters in Equation (65) are  $U_{em} = 13791.3 \text{ J}\cdot\text{mol}^{-1}$ ,  $U_e = 13238.7 \text{ J}\cdot\text{mol}^{-1}$ ,  $b_0 = 0.154 \text{ nm}$ ,  $a_0 = 0.425 \text{ nm}$ ,  $\psi = 4$ ,  $T_m^0 = 419 \text{ K}$ ,  $\Delta H_\mu = 4140 \text{ J}\cdot\text{mol}^{-1}$  [98–99,102]. The values for the parameters of the Ozawa equation (66) are chosen so that the calculated crystallinity roughly corresponds to the experimental findings for HDPE. Nevertheless, parameters of the Equation (66) will be precisely determined further in the section devoted to modeling the two-way SME in cross-linked PEs. Note that draw ratio  $\lambda_2$  is originally defined as the actual length of the covalent network divided by its initial length. However, to link this designation with the model in Figure 9c it is necessary to transform  $\lambda_2$  into  $\lambda_2^c$ , where  $\lambda_2^c = \varepsilon_2^c + 1$ , as follows:

$$\lambda = \frac{l_2}{l_{02}} = \frac{l_2}{l_0} \cdot \frac{l_0}{l_{02}} = \lambda_2^c \cdot \Lambda, \quad (67)$$

here  $l_2$  is the actual length of covalent network,  $l_{02}$  is the initial length of undeformed covalent network,  $l_0$  is the initial total length of undeformed sample,  $\Lambda$  is the correction factor. For the calculation of the free energy of crystallization the correction factor is assumed to possess the value  $\Lambda = 2$  but it will be evaluated more precisely during fitting appeared in the section devoted to modeling the two-way SME.

Thus, the free energies of crystallization  $\Delta F_f(T, \lambda_2^c)$  as a function of temperature  $T$  and draw ratio  $\lambda_2^c$  calculated for cross-linked HDPE on the basis of Equations (65)–(67) in case of different values of chain links and different numbers of crystal folds are plotted in Figure 11. The values  $\Delta F_f(T, \lambda_2^c)$  corresponding to numbers of folds  $f = 2, 3$  and  $f > 4$  are greater in the presented ranges of temperature and draw ratio, so they are not shown. Note that the

values  $N = 650$  (Figure 11a) and  $N = 850$  (Figure 11b) were selected in order to exemplify cases when the lowest free energy corresponds to crystals with different number of chain folds.

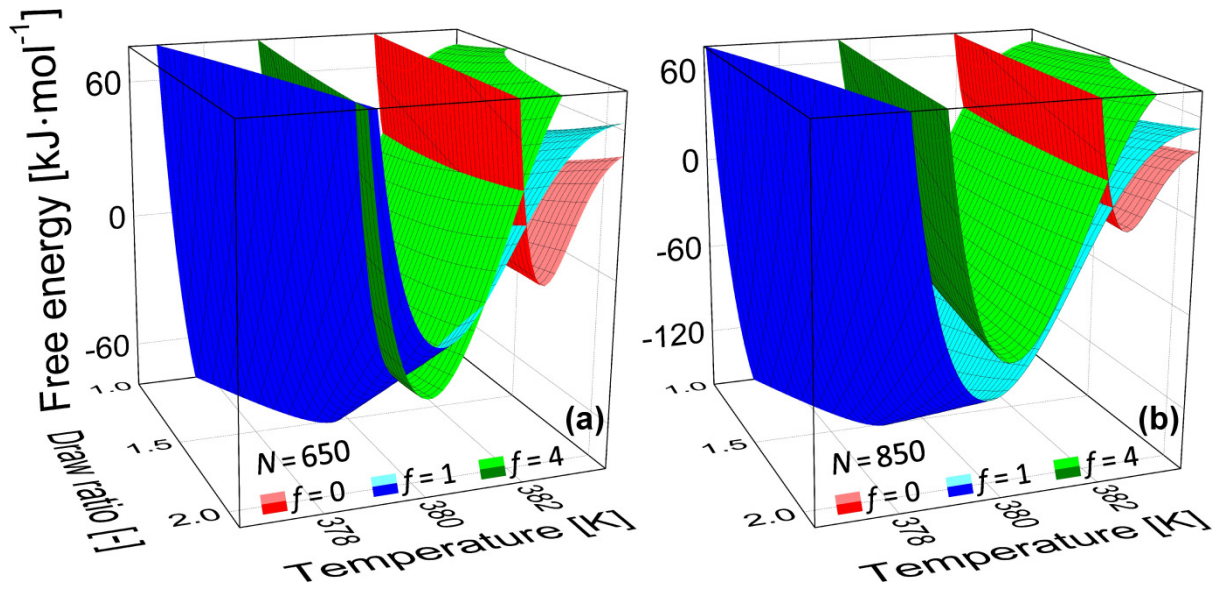


**Figure 11:** The free energy of crystallization  $\Delta F_f(T, \lambda_2^c)$  as a function of temperature  $T$  and draw ratio  $\lambda_2^c$  calculated for HDPE in case of different values of chain links  $N = 650$  (a),  $N = 850$  (b), and different numbers of crystal folds  $f$  [92–93].

The results indicate that a covalent polymer network having different number of chain links  $N$  and subjected to the same deformation may form crystals with quite different orientation, namely, for presented magnitudes  $N$  the extended-chain morphology ( $f = 0$ ) has a lower free energy at the onset of crystallization, whereas further cooling results in forming the folded-chain crystals oriented nearly parallel ( $f = 4$ , Figure 11a) or perpendicular to the stretch direction ( $f = 1$ , Figure 11b). Evidently, these different cases of the orientation of crystals lead to dramatically different mechanical behavior of pre-deformed crystallizing covalent network. It is expected that perpendicular orientation of chain folds in crystals results in sample contraction during crystallization, while the anomalous elongation of a sample under load during the two-way SME can be observed when crystal chains are parallel to the

force direction or make an acute angle with it. Nevertheless, such a suggestion will be verified by fitting the experimental findings of the two-way SME in PEs in the following *Section 6.6*.

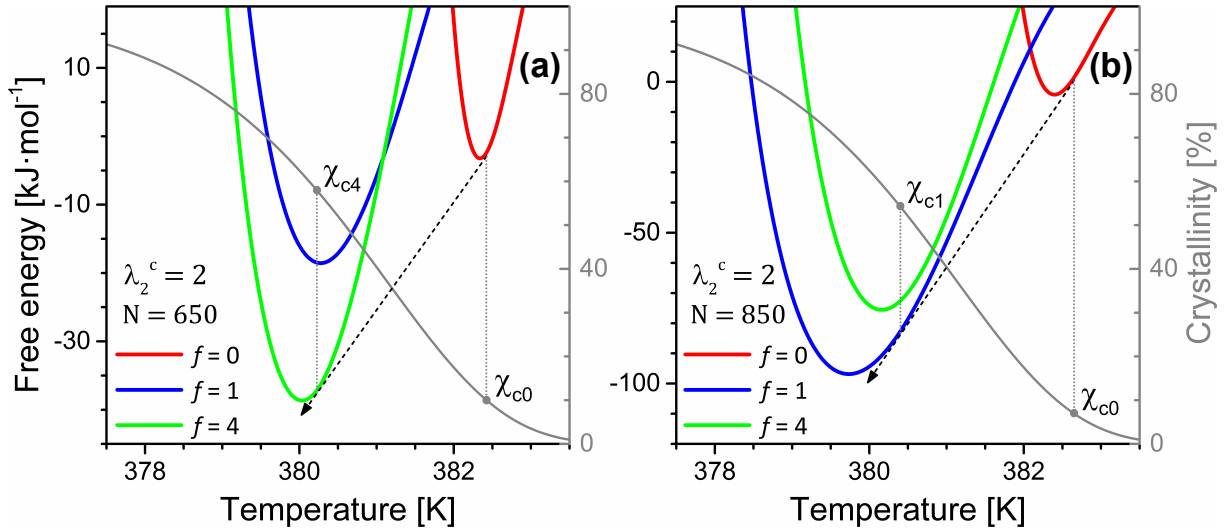


**Figure 12:** The free energy of crystallization (referred to left axes) and crystallinity (referred to right axes) as a function of temperature  $T$ . The free energy curves were calculated for HDPE in case of  $\lambda_2^c = 2$ , different values of chain links  $N = 650$  (a),  $N = 850$  (b), and different numbers of crystal folds  $f$ . The black dashed lines represent the common tangent lines and indicate the crystallization path at cooling [92].

Note that crystallization conditions in the present theory are assumed so that the crystallization is an equilibrium thermodynamic process. This enables to plot, as shown in Figure 12, the free energies of crystallization in case of  $N = 650$  (Figure 12a),  $N = 850$  (Figure 12b) when  $\lambda_2^c = 2$ , and the crystallinity as a function of temperature calculated theoretically on the basis of Equation (66) and used for the calculation of  $\Delta F_f(T, \lambda_2^c)$  presented in Figure 11. According to the lever rule, the composition of the entire crystallizing network of monodisperse chains is determined by drawing the common tangent line (black dashed line in Figure 12a–b) to the free energy curves, where arrows indicate the crystallization path at cooling. The values  $\chi_{c0}$ ,  $\chi_{c1}$ , and  $\chi_{c4}$  were obtained as the crystallinity corresponding to the intercepts of the common tangent line with the free energy curves. Figure 12 is shown to give better understanding of used assumptions and parameters, such as



$\chi_{c0}$  and  $\chi_{cf}$ , however the current theory comprises non-isometric conditions. Therefore, the free energy of crystallization  $\Delta F_f(T, \lambda_2^c)$  is calculated for any given value of draw ratio, that is,  $\lambda_2^c$  remains a variable.

As discussed above, the extended-chain crystallites have a lower free energy at the onset of crystallization of HDPE. The formation of these crystallites results in an increase of crystallinity from 0 to  $\chi_{c0}$  value. According to the calculation of the free energy of crystallization (Figure 11–12), further cooling leads to the crystal growth and the transformation of the initial extended-chain crystals into the crystals with folded-chain morphology, since the latter has the lowest free energy. When temperature is lowered below some critical point, the free energy of crystallization reaches its minimum, crystallization ceases, and crystallinity possesses  $\chi_{cf}$  value. In case of an ideal monodisperse network all network chains have formed crystallites with  $f$  folds at this stage. Thus,  $\chi_{cf}$  is a maximum crystallinity value at a given number of chain links and deformation. However, during crystallization  $\chi_c$  value is defined as:

$$\chi_c = G_0 \cdot \chi_{c0} + G_f \cdot \chi_{cf}, \quad (68)$$

where  $G_0$  and  $G_f$  are the fractions of network chains having crystallinity  $\chi_{c0}$  and  $\chi_{cf}$ , 0 and  $f$  folds in the crystal, respectively. Both  $G_0$  and  $G_f$  values change with increasing crystallinity, only their sum is constant and equals 1. Hence, the system of equations can be written:

$$\begin{cases} G_0 \cdot \chi_{c0} + G_f \cdot \chi_{cf} = \chi_c \\ G_0 + G_f = 1 \end{cases}. \quad (69)$$

Solving this system the fractions  $G_0$  and  $G_f$  are as follows:

$$G_0 = \frac{\chi_{cf} - \chi_c}{\chi_{cf} - \chi_{c0}}, \quad G_f = \frac{\chi_c - \chi_{c0}}{\chi_{cf} - \chi_{c0}}. \quad (70)$$

Using designations (68) and (70) the lowest total specific free energy of crystallization of the network  $\Delta F_{tot}^{sp}(T, \lambda_2^c)$  can be written as:

$$\Delta F_{tot}^{sp}(T, \lambda_2^c) = \nu_c \cdot [G_0 \cdot \Delta F_0(T, \lambda_2^c) + G_f \cdot \Delta F_f(T, \lambda_2^c)], \quad (71)$$

where  $\nu_c$  is the crosslink density of covalent polymer network.

The expression (71) enables calculation of the applied nominal stress  $\sigma_{0N}$ , which is the first derivative of the total specific free energy with respect to draw ratio:

$$\sigma_{0N} = \nu_c \frac{\partial \Delta F_{tot}^{sp}(T, \lambda_2^c)}{\partial \lambda_2^c} = \nu_c \cdot \left[ G_0 \frac{\partial \Delta F_0(T, \lambda_2^c)}{\partial \lambda_2^c} + G_f \frac{\partial \Delta F_f(T, \lambda_2^c)}{\partial \lambda_2^c} \right], \quad (72a)$$

$$\begin{aligned} \frac{\partial \Delta F_f(T, \lambda_2^c)}{\partial \lambda_2^c} = & \Lambda RT \cdot \left[ \frac{3}{5N\theta^3} (\lambda_2^c)^3 - \frac{6\varphi\delta}{5N\theta^3} (\lambda_2^c)^2 + \frac{1}{\theta} \left( 1 + \frac{9\varphi^2}{5N^2\theta^2} - \frac{1}{N\theta} \right) \lambda_2^c - \right. \\ & \left. - \frac{1}{\theta} \left( 1 + \frac{3\varphi^2}{5N^2\theta^2} - \frac{1}{N\theta} \right) \cdot \frac{1}{(\lambda_2^c)^2} - \frac{4}{5N\theta^3} \frac{1}{(\lambda_2^c)^3} + \right. \\ & \left. + \left( \frac{1}{5N\theta^3} - \frac{3\varphi^3\delta}{5N^2\theta^3} - \frac{\varphi\delta}{\theta} \left[ 1 - \frac{1}{N\theta} \right] \left[ 1 + \frac{1}{20N} \right] \right) \right], \end{aligned} \quad (72b)$$

where  $\theta = \left( 1 - \chi_{cf} - \frac{\psi_f}{N} \right)$  as mentioned above,  $\varphi$  also depends on number of folds  $f$  and is defined according to Equation (60b).

Thus, Equations (72) represent a stress-strain-temperature relationship for loaded crystallizing covalent network. The sought temperature dependent deformation of covalent network under constant load during non-isothermal crystallization  $\lambda_2^c$  can be expressed from Equations (72) and converted into the strain  $\varepsilon_2^c$  as follows:

$$\varepsilon_2^c = \lambda_2^c - 1. \quad (73)$$

#### 4.2.3. The total strain as a function of temperature

As mentioned in *Section 2.5.*, the two-phase model shown in Figure 7 can be scarcely used to describe the thermo-mechanical behavior of the amorphous polymers. However, it is just the case for crystallizable polymers. Hence, based on the work of Liu *et al.* [63] the thermal contraction of cross-linked semicrystalline polymers during cooling is taken into account and can be written as:

$$\varepsilon_{TC} = \Delta T \cdot (\alpha_c \chi_c + \alpha_a (1 - \chi_c)) = (T - T_{pr}) \cdot (\alpha_c \chi_c + \alpha_a (1 - \chi_c)), \quad (74)$$

where  $T_{pr}$  is the initial programming temperature of cooling run ( $T_{pr} > T_m$ ),  $\alpha_c$  is a linear expansion coefficient of the crystalline phase,  $\alpha_a$  is a linear expansion coefficient of the amorphous phase,  $\chi_c$  is the crystallinity as a function of temperature given by Equation (66).

Finally, referring to the mechanical model depicted in Figure 9c and to the arrangement of strains in Equation (8a), the theoretically derived total temperature dependent strain of cross-linked semicrystalline polymer under constant load during non-isothermal crystallization at cooling is expressed as follows:

$$\varepsilon_T^c = \varepsilon_{TC} + \varepsilon^c = \varepsilon_{TC} + \varepsilon_1^c + \varepsilon_2^c, \quad (75)$$

where thermal contraction  $\varepsilon_{TC}$  is given by Equation (74), the strain of entangled slipped molecules  $\varepsilon_1^c$  is given by Equation (42), and the strain of crystallizing covalent network is given by Equations (72)–(73).

### 4.3. Model behavior at heating above $T_m$ under constant load

The thermo-mechanical behavior of cross-linked semicrystalline polymers at heating is schematically illustrated in Figure 9d.

Firstly, similarly to the consideration presented in Section 4.2.1., the viscous flow of entangled macromolecules at heating is described by the following expressions:

$$\sigma_1^h = \frac{3}{2} \nu_e RT \varepsilon_1^h, \quad (76a)$$

$$\dot{\varepsilon}_1^h = -2 \frac{V_h}{V_m} \cdot \frac{k_B T}{h} \cdot \exp\left(-\frac{U}{k_B T}\right) \cdot \sinh\left(\frac{V_h \sigma_2^h}{2k_B T}\right), \quad (76b)$$

where minus in (76b) is used to account that heating results in a recovery of previously stored deformation, therefore strain rate is negative.

Using Equation (8b) the stress acting on a dashpot can be expressed:

$$\sigma_2^h = \sigma_0 - \sigma_1^h = \sigma_0 - \frac{3}{2} \nu_e RT \varepsilon_1^h. \quad (77)$$

Substitution of Equation (77) in (76b) implies:

$$\dot{\varepsilon}_1^h = -2 \frac{V_h}{V_m} \cdot \frac{k_B T}{h} \cdot \exp\left(-\frac{U}{k_B T}\right) \cdot \sinh\left(\frac{V_h \sigma_0}{2k_B T} - \frac{3}{4} \frac{V_h}{k_B} \nu_e R \varepsilon_1^h\right). \quad (78)$$

Taking into account constant heating rate  $\frac{dT}{dt} = \gamma$ , using constant nominal stress  $\sigma_{0N}$  instead of true stress as expressed in Equation (17), and following the reasonable approximation (14), Equation (78) is transformed:

$$\frac{d\varepsilon_1^h}{dT} = \frac{V_h^2}{V_m \gamma h} \cdot \exp\left(-\frac{U}{k_B T}\right) \cdot \left(\frac{3}{2} \nu_e RT \varepsilon_1^h + \sigma_{0N} (1 + \varepsilon_1^h)\right). \quad (79)$$

Note that Equation (79) is a non-homogeneous first-order linear differential equation, which is completely similar to Equation (18) used to describe the viscous low of entangled macromolecules at cooling. Thereby, the solution of (79) is sought based on the same assumptions, basic equations, and overall theoretical treatment presented in Section 4.2.1.

Hence, the temperature dependent strain of entangled slipped macromolecules at heating is given by:

$$\varepsilon_1^h = \frac{\sigma_{0N}}{3/4\nu_e U - \sigma_{0N}} + \left( \varepsilon_{01} - \frac{\sigma_{0N}}{3/4\nu_e U - \sigma_{0N}} \right) \cdot \exp \left[ -\frac{2V_h^2}{V_m} \cdot \frac{3/4\nu_e U - \sigma_{0N}}{\gamma h} T \cdot \exp \left( -\frac{U}{RT} \right) \right]. \quad (80)$$

*Secondly*, it is obvious that a recovery of strain stored in the covalent network is caused by melting of the same crystal structure formed during previous crystallization at cooling. Therefore it is assumed that melting of covalent polymer network can be described by the free energy change consisting of the same terms, which appear in Equation (44) presented in *Section 4.2.2.*, but with opposite signs. Following the same assumptions, basic equations, and solutions as described in *Section 4.2.2.*, the stress-strain-temperature relationship for the covalent network under constant load heated above melting point  $T_m$  is written as:

$$\sigma_{0N} = -\nu_c \frac{\partial \Delta F_{tot}^{sp}(T, \lambda_2^h)}{\partial \lambda_2^h} = -\nu_c \cdot \left[ G_0 \frac{\partial \Delta F_0(T, \lambda_2^h)}{\partial \lambda_2^h} + G_f \frac{\partial \Delta F_f(T, \lambda_2^h)}{\partial \lambda_2^h} \right], \quad (81a)$$

$$\begin{aligned} \frac{\partial \Delta F_f(T, \lambda_2^h)}{\partial \lambda_2^h} = & \Lambda RT \cdot \left[ \frac{3}{5N\theta^3} (\lambda_2^h)^3 - \frac{6\varphi\delta}{5N\theta^3} (\lambda_2^h)^2 + \frac{1}{\theta} \left( 1 + \frac{9\varphi^2}{5N^2\theta^2} - \frac{1}{N\theta} \right) \lambda_2^h - \right. \\ & \left. - \frac{1}{\theta} \left( 1 + \frac{3\varphi^2}{5N^2\theta^2} - \frac{1}{N\theta} \right) \cdot \frac{1}{(\lambda_2^h)^2} - \frac{4}{5N\theta^3} \frac{1}{(\lambda_2^h)^3} + \right. \\ & \left. + \left( \frac{1}{5N\theta^3} - \frac{3\varphi^3\delta}{5N^2\theta^3} - \frac{\varphi\delta}{\theta} \left[ 1 - \frac{1}{N\theta} \right] \left[ 1 + \frac{1}{20N} \right] \right) \right]. \end{aligned} \quad (81b)$$

The crystallinity as a function of temperature at heating is included in expressions for chain fractions  $G_0$  and  $G_f$  (Equations (70)) and is defined similarly to Equation (66):

$$\chi_c = A \cdot \exp \left[ -K \left( \frac{T}{T_{sw}^h} \right)^m \right], \quad (82)$$

where  $T_{sw}^h$  is switching transition temperature at heating, which is assumed to be melting temperature of a semicrystalline polymer network in the present consideration.

As before, the strain of covalent network  $\varepsilon_2^h$  as a function of temperature can be simply expressed from Equations (81) using no additional assumptions.

Also, the thermal expansion of cross-linked semicrystalline polymers can be written in the same manner as Equation (74), namely:

$$\varepsilon_{TE} = (T - T_{low}) \cdot (\alpha_c \chi_c + \alpha_a (1 - \chi_c)), \quad (83)$$

where  $T_{low}$  is the initial temperature of heating run, that is, the lowest temperature of the two-way shape-memory experiment ( $T_{low} < T_c$ ).

Thus, the expression for the temperature dependent strain of cross-linked semicrystalline polymers at heating is given as:

$$\varepsilon_T^h = \varepsilon_{TE} + \varepsilon_1^h + \varepsilon_2^h. \quad (84)$$

Along with equations (80)–(83), which are included in (84), Equation (84) will be used for simulation of the experimental data of the two-way shape-memory behavior of PEs under study at heating.

## **5. Investigation and modeling the shape-memory behavior of cross-linked polyethylene and ethylene-copolymers**

### **5.1. Materials and processing**

PEs under study have been commercially available products (Dow Chemical, Schkopau, Germany), namely high-density polyethylene – HDPE (KS 10100 UE) and two metallocene-catalyzed homogeneous ethylene-1-octene copolymers (EOCs) with approximately 30 and 60 hexyl branches per 1000 C – EOC30 (AFFINITY™ PL 1280G) and EOC60 (ENGAGE 8200), respectively. The relevant parameters of these materials are given in Table 1. Pellets of the processed polymers were impregnated with 2,5-bis(t-butylperoxy)-2,5-dimethylhexane (DHBP) via mechanical mixing in a hermetic flask and diffusion of DHBP into the polymer pellets for three days at room temperature. The impregnated EOC30 and EOC60 pellets contained the nominal DHBP concentration of 2, 3, and 4 wt%, whereas impregnated HDPE contained 2 wt% of the peroxide. Subsequently, DHBP impregnated polymers were homogenized using a single-screw mixing extruder (Brabender® GmbH & Co. KG, Duisburg, Germany) at 403 K.

The processing experiments show that the applied cross-linking method is suitable for PEs with the chosen melt-flow index MFI (Table 1) measured by means of the melt index test apparatus MI 21,6 (Göttfert Werkstoff-Prüfmaschinen GmbH, Buchen, Germany). DHBP as a low-molecular fluid substance can act as a lubricant during processing, i.e., the effective MFI values of DHBP-impregnated PEs are evidently higher and the viscosities are lower than that of pure materials. Thus, the DHBP can conduce to the mixing process at 403 K. The extrudates were compression molded to films with a thickness of 1 mm and cross-linked at a temperature of 463 K in the press under load.

The crosslink density  $\nu_c$  of PEs under study was estimated by means of swelling procedure on the basis of Flory-Rehner equation [103–104]. The swelling measurements were performed on the samples stored in xylene at 383 K after at least 10 hours using the gel of cross-linked HDPE and EOCs obtained after extraction of the soluble fraction as described by Sajkiewicz *et al.* [105] and Smedberg *et al.* [106]. The extraction experiments were carried out in a *Soxhlet* extractor in xylene at 383 K for at least 28 hours using samples with a mass about 0.7 g partitioned into 65 pieces. The values of crosslink density  $\nu_c$  are listed in Table 1.

Note that the relatively homogenous distribution of crosslink points may be expected only in highly-branched and, correspondingly, low crystalline EOC60, whose very small

**Table 1:** Designations as well as some physical and molecular parameters of used PEs.

Designation	Melt-Flow Index (MFI) <sup>a)</sup> [dg·min <sup>-1</sup> ]			$T_m$ <sup>b)</sup> [K]	Density [kg·m <sup>-3</sup> ]	Mass-Average Molecular Mass $\bar{M}_w$ [kg·mol <sup>-1</sup> ]	Polydispersity $\bar{M}_w/\bar{M}_n$ [-]	Degree of branching [CH <sub>3</sub> /1000C]	Crosslink density $\nu_c$ [mol·m <sup>-3</sup> ]
	463 K/ 2.16 kg	463 K/ 5.0 kg	403 K/ 5.0 kg						
HDPE	3.0	10.1	2.5	405	955	99	4.3	~ 0	110 140
EOC30	5.0	17.7	4.2	369	900	64	2.3	~ 30	220 270
EOC60	4.4	15.9	3.4	332	870	87	2.5	~ 60	150 190

a) measured by test apparatus MI 21,6 (Göttfert);

b) obtained by DSC [34].

crystallites, e.g., fringed micelles [107], are dispersed in the continuous and quasi homogenous amorphous phase. The peroxide distribution in medium crystalline EOC30 and high crystalline HDPE homogenized in the extruder is definitely no more homogeneous at molecular level after subsequent cooling of the extrudates due to reallocation of the peroxide caused by crystallization. The originated crystalline regions are free from peroxide by definition. Thereupon, reheating until 383 K obviously resulted in uncross-linking of these nano-regions, which retain the ability to crystallization. Hence, the experimentally obtained average values of crosslink density  $\nu_c$  of EOC30 and especially of HDPE are definitely lower than the true local crosslink density of the amorphous phase [34].

## 5.2. Methods of materials characterization

### 5.2.1. Simultaneous DMTA and shape-memory tests under constant load

Dynamic-mechanical thermal analysis (DMTA) of specimens loaded with a static force was carried out in tensile mode using a mechanical spectrometer with measuring head Mark III (Rheometric Scientific Inc., Piscataway, New Jersey, USA). The miniature tensile test

specimens shaped as shouldered test bars with the cross-sectional area of  $2 \times 1 \text{ mm}^2$  and initial clamps distance between 6 and 12 mm were tested at the frequency of 1 Hz during the thermal loops at heating and cooling rate of  $2 \text{ K} \cdot \text{min}^{-1}$ . The initial static stress value amounted between 0.3 and 1.2 MPa. The combination of low dynamical deformation with amplitude of 0.1 % along with relatively high static load enabled to obtain simultaneously the temperature dependences of dynamical storage modulus  $E'$  and of macroscopic strain induced by static load and reached some hundred percent. Thus, the thermal loops of storage modulus  $E'$  as well as shape-memory creep and recovery strain in the first cooling and second heating runs, respectively, were measured simultaneously.

### **5.2.2. Differential scanning calorimetry**

Melting and crystallization behavior of PEs under study was investigated with a power compensation DSC 7 equipped with the liquid nitrogen accessory CCA-7 (PerkinElmer LAS GmbH, Rodgau, Germany) for controlled cooling at a rate of  $10 \text{ K} \cdot \text{min}^{-1}$  and heating at a rate of  $20 \text{ K} \cdot \text{min}^{-1}$ . The differential scanning calorimetry (DSC) data were collected for two sets of samples of each cross-linked PE: the first set was cut from undeformed PEs in their original permanent shapes, whereas the second set was cut from the drawn samples crystallized after cooling under load with nominal stress  $\sigma_{0N}$  of 1 MPa in case of HDPE (residual strain at 273 K is about 109%), 0.6 MPa in case of EOC30 (residual strain at 273 K is about 104%), and 0.3 MPa in case of EOC60 (residual strain at 273 K is about 70%) during specific thermo-mechanical experiment described above. Each drawn sample was sealed in 20 ml aluminum pan between two thin films of polytetrafluoroethylene (PTFE) in order to ensure free mobility of a sample during recovery of its original shape at heating. The sample mass was about 8 mg. Heat-flow rate raw data were corrected for the instrumental asymmetry and converted into temperature dependencies of apparent specific heat capacity  $c_p(T)$ . The measured  $c_p(T)$  values in conjunction with theoretical values of specific heat capacity for crystalline and amorphous polyethylene taken from the advanced thermal analysis system ATHAS [108] were utilized for the calculation of enthalpy-based crystallinity as a function of temperature  $\chi_c(T)$  on the basis of the two-phase model as described by Mathot *et al.* [109].

### **5.2.3. Two-way shape-memory behavior**

The shape-memory investigation was carried out in tensile mode using a mechanical spectrometer measuring head Mark III (Rheometric Scientific Inc., Piscataway, New Jersey,



USA). The samples of cross-linked HDPE, EOC30, and EOC60 shaped as shouldered test bars with the cross-sectional area of  $2 \times 1 \text{ mm}^2$  were tested during the specific thermo-mechanical experiment at an initial clamps distance of 6 mm. The specimens were loaded by different nominal stress  $\sigma_{0N}$ , which is defined as force divided by the *initial* cross-sectional area, at the programming temperatures  $T_{pr}$  above the corresponding melting temperature, namely,  $T_{pr} = 438 \text{ K}$  in case of HDPE,  $T_{pr} = 413 \text{ K}$  and  $T_{pr} = 393 \text{ K}$  in case of EOC30 and EOC60, respectively. Such loading entailed the initial strain  $\varepsilon_{ini}$ . Subsequent cooling under constant load to the lowest temperature  $T_{low}$  of 273 K at an average rate of  $2 \text{ K} \cdot \text{min}^{-1}$  resulted, at first, in the relatively slight creep of the samples by value  $\varepsilon_{cr}$  prior to crystallization and, secondly, in the considerable anomalous elongation of the samples by strain increment  $\Delta\varepsilon_{inc}$  in the temperature range of crystallization. Afterwards, the loaded specimens were thermally equilibrated for 5 min at  $T_{low}$  and then heated to the programming temperature  $T_{pr}$  at a rate of  $2 \text{ K} \cdot \text{min}^{-1}$ . During melting of the crystalline phase the specimens considerably contracted by strain decrement  $\Delta\varepsilon_{dec}$ . After thermal equilibration for 5 min at  $T_{pr}$  the thermo-mechanical cycle was repeated. The strain was measured as a function of temperature during the described thermo-mechanical experiment.

Because any difference between the measured temperature of a sample and its true value occurs in each cooling/heating tensile experiment using a mechanical spectrometer, a calibration sample of polyamide 6 with embedded conductor of K-type thermocouple (chromel–alumel) was used to determine the true temperature of the specimen during the shape-memory experiment. Another thermocouple was connected to a data logger measuring the electrical potential difference and, correspondingly, the real temperature of the sample. The specimen was tested in a mechanical spectrometer under the same thermal conditions of shape-memory experiment as described in the previous paragraph. The temperature sets from the spectrometer sensor and thermocouple were registered synchronously and their difference was approximated by the polynomial function. Received correction function was used to calculate the true temperature of specimens during shape-memory investigation.

#### **5.2.4. Transmission electron microscopy**

The high-resolution transmission electron microscopy (TEM) images of two sets of PEs samples – slowly crystallized undeformed samples and drawn samples crystallized after cooling under load during the two-way SME as also described in *Section 5.2.2.* – were obtained on a LIBRA200 MC (Carl Zeiss Microscopy GmbH, Oberkochen, Germany).

Sample preparation was carried out at ultramicrotome EM UC6/FC6 (Leica Microsystems GmbH, Wetzlar, Germany). The first step for sample preparation was the manufacture of cross-sections of the undeformed and drawn specimens at 123 K under dry nitrogen atmosphere. Afterwards cross-sections were stained in RuO<sub>4</sub> vapor for 24 hours and then degassed for further 24 hours. Finally, the ultrathin sections were sliced at 123 K under dry nitrogen atmosphere and transferred for image acquisition onto copper grids coated with carbon film. The place of sampling of drawn PEs is schematically shown in Figure 13.

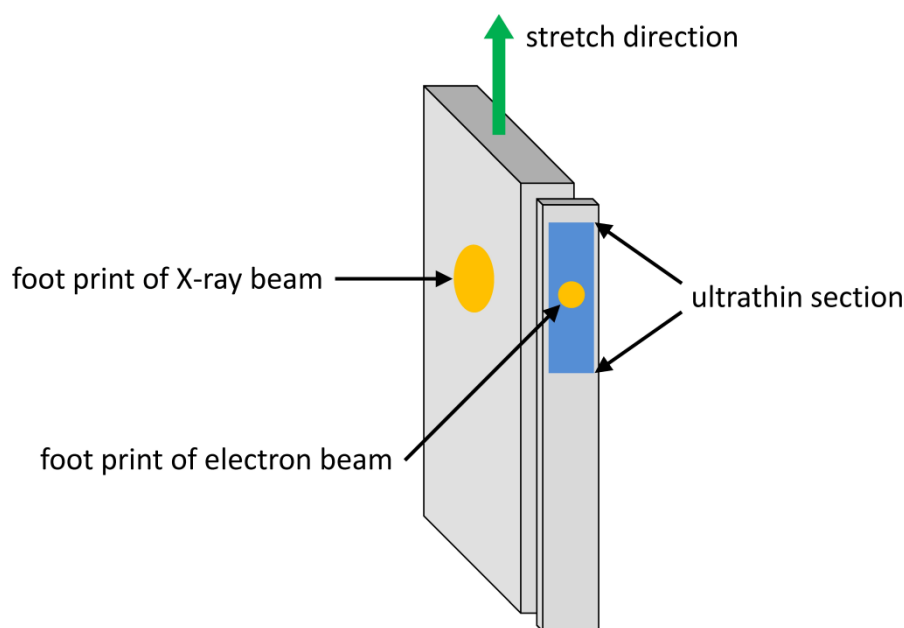


**Figure 13:** Schematic representation of the exposure of the drawn PEs specimens to X-ray beam during wide- and small-angle X-ray scattering as well as the preparation of the stretched specimens for TEM investigation.

### 5.2.5. Wide- and small-angle X-Ray scattering

Wide- and small-angle X-Ray scattering (WAXS and SAXS) investigation was performed for two sets of samples – slowly crystallized undeformed samples and stretched samples crystallized after cooling under load during the two-way shape-memory experiment (Section 5.2.2.). WAXS patterns were collected in transmission geometry for analysis of the orientation of the crystals using an X-ray flat film camera (Molecular Data Corporation, Cleveland, Ohio, USA) equipped with a 0.5 mm pinhole collimation system. SAXS

measurements were carried out at a 3-fold pinhole system (self-construction) with rotating anode (Rigaku Corporation, Tokyo, Japan) using Cu-K $\alpha$  radiation monochromatized by primary confocal multilayer optic (Max-Flux® Optics, now: Rigaku Corporation, Tokyo, Japan) and area detection system MarCCD (now: Rayonix, L.L.C., Evanston, USA). The wavelength of the Ni-filtered Cu-K $\alpha$  radiation in both WAXS and SAXS was 0.15418 nm, and the sample-to-detector distance was about 30 mm. The photographs were taken with the primary beam being normal to the stretch direction of drawn films as shown in Figure 13.

The results will be discussed based on 2D scattering pattern. Intensity plots  $I(q)$  were created by means of sectorial integration over  $\pm 5^\circ$  to the orientation on equator in case of WAXS and 360°-integration in case of SAXS. The scattering curves of SAXS are displayed as  $I(q) \cdot q^2$  data vs. scattering vector  $q = 2\pi/d$  without background subtraction and  $I(\chi)$  vs. azimuthal angle  $\chi$ , respectively.

## 6. Results and discussion

### 6.1. Viscoelastic behavior and shape-memory effect under constant load

The clear manifestation of the two-way invertible SME can be observed obviously in each crystallizable covalent polymer network if suitable values of crosslink density  $\nu_c$  and load  $\sigma_{0N}$  are employed [47–51,54]. The results demonstrated in Figure 14 prove that the linear high-

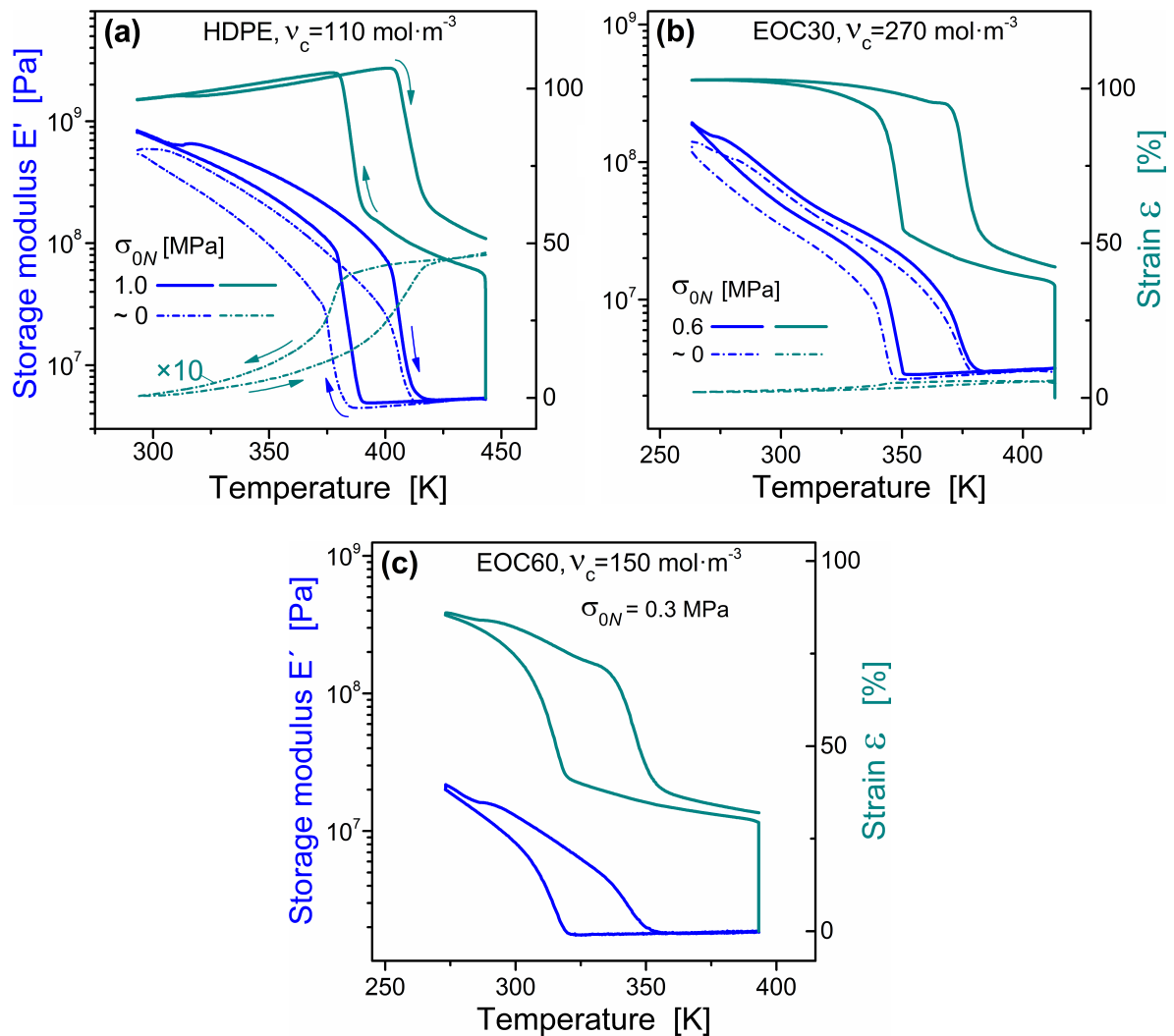


**Figure 14:** Simultaneously measured temperature dependencies of corrected storage modulus  $E'$  and of thermally induced shape-memory creep/recovery strain  $\epsilon$  of unconstrained and loaded samples of nearly linear (a) and short-chain branched PEs (b–c) with different degree of branching and crosslink density  $\nu_c$ . Arrows in figure (a) indicate cooling and heating runs; strain of unconstrained HDPE is 10 times magnified for better resolution.

density and short-chain branched PEs cross-linked by peroxide are not an exception to this statement.

The simultaneously measured temperature dependencies of strain  $\varepsilon$  and storage modulus  $E'$  of cross-linked linear HDPE, medium- and highly-branched EOC30 and EOC60, respectively, performed under constant load exhibit (Figure 14) the distinct occurrence of the *anomalous macroscopic elongation* (thermally induced shape-memory creep) accompanied with the stepwise increase in  $E'$  during non-isothermal crystallization at cooling and the pronounced contraction (thermally induced shape-memory recovery) along with the stepwise decrease in  $E'$  during subsequent melting at heating.

The values of  $E'$  were corrected taking into consideration the change of sample length and, correspondingly, of the cross-sectional area. Assuming that in the first approximation polymer networks are incompressible, i.e., the sample volume calculated as the product of its length and cross-sectional area is constant, the corrected  $E'$  value can be obtained by means of simple transformation of measured values of storage modulus  $E'_{meas}$ :

$$E' = E'_{meas} \cdot (l_0 + \Delta l)/l_0, \quad (85)$$

where  $l_0$  and  $\Delta l$  are the initial length and absolute deformation of a sample, respectively.

As seen from Figure 14, the stepwise elongation and increase of  $E'$  at cooling of cross-linked PEs occur at the identical temperatures lying in the range of crystallization. Such a behavior depicts directly that just crystallization under load causes the anomalous elongation of PE networks. The comparison of corrected temperature dependencies of  $E'$  obtained for loaded and unconstrained samples (Figure 14a–b) allows concluding that cross-linked PEs under load demonstrate higher values of crystallization and melting temperatures ( $T_c$  and  $T_m$ ), higher  $E'$  values in entire temperature range, as well as higher  $E'$  increment and decrement during non-isothermal crystallization and melting, respectively.

The described behavior can be explained as a result of the reduction of entropy of polymer chains in the course of uniaxial extension [87] after application of a constant load during the two-way SME and, consequently, as a result of the initial ordering of network chains already in the amorphous phase that contributes to a formation of crystal precursors and leads to the crystallization at higher temperature similarly to quiescent flow-induced crystallization of entangled polymer melt [110], as also discussed in the next *Section 6.2*. It is well known that the crystalline phase, which is crystallized at higher  $T_c$ , melts at higher  $T_m$  as well [85]. Besides, the lamellar orientation and the formation of crystalline texture result in significant increase in  $E'$  (see also *Sections 6.2. and 6.4.*) [86].

## 6.2. Melting and crystallization behavior of cross-linked polyethylenes

Temperature dependencies of apparent specific heat capacity  $c_p(T)$  shown in Figures 15a–b allow discussing the melting and crystallization behavior of stretched samples of cross-linked PEs prepared by crystallization during cooling under load of 1 MPa for HDPE, EOC30 and EOC60.

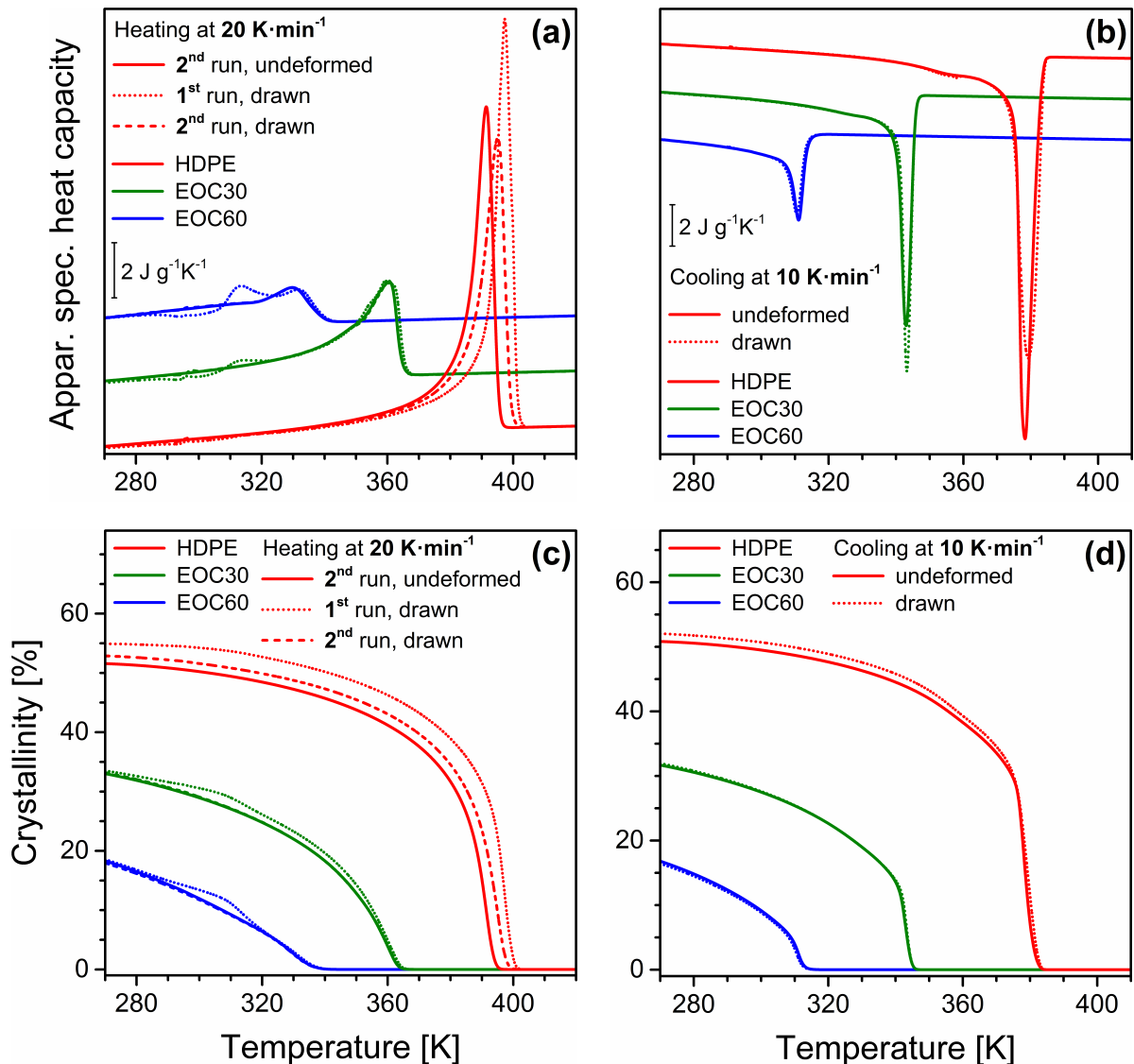


**Figure 15:** Apparent specific heat capacity (a–b) and enthalpy-based crystallinity as functions of temperature (c–d) at heating and cooling (cooling runs preceded the second heating) of undeformed samples of cross-linked HDPE ( $v_c = 110 \text{ mol}\cdot\text{m}^{-3}$ ), EOC30 ( $v_c = 270 \text{ mol}\cdot\text{m}^{-3}$ ), and EOC60 ( $v_c = 190 \text{ mol}\cdot\text{m}^{-3}$ ) as well as their stretched samples. The stretched PEs were preliminarily crystallized under load of 1 MPa for HDPE, 0.6 for EOC30, and 0.3 MPa for EOC60 during cooling stage of the two-way shape-memory cycle.

0.6 MPa for EOC30, and 0.3 MPa for EOC30 in comparison with undeformed samples as reference objects. Enthalpy-based crystallinity as a function of temperature calculated on the basis of DSC curves is depicted in Figures 15c–d.

**Table 2:** DSC peak temperatures of melting and crystallization (Figure 15a–b) as well as enthalpy-based crystallinity (Figure 15c–d) at room temperature of undeformed and stretched samples of cross-linked HDPE, EOC30, and EOC60 crystallized under load during cooling stage of the two-way shape-memory cycle.

Samples		Melting temperature $T_m$		Crystallization temperature $T_c$	Crystallinity $\chi_c$ at 298 K		
		[K]			[K]	[%]	
		1 <sup>st</sup> heat. run	2 <sup>nd</sup> heat. run			1 <sup>st</sup> heat. run	cooling run
HDPE	undeformed	–	391.4	378.3	–	49.7	50.4
	drawn	397.2	395.1	379.2	54.3	50.9	51.8
EOC30	undeformed	–	360.5	343	–	27.8	29.6
	drawn	361.7	360.6	343.2	30.8	27.9	29.3
EOC60	undeformed	–	329.7	311.1	–	9.9	12.4
	drawn	332.1	330	310.8	13.7	9.7	12.3

Table 2 lists the melting and crystallization temperatures obtained as peak temperatures of corresponding DSC traces as well as values of crystallinity at room temperature (298 K). Note that the endothermic melting process measured in the first heating run reflects the preceding mechanical treatment and thermal history of specimens, whereas in the second heating run the shape of DSC melting trace is affected only by conditions of non-isothermal crystallization in previous cooling run [111–114]. The first heating runs of drawn cross-linked EOC30 and EOC60 samples exhibit a minimum followed by a maximum arising in the temperature range between approximately 280 K and 325 K and caused by annealing at room temperature during storage of prepared samples, as it was already shown for uncross-linked EOCs and other random copolymers of ethylene with  $\alpha$ -olefins especially with high degree of branching [109,111–114].

As it is seen from Table 2 and Figure 15, melting temperatures  $T_m$  and crystallinity in entire temperature range of preliminarily drawn cross-linked HDPE, EOC30, and EOC60 in the first heating run are higher as compared to their values for undeformed samples. This can be explained as a result of the initial ordering of network chains in the amorphous phase as it was mentioned in the previous section. As is well known, the crystalline phase, which is crystallized at higher  $T_c$ , melts at higher  $T_m$  as well [85]. Such explanation is supported by the crystallization behavior at cooling (Figure 15b) of previously melted samples during the first heating run.

In spite of the fact that stretched samples were placed between two thin films of PTFE as described in *Section 5.2.* in order to ensure free recovery of their permanent shapes during the first heating run, crystallization temperatures  $T_c$  of previously melted samples are higher than  $T_c$  of undeformed specimens, especially for HDPE. This is apparently caused by the incomplete recovery of the initial shape after processing. The second heating runs following the cooling of these samples are also characterized by higher melting temperatures  $T_m$ . As it is seen from Table 2, the enthalpy-based crystallinity of PEs under study is sufficiently different. Furthermore, the deformation of samples results in higher crystallinity values as shown in Figure 15c–d as well as in Table 2 that evidences the higher ordering of the stretched samples during crystallization and is more distinct for HDPE.

### **6.3. Two-way shape-memory behavior**

#### **6.3.1. Effect of loading**

The strain as a function of temperature shown in Figure 16a,c,e represents the evolution of thermo-mechanical response of HDPE, EOC30, and EOC60 with the highest reached crosslink densities of 110, 270, and 190 mol·m<sup>-3</sup>, respectively, loaded by different nominal stresses during the cyclic two-way shape-memory experiment. As it is seen from Figure 16a, only the HDPE sample loaded by 0.9 MPa does not reveal typical two-way shape-memory behavior, while the other samples of PEs under study at different loads exhibit the distinct two-way SME. Such peculiar mechanical behavior of HDPE at 0.9 MPa cannot be appropriately explained at this stage, however, it will be specifically discussed on the basis of the results of modeling presented in *Section 6.6.2.* The important characteristics of the two-way shape-memory performance like initial strain  $\varepsilon_{ini}$ , non-isothermal entropy-elastic creep  $\varepsilon_{cr}$ , crystallization-induced strain increment  $\Delta\varepsilon_{inc}$ , and melting-induced strain decrement  $\Delta\varepsilon_{dec}$  mentioned in *Section 5.2.* are exemplified in Figure 16a for HDPE loaded by 1.2 MPa.



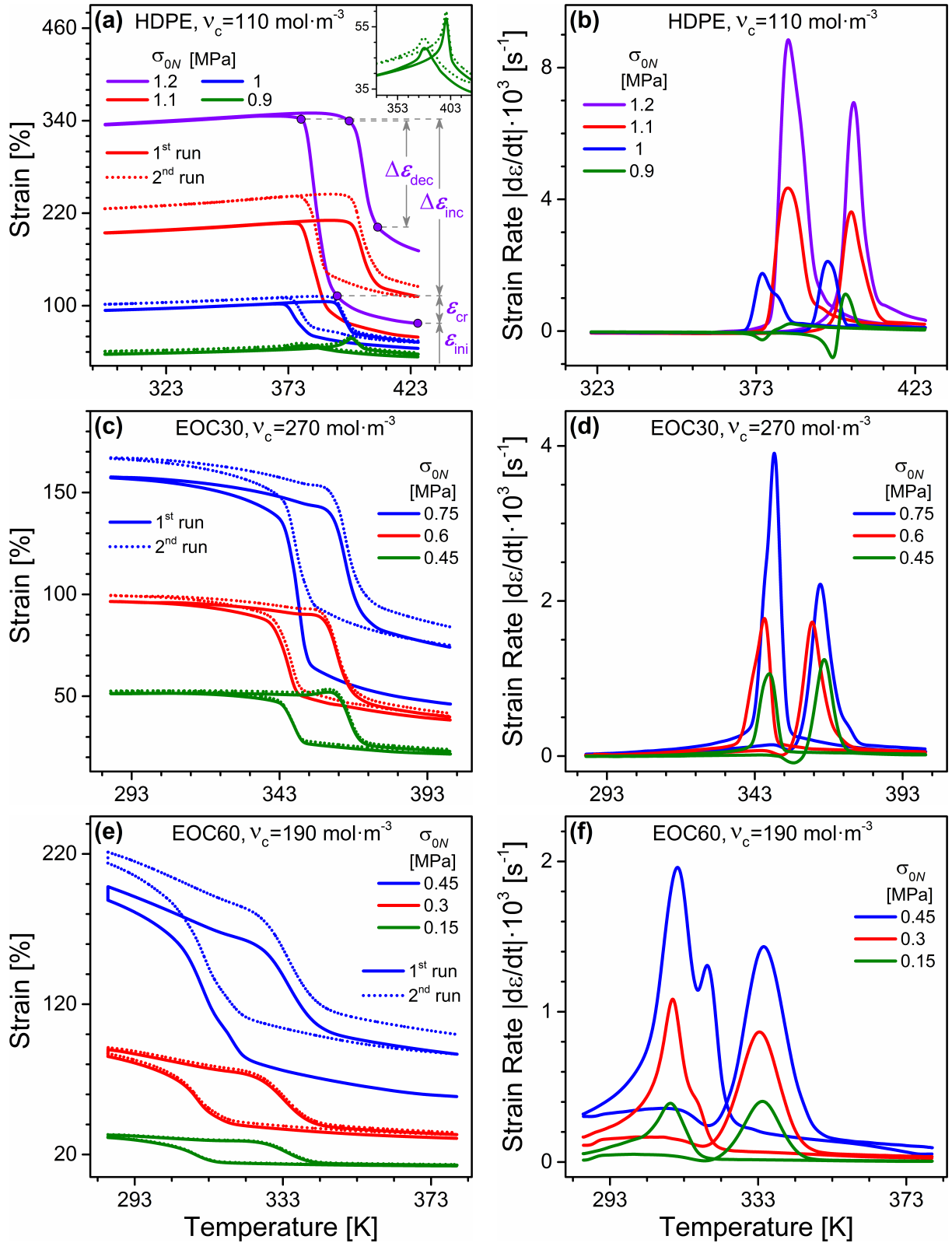


**Figure 16:** The effect of loading on the two-way shape-memory behavior of cross-linked HDPE (a–b), EOC30 (c–d), and EOC60 (e–f) with the highest crosslink densities of 110, 270, and 190  $\text{mol} \cdot \text{m}^{-3}$ , respectively. The insert in figure (a) enlarges the thermo-mechanical behavior of HDPE loaded by 0.9 MPa.

For deeper understanding and proper characterization of the two-way SME new parameters are introduced, such as the two-way shape-memory effectiveness factor  $\gamma_{eff}$  and the two-way shape-memory recovery factor  $\gamma_{rec}$  as follows:

$$\gamma_{eff} = \frac{\Delta\varepsilon_{inc}}{\varepsilon_{ini}}, \quad (86)$$

$$\gamma_{rec} = \frac{\Delta\varepsilon_{dec}}{\Delta\varepsilon_{inc}} \cdot 100\%. \quad (87)$$

According to the designation (86), the factor  $\gamma_{eff}$  reflects the productivity of pre-drawn covalent polymer network by comparing the anomalous strain increment  $\Delta\varepsilon_{inc}$  originating from the oriented non-isothermal crystallization with the initial entropy-elastic strain of the network  $\varepsilon_{ini}$  arising immediately after loading in the amorphous state. As given by expression (87), the factor  $\gamma_{rec}$  defines the recoverability of the crystallization-induced strain increment during melting of the oriented crystalline phase. In addition, the experimental curves shown in Figure 16 allow estimating the specific work  $W_{sp}$  done by a sample against external force in the course of the two-way shape-memory recovery initiated by melting of crystalline phase at heating under assumption of sample incompressibility:

$$W_{sp} = \frac{F \cdot \Delta l_{dec}}{V} = \sigma_{0N} \cdot \Delta\varepsilon_{dec}, \quad (88)$$

where  $F$  is applied external force,  $V$  is volume of a sample,  $\Delta l_{dec}$  is contraction of a sample at melting.

The temperature dependencies of strain rate illustrated in Figure 16b,d,f disclose the change of kinetics of the two-way SME in PEs under study with the applied load. Based on the presented plots, the switching temperatures of the two-way SME  $T_{sw}^c$  and  $T_{sw}^h$  can be evaluated as the temperatures of strain rate peaks at cooling  $|d\varepsilon/dt|_{max}^c$  and heating  $|d\varepsilon/dt|_{max}^h$ , respectively. Besides, a magnitude of strain rate peak itself is also a relevant characteristic of the two-way shape-memory behavior, as it indicates the maximum rate of shape changing. Finally, these and aforementioned parameters were estimated for all curves in Figure 16 and are listed in Table 3.

As it was previously shown by Kolesov et al. [51], the switching temperature of thermally induced recovery during the one-way SME in cross-linked semicrystalline polymers nearly coincides with their melting point. Moreover, a comparison of data presented in Tables 2 and 3 evidences that crystallization/melting temperatures of the stretched PEs evaluated from DSC (Table 2) and the switching temperatures of the two-way shape-memory behavior (Table 3) are almost the same. This direct correlation of  $T_{sw}^c$  and  $T_{sw}^h$  values with crystallization  $T_c$  and

melting temperature  $T_m$  clearly proves that the anomalous elongation and subsequent contraction in the framework of the two-way SME are caused exactly by crystallization and melting of loaded covalent network of PEs under study, respectively.

**Table 3:** The effect of loading on the parameters of the two-way shape-memory behavior of HDPE, EOC30, and EOC60 with the highest crosslink densities.

Samples	$\nu_c$	$\sigma_{N0}$	$T_{sw}^c$	$T_{sw}^h$	$\epsilon_{ini}$	$\epsilon_{cr}$	$\Delta\epsilon_{inc}$	$\Delta\epsilon_{dec}$	$\gamma_{eff}$	$\gamma_{rec}$	$\left \frac{d\epsilon}{dt}\right _{max}^c$	$\left \frac{d\epsilon}{dt}\right _{max}^h$	$W_{sp}$
	[mol·m <sup>-3</sup> ]	[MPa]	[K]	[K]	[%]	[%]	[%]	[%]	[-]	[%]	[10 <sup>3</sup> ·s <sup>-1</sup> ]	[10 <sup>3</sup> ·s <sup>-1</sup> ]	[kJ·m <sup>-3</sup> ]
HDPE	110	0.9	378.3	398.8	33.7	6.9	–	–	–	–	–	–	–
		1	375 379.4	396	44.6	14.7	42.9	41.6	0.96	97	1.75 1.1	2.12	416
		1.1	383.1	403	59.2	17.9	129.7	87.1	2.19	67	4.34	3.62	958
		1.2	383.5	403.7	76.8	27.9	238.8	151.8	3.11	64	8.85	6.94	1822
EOC30	270	0.45	348	366.6	21.6	5.2	20.6	26.2	0.95	127	1.06	1.24	118
		0.6	346.4	362.5	38.3	11.9	37.3	42.5	0.97	114	1.77	1.73	255
		0.75	349.7	365.2	46.1	18.5	73.1	59.1	1.59	81	3.91	2.22	443
EOC60	190	0.15	309.4	334.3	12.4	2.3	11.8	14.5	0.95	123	0.39	0.4	22
		0.3	310 316.4	333.5	30.8	9.7	34.1	35.2	1.11	103	1.08 0.42	0.86	106
		0.45	311.3 319.3	334.6	58.6	26.2	84.4	61.4	1.44	73	1.96 1.31	1.43	276

The received results allow concluding that both  $T_{sw}^c$  and  $T_{sw}^h$  values of all PEs under study increase in general with increasing load. This fact can be explained by entropy reduction of polymer chains due to uniaxial extension immediately after application of a constant load that results in the initial ordering of network chains already in the amorphous phase [87]. Such ordering contributes to a formation of crystal precursors and, consequently, leads to the crystallization at higher temperature, similarly to quiescent flow-induced crystallization of

entangled polymer melt [110]. As known, the crystalline phase crystallized at higher  $T_c$  melts at higher  $T_m$  as well [85]. However, switching temperatures of HDPE at 0.9 MPa and of EOC30 at 0.45 MPa are higher than that of HDPE at 1 MPa and EOC30 at 0.6 MPa, respectively. Nevertheless, this unusual event can be clarified by taking into account the size of crystallites formed during non-isothermal crystallization. As it was reported by Kitamaru *et al.* [115] for cross-linked HDPE stretched from the melt and crystallized under isometric conditions, the long period  $L$  as a function of draw ratio passes through a minimum, which occurs at low extension, with monotonically increasing draw ratio, while crystallinity rises steadily (Figure 17). Hence, the uniaxial deformation of cross-linked HDPE results primarily in a decrease of the long period, i.e. of the crystal thickness, and only then leads to a rising magnitude of  $L$  as depicted in Figure 17. According to the Gibbs-Thompson equation, thinner crystals melts at lower temperatures [86]. Thereby, it can be assumed that HDPE at 0.9 MPa and EOC30 at 0.45 MPa possess higher switching temperatures because of larger size of crystallites as compared to HDPE at 1 MPa and to EOC30 at 0.6 MPa, correspondingly.

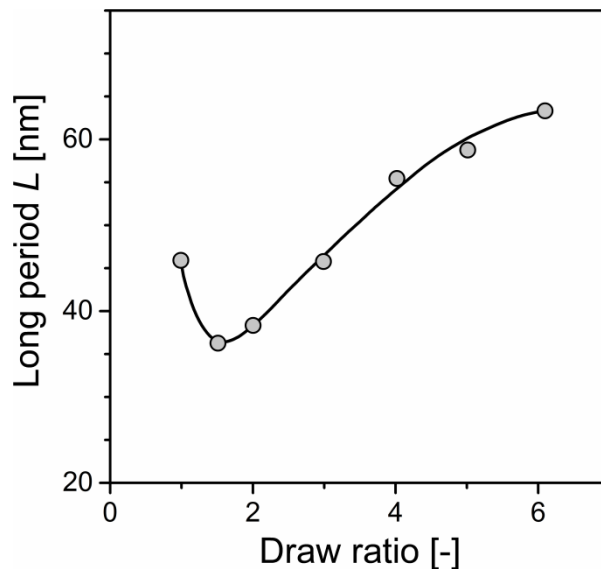


**Figure 17:** Long period  $L$  against the draw ratio measured for the gel sample of linear PE drawn in the molten state at 433 K and crystallized under constant deformation upon cooling to lower temperature below  $T_c$  [115].

Moreover, the fractionated strain rate peaks originated at cooling of HDPE loaded by 1 MPa and EOC60 loaded by 0.3 and 0.45 MPa (Figure 16b,f) evidently reflect the specific

character of crystallization of these samples. It is suggested that the reason for the fractionated strain rate of HDPE lies behind its rather wide molecular weight distribution as shown in Table 1 and the inhomogeneous distribution of crosslink points as mentioned in *Section 5.1*. Thus, relatively low strain induces already a high orientation of short network chains, which crystallize at higher temperature than non-oriented chains on account of the increased number of crystal precursors as discussed above, whereas longer network chains – under the same conditions – become only less oriented towards the stretch direction and therefore they crystallize at lower  $T_c$  than the more oriented short network chains. This effect becomes negligible with increasing load and, consequently, increasing initial deformation  $\varepsilon_{ini}$ , since both short and long network chains become strongly oriented in the stretch direction. By contrast, splitting of strain rate peaks in EOC60 is a consequence of its peculiar crystal structure. As it was earlier investigated, short-chain branched PEs with high degree of side-chains possess the so-called bundle-like or fringed-micelles structure containing both folded- and extended-chain crystals [107,116–117]. Apparently, the primary orientation of network chains due to stretching in the amorphous phase stronger affects exactly the formation of the extended-chain crystallites, in particular, by increasing their crystallization temperature. This influence rises with increasing initial strain  $\varepsilon_{ini}$  as shown in Figure 16f and Table 3.

As visible in Table 3, the values of the two-way shape-memory effectiveness factor  $\gamma_{eff}$  amount to more than 0.9 for all PEs under study and increase markedly with increasing load. This tendency is particularly considerable for HDPE, which exhibits an increase of the efficiency factor  $\gamma_{eff}$  from 0.96 to 3.11. Besides, HDPE at 1.2 MPa demonstrates a remarkably large strain increment  $\Delta\varepsilon_{inc}$  of about 238 %. Such a behavior is an evidence of very high two-way shape-memory productivity of covalent network in HDPE arising from high crystallinity and appropriate crosslink density.

In the meantime, the two-way shape-memory recovery factor  $\gamma_{rec}$  of both linear and branched PEs diminishes with rising stress  $\sigma_{N0}$ . In addition, the recovery rate peak values at cooling  $|d\varepsilon/dt|_{max}^c$  rise faster with increasing load than that at heating  $|d\varepsilon/dt|_{max}^h$  for each polyethylene. Both trends can be explained by taking into account that the anomalous elongation during non-isothermal crystallization proceeds towards the applied force, which accelerates stretching, whereas the sample contraction due to melting of the crystalline phase at heating occurs against the applied stress preventing the strain recovery. Evidently, this effect increases as the applied force rises. Also, the recovery rate peak magnitudes decrease appreciably with the appearance of short-chain branches and with the rise of

degree of branching. So, HDPE possesses the highest  $|d\varepsilon/dt|_{max}^c$  and  $|d\varepsilon/dt|_{max}^h$  values, while EOC60 reveals the lowest strain rates that obviously reflects the inhibition of the nucleation and crystal growth rates in branched PEs as compared to linear HDPE, which is caused by spatial hindrances and results in essentially different crystallinity. This explanation is strongly supported by crystallization and melting behavior of PEs under study depicted in Figure 15 as well as by crystallinity values listed in Table 2.

Note that  $\gamma_{rec}$  magnitudes of short-chain branched PEs at low stresses exceed 100%. The cause of such  $\gamma_{rec}$  values lies in forming only imperfect crystals of lower stability due to annealing at  $T_{low}$ , which contributes to the strain decrement  $\Delta\varepsilon_{dec}$ , so that it exceeds the strain increment  $\Delta\varepsilon_{inc}$ . Melting of this imperfect crystal population is observed in the heating run in Figures 16d,f as additional low and very wide strain rate “peaks” with the switching temperature of about 344–348 K in case of EOC30 and 305–311 K in case of EOC60. Besides, melting of the aforementioned imperfect crystalline phase clearly arise in DSC traces during the first heating of drawn EOC30 and EOC60 as shown in Figure 15a.

The specific work  $W_{sp}$  calculated on the basis of Equation (88) considerably increases with increasing load for HDPE and both branched PEs, in particular, as a result of rising strain decrement  $\Delta\varepsilon_{dec}$ . Also, the HDPE sample loaded by 1.2 MPa performs extremely high mechanical work of approximately  $1.8 \text{ MJ}\cdot\text{m}^{-3}$  that additionally confirms the high two-way shape-memory performance of the covalent network in HDPE as mentioned above. In other words, the specific work  $W_{sp} = 1.8 \text{ MJ}\cdot\text{m}^{-3}$  means that one cubic meter of cross-linked HDPE is able to lift a huge mass of about 122 t to a height of about 1.5 m. Although the EOC60 sample possesses relatively low  $W_{sp}$  values in comparison with HDPE, it reveals the pronounced two-way shape-memory behavior already at 0.15 MPa being initially stretched to only 12.4% and having a sufficiently high effectiveness factor  $\gamma_{eff}$  of 0.95. These facts, at first, point to the small radius of gyration of network chains in EOC60 caused by both high degree of branching and high crosslink density and, secondly, confirm the high perfection of covalent network in EOC60.

### **6.3.2. Effect of crosslink density**

The temperature dependencies of strain and strain rate in Figure 18 demonstrate the change of the two-way shape-memory behavior of EOC30 and EOC60 with increasing crosslink density. The evolution of parameters of the two-way shape-memory performance, which were introduced in *Sections 5.2.* and *6.3.1.*, are listed in Table 4.

The received results allow concluding that both switching temperatures  $T_{sw}^c$  and  $T_{sw}^h$  corresponding to the highest strain rate peaks in Figure 18b and 18d decrease with increasing

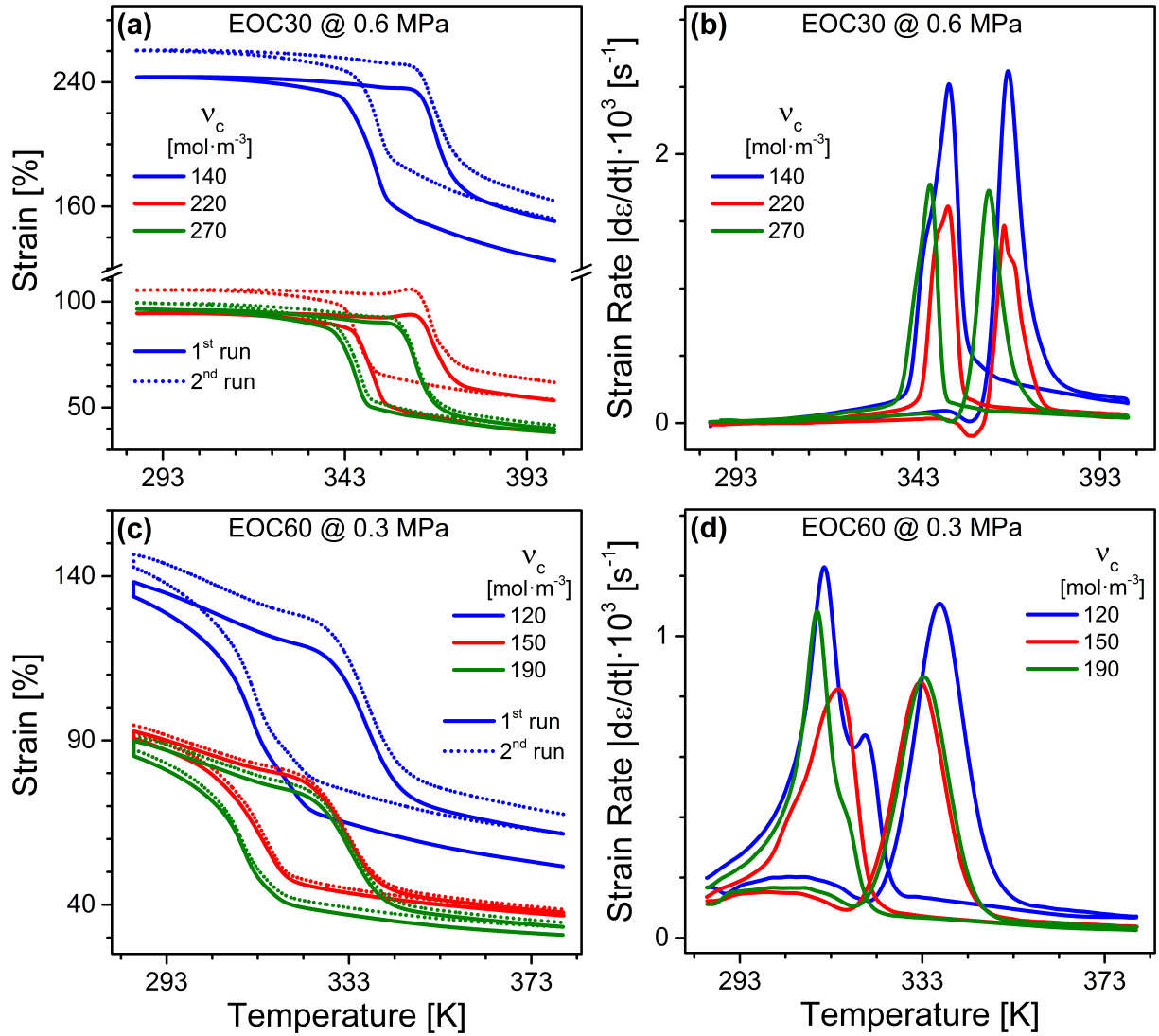


**Figure 18:** The effect of crosslink density on the occurrence (a,c) and kinetics (b,d) of the two-way SME in EOC30 (a–b) and EOC60 (c–d) loaded by 0.6 and 0.3 MPa, respectively.

crosslink density  $\nu_c$ . Such a tendency is similar to the decrease of the crystallization and melting temperatures of undeformed EOC30 and EOC60 with increasing  $\nu_c$  magnitudes, as reported by Kolesov *et al.* [52]. The origin of this phenomenon lies behind shortening the polymer chain between neighboring crosslink points with rising crosslink density that, consequently, results in the reduction of crystallite size and of lamellae thickness. According

to the Gibbs-Thompson equation, thinner crystals melt at lower temperatures [86]. Also, mentioned strong correlation between the dependences of the switching temperatures and crystallization/melting temperatures on  $\nu_c$  additionally proves that exactly crystallization/melting plays a key role in the two-way shape-memory behavior being responsible for its principal manifestation.

**Table 4:** The effect of crosslink density on the parameters of the two-way shape-memory behavior of EOC30 and EOC60 loaded by 0.6 and 0.3 MPa, respectively.

Samples	$\sigma_{N0}$	$\nu_c$	$T_{sw}^c$	$T_{sw}^h$	$\varepsilon_{ini}$	$\varepsilon_{cr}$	$\Delta\varepsilon_{inc}$	$\Delta\varepsilon_{dec}$	$\gamma_{eff}$	$\gamma_{rec}$	$\left \frac{d\varepsilon}{dt}\right _{max}^c$	$\left \frac{d\varepsilon}{dt}\right _{max}^h$	$W_{sp}$
	[MPa]	[mol·m <sup>-3</sup> ]	[K]	[K]	[%]	[%]	[%]	[%]	[-]	[%]	[10 <sup>3</sup> ·s <sup>-1</sup> ]	[10 <sup>3</sup> ·s <sup>-1</sup> ]	[kJ·m <sup>-3</sup> ]
EOC30	0.6	140	345.8 351.5	367.8	124.9	36.6	70.3	67.7	0.56	96	1.45 2.52	2.62	406
		220	348.8 351.2	366.7 369.4	38.4	12.7	36.6	33.9	0.96	93	1.44 1.61	1.47 1.19	203
		270	346.4	362.5	38.3	11.9	37.3	42.5	0.97	114	1.77	1.73	255
EOC60	0.3	120	311.5 320.5	336.9	51.7	17	47.2	44.1	0.91	93	1.23 0.67	1.11	132
		150	314.7	332.7	36.7	10.7	34.9	34.7	0.95	99	0.82	0.85	104
		190	310 316.4	333.5	30.8	9.7	34.1	35.2	1.11	103	1.08 0.42	0.86	106

As can be seen from Table 4, the magnitudes of the initial strain  $\varepsilon_{ini}$  and of the non-isothermal entropy-elastic creep prior to crystallization  $\varepsilon_{cr}$  of short-chain branched PEs under study diminish with rising crosslink density as a result of increasing storage modulus, according to the statistical mechanical theory of rubber elasticity [87], and of perfecting the covalent polymer network, respectively. Although EOC30 with the crosslink density of 140 mol·m<sup>-3</sup> demonstrates a relatively high strain increment  $\Delta\varepsilon_{inc}$  of about 70%, the two-way shape-memory effectiveness factor  $\gamma_{eff}$  of this sample amounts only 0.56. The latter is almost two times lower as compared to other EOC30 samples containing larger number of crosslink



points and about four times lower in comparison with HDPE at 1.1 MPa (Figure 16a and Table 3), which is stretched after crystallization nearly to the same strain of approximately 210% as well as has comparable crosslink density but higher crystallinity. Besides,  $\gamma_{eff}$  values for all samples of short-chain branched PEs increase with increasing crosslink density  $\nu_c$ . These facts allow establishing very important empirically justified conclusions:

- the two-way shape-memory performance of covalent polymer networks strongly depends on the crosslink density  $\nu_c$  and rises with elevating  $\nu_c$  values;
- crystallinity plays a crucial role in the two-way shape-memory performance as it mainly determines the capacity of covalent network to reveal the two-way SME.

Note that the two-way shape-memory recovery factor  $\gamma_{rec}$  of EOC30 and EOC60 with various  $\nu_c$  magnitudes is above 90% that is an evidence of the good perfection of covalent networks in these samples. In the meantime, the EOC30 sample with the crosslink density of  $220 \text{ mol}\cdot\text{m}^{-3}$  exhibits lower  $\Delta\varepsilon_{dec}$ ,  $\gamma_{rec}$ , and  $W_{sp}$  values as compared to EOC30 having  $270 \text{ mol}\cdot\text{m}^{-3}$  in spite of the fact that both samples were initially stretched almost to the same extent. Thus, it can be concluded that the two-way shape-memory recovery factor  $\gamma_{rec}$  is a significant and properly introduced parameter, since  $\gamma_{rec}$  magnitude strongly correlates with the perfection of covalent polymer network. Additionally, the change of the specific work  $W_{sp}$  with increasing crosslink density only reflects the change of the strain decrement  $\Delta\varepsilon_{dec}$ . However, the comparison of  $W_{sp}$  values listed in Tables 3 and 4 discloses that exactly the crystallinity characterizes the ability of cross-linked semicrystalline polymers to do useful work in the course of the two-way SME.

#### **6.4. Crystal morphology of cross-linked polyethylenes**

The TEM images of cross-linked HDPE, EOC30, and EOC60 samples prepared both during slow non-quiescent crystallization and during non-isothermal crystallization under load in the course of shape-memory creep are depicted in Figure 19. As shown in Figure 19a–d, the crystalline phase of cross-linked HDPE and EOC30 is represented by lamellae, which are well distinct in HDPE and thin, short, and substantially distorted in EOC30. More particularly, these lamellae are randomly oriented in undeformed samples (Figure 19a,c) and oriented nearly perpendicular to the loading force direction in stretched specimens having residual strain of about 100% (Figure 19b,d). The received TEM images allow estimating the lamellae thickness that amounts roughly 12 nm for both undeformed and drawn cross-linked HDPE.

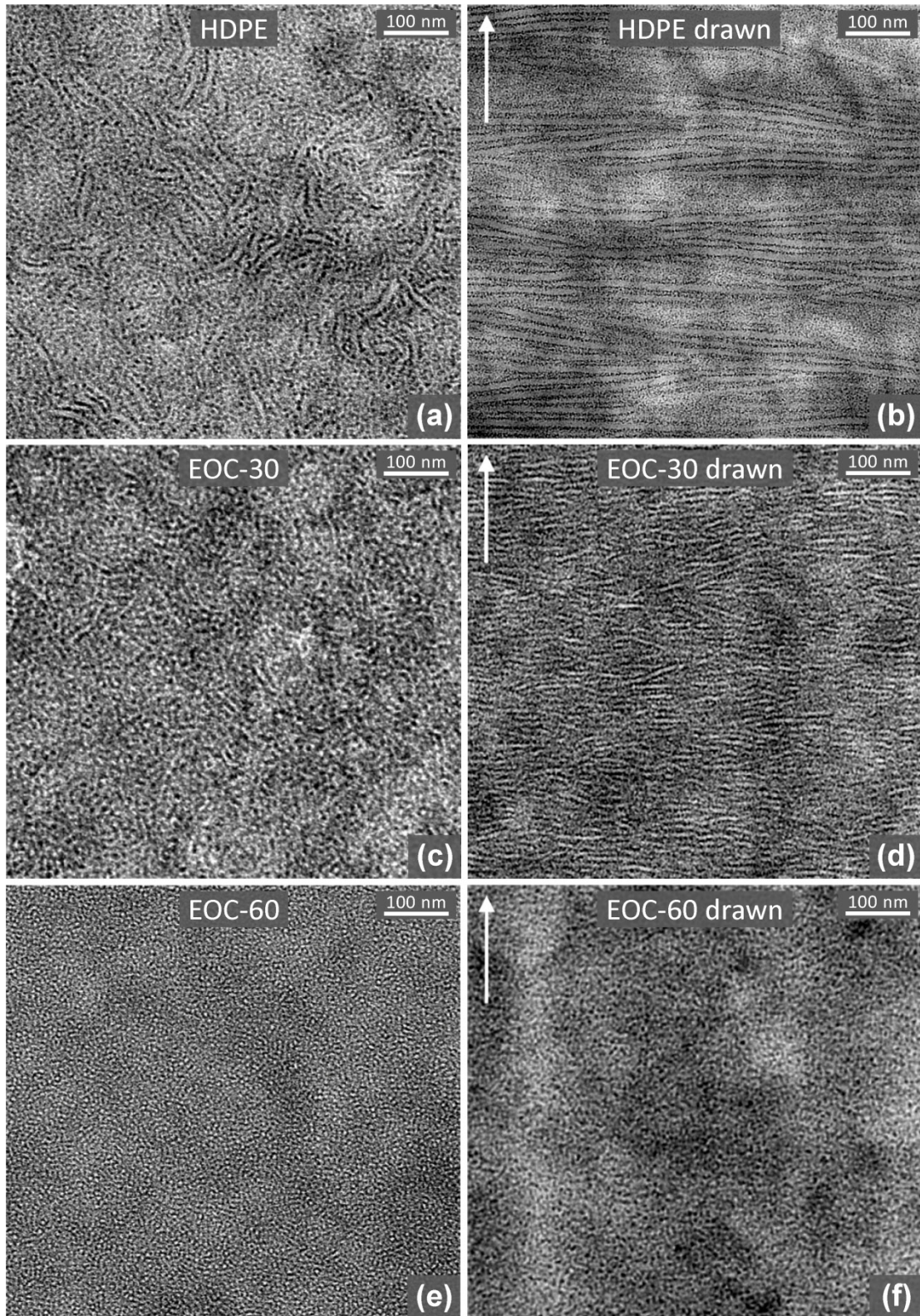


**Figure 19:** High-resolution TEM images of undeformed cross-linked HDPE with  $v_c = 110 \text{ mol}\cdot\text{m}^{-3}$  (a), EOC30 with  $v_c = 270 \text{ mol}\cdot\text{m}^{-3}$  (c), and EOC60 with  $v_c = 190 \text{ mol}\cdot\text{m}^{-3}$  (e) and of their samples stretched during non-isothermal crystallization under load of 1MPa (b), 0.6 MPa (d), and 0.3 MPa (f). White arrows in images (b,d,f) indicate the stretch direction.

In the meantime, drawn and undeformed samples of cross-linked EOC60 (Figure 19e–f) contain small crystallites, whose size and orientation cannot be evaluated on the basis of obtained TEM images. In this connection, it should be noted that super-molecular structure/morphology of *uncross-linked* and undeformed short-chain branched PEs has been investigated earlier as a function of degree of branching by means of TEM and atomic force microscopy [107,113,116–117]. The results of these investigations revealed that in case of linear, slightly branched, and partly medium-branched PEs, especially if samples were slowly crystallized or well annealed, well organized and laterally extended lamellae (folded-chain crystals) can be seen clearly with a tendency to formation of lamellae stacks. With increasing degree of branching and crystallization rate the described super-molecular lamellar structure is more and more replaced with smaller, imperfect, and randomly oriented lamellae as well as with so-called bundle-like crystals or fringed-micelles structure containing extended-chain crystals [107,116–117]. In the light of these results, it can be assumed that the changes of crystal morphology with increasing degree of branching in cross-linked PEs reveal the trend similar to that was demonstrated for *uncross-linked* PEs, i.e., the substitution of folded-chain crystals by extended-chain crystals with increasing degree of branching (e.g. in cross-linked EOC60). Besides, the molecular orientation of crosslink points during crystallization of loaded networks causes the additional constraints of nucleation and crystal growth in cross-linked PEs and strongly affects the crystal morphology as revealed in Figure 19.

## **6.5. Crystal orientation**

### **6.5.1. WAXS of cross-linked polyethylenes**

WAXS patterns in Figure 20 were recorded to determine the orientation of the crystals in both slowly crystallized undeformed and stretched PEs with the highest crosslink densities crystallized under load during the two-way shape-memory experiment as illustrated in Figure 14 and 16. Though the stresses applied to HDPE, EOC30, and EOC60 were different, the samples were finally stretched nearly to the same strain resulting in about 90–100%. Furthermore, in order to find the evolution of the crystal orientation, WAXS images shown in Figure 21 were collected for stretched HDPE samples crystallized under different loads as discussed in *Section 6.3.1*.

As can be seen in Figure 20a–c, WAXS reflections of undeformed specimens are represented by continuous concentric circles, which indicate the random orientation of crystals. On the other hand, the arcs of reflections of stretched PEs in Figures 20d–f and 21 point to preferred orientation of crystals. Namely, both reflections 110 and 200 in stretched



EOC60 are situated on the equator, perpendicular to the draw direction (Figure 20f). Therefore, the  $a$  and  $b$  axes of the orthorhombic unit cell [102,111] are orthogonal to the stretch direction or, in other words, crystals are oriented such that the chain axis  $c$  is parallel to the draw direction. Thus, no further calculation is needed to ascertain the orientation of the unit cell of stretched EOC60. On the contrary, the determination of crystal orientation in drawn HDPE and EOC30 requires additional treatment.

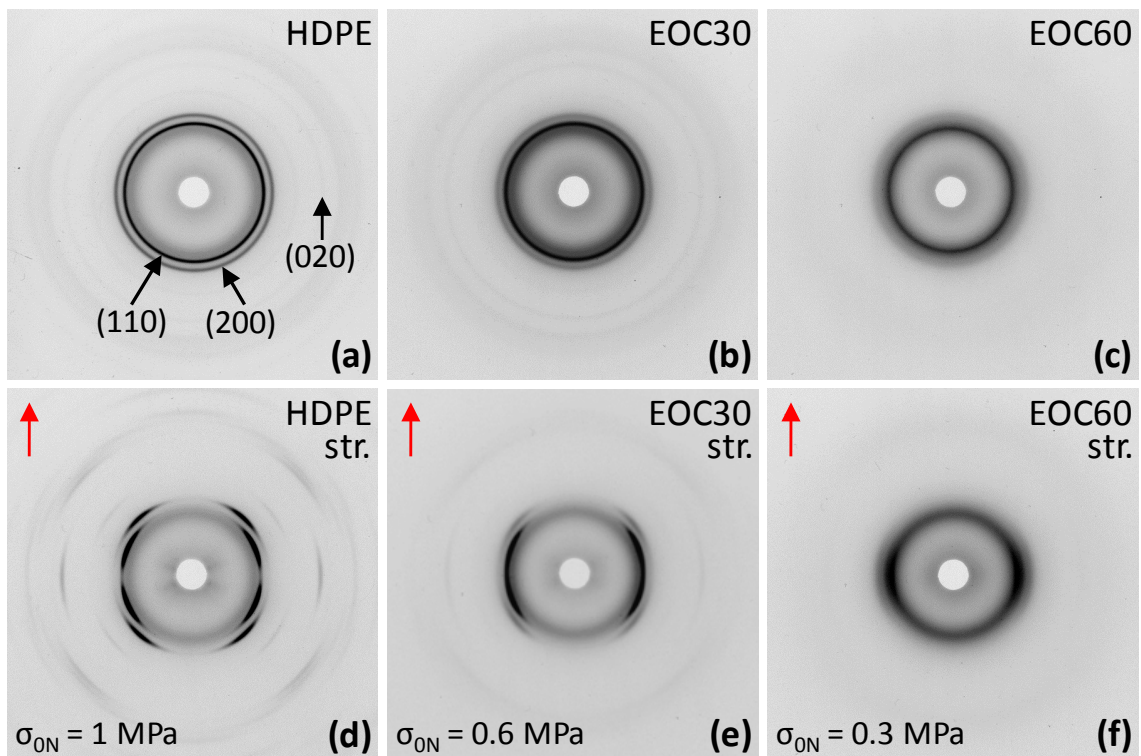


**Figure 20:** WAXS patterns of undeformed slowly crystallized (a–c) and stretched due to crystallization under load (d–f) foils of HDPE, EOC30, and EOC60 with the highest crosslink densities of 110, 270, and 190 mol·m<sup>-3</sup>, respectively. Red arrows in figures (d–f) indicate the stretch direction.

The equatorial scattering plots in Figure 22 were obtained by sector integration over  $\pm 5^\circ$  related to the orientation on equator of the WAXS images of stretched PEs presented in Figures 20d–f and 21. The peak positions of the reflections from the (110), (200), and (020) crystallographic planes, in case they were resolved, were used to calculate the parameters  $a$  and  $b$  of the unit cell on the basis of Bragg's law [118]:

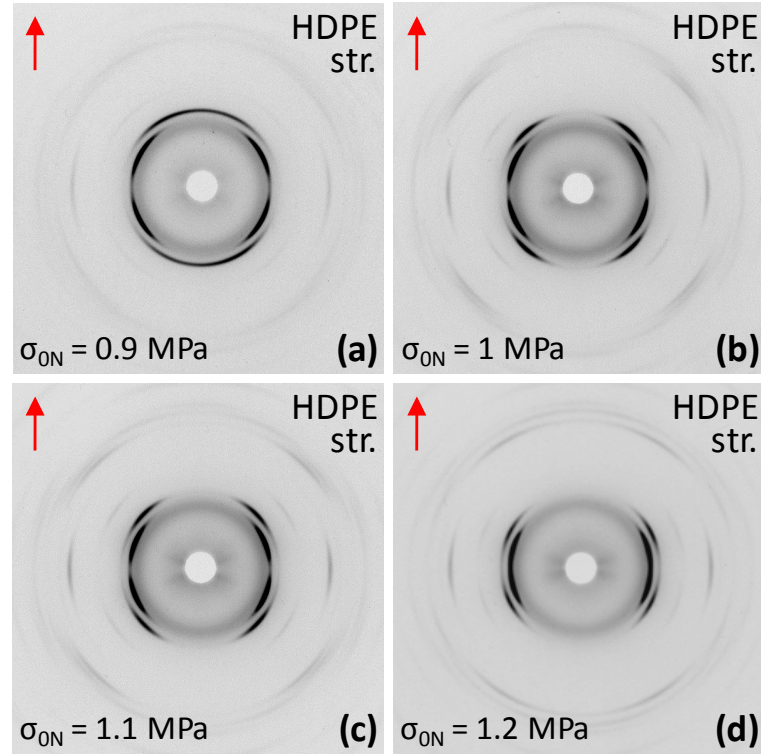


**Figure 21:** WAXS patterns of HDPE foils with the crosslink density of  $110 \text{ mol}\cdot\text{m}^{-3}$  stretched due to crystallization under load of 0.9 (a), 1 (b), 1.1 (c), and 1.2 MPa (d). Red arrows in figures indicate the stretching direction.

$$2d(hkl) \cdot \sin\theta = n\lambda_0, \quad (89)$$

where  $d(hkl)$  is the interplanar spacing between neighboring  $(hkl)$ -planes,  $\theta$  is the Bragg angle, i.e., one-half the angle of deviation of the diffracted rays from the incident X-rays,  $n$  is an integer, and  $\lambda_0$  is the wavelength of X-rays. Only the first order of reflections was recorded in the WAXS images, therefore  $n = 1$ .

To determine the positions of peaks precisely, the experimental findings in the 1D plots were approximated by the Gaussian functions corresponding to the amorphous halo peak and scattering peaks as shown in Figure 22. Since the crystal symmetry of HDPE and EOC30 is orthorhombic [102], the following equations are used to calculate the orientation of the unit cell [118]:

$$\cos^2\varphi_{hk0,Z} = e_a^2 \cdot \cos^2\varphi_{h00,Z} + e_b^2 \cdot \cos^2\varphi_{0k0,Z}, \quad (90a)$$

$$\cos^2\varphi_{h00,Z} + \cos^2\varphi_{0k0,Z} + \cos^2\varphi_{00l,Z} = 1, \quad (90b)$$

where  $\varphi_{hk0,Z}$  is the angle between the unit vector normal to the  $(hk0)$ -plane and the stretch direction or machine direction  $Z$ ;  $\varphi_{h00,Z}$  is the angle between the unit vector normal to the  $(h00)$ -plane, i.e.,  $a$ -axis, and the stretch direction  $Z$ ;  $e_a$  is the cosine of the angle between the unit vector normal to the  $(hk0)$ -plane and  $a$ -axis;  $e_b$  is the cosine of the angle between the unit vector normal to the  $(hk0)$ -plane and  $b$ -axis.

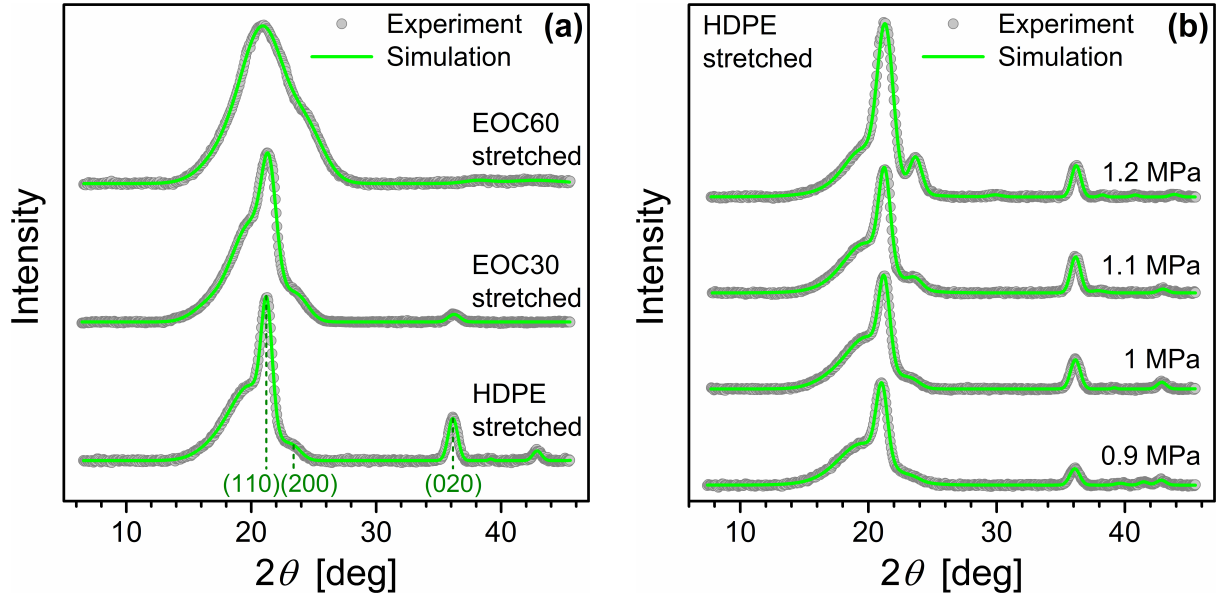


**Figure 22:** Equatorial scattering curves of stretched HDPE, EOC30, and EOC60 crystallized under load during the two-way SME (a) as well as stretched HDPE samples crystallized under different loads (b). The experimental curves (gray points) in (a) and (b) were obtained by sector integration over  $\pm 5^\circ$  related to the orientation on equator of the WAXS images shown in Figures 20d–f and 21, respectively. Green lines represent the simulation curves.

Finally, the orientation of the unit cell relative to the stretch direction  $Z$  in drawn HDPE and EOC30 is calculated by consecutive substitution of the angles values  $\varphi_{110,Z}$  and  $\varphi_{200,Z}$  determined from corresponding WAXS images into the left part of Equation (90a) and by the solution of the obtained systems of equations (90). Note that reflections in Figures 20d–e and 21 are represented by the relatively wide arcs that has to be accounted for calculations. So, Table 5 lists the parameters  $a$  and  $b$  of the unit cell as well as its orientation for all stretched PEs under study. As the angles  $\varphi_{200,Z}$  and  $\varphi_{a,Z}$  are the same, only values  $\varphi_{a,Z}$  are shown in Table 5.

The received results show that though the crystals of HDPE drawn under 0.9, 1, and 1.1 MPa are oriented, they make a sufficiently large angle with the stretch direction and exhibit a wide distribution of orientation. Furthermore, the unit cell of EOC30 drawn under 0.6 MPa possesses stronger orientation with a narrower distribution as compared to the HDPE sample stretched nearly to the same strain under 1 MPa. This fact can be explained as the result of a higher crosslink density of EOC30, i.e., shorter polymer chains between neighboring crosslink points that causes, consequently, a stronger orientation of the drawn network chains already in the amorphous state before crystallization proceeds.

**Table 5:** Structural parameters  $a$  and  $b$  of the unit cell as well as its orientation relative to the stretch direction  $Z$  as determined for the stretched samples of HDPE, EOC30, and EOC60 crystallized under load during the two-way SME.

Samples	$\nu_c$ [mol·m <sup>-3</sup> ]	$\sigma_{0N}$ [MPa]	$a$ [nm]	$b$ [nm]	$\varphi_{110,Z}$ [°]	$\varphi_{a,Z}$ [°]	$\varphi_{b,Z}$ [°]	$\varphi_{c,Z}$ [°]
HDPE	110	0.9	0.75	0.497	61±14	23±12	88±6	67±11
		1	0.749	0.496	67±14	42±8	87±4	46±9
		1.1	0.749	0.496	69±12	47±5	88±4	43±8
		1.2	0.75	0.496	75±12	64±4	88±3	26±7
EOC30	270	0.6	0.745	0.496	71±12	55±7	88±3	35±8
EOC60	190	0.3	0.744	0.495	90±9	90±8	90±8	0±8

In addition, it was found that the orientation of the  $c$ -axis of stretched HDPE changes *quasi-discretely* depending on the uniform increase of applied constant stress as it evidently follows from Table 5. Such unique behavior will be discussed in details on the basis of the results of modeling presented in the next *Section 6.6*.

### 6.5.2. SAXS of cross-linked polyethylenes

SAXS images of slowly crystallized undeformed and stretched samples of HDPE, EOC30, and EOC60 crystallized under load during the two-way SME are presented in Figure 23. The continuous reflections in Figure 23a–c indicate that alternating crystalline and amorphous

regions are randomly oriented. However, the long period (repeating unit) of this layered structure  $L$  can be determined as:

$$L = L_c + L_a, \quad (91)$$

where  $L_c$  is thickness of crystalline sublayer and  $L_a$  is thickness of amorphous sublayer.

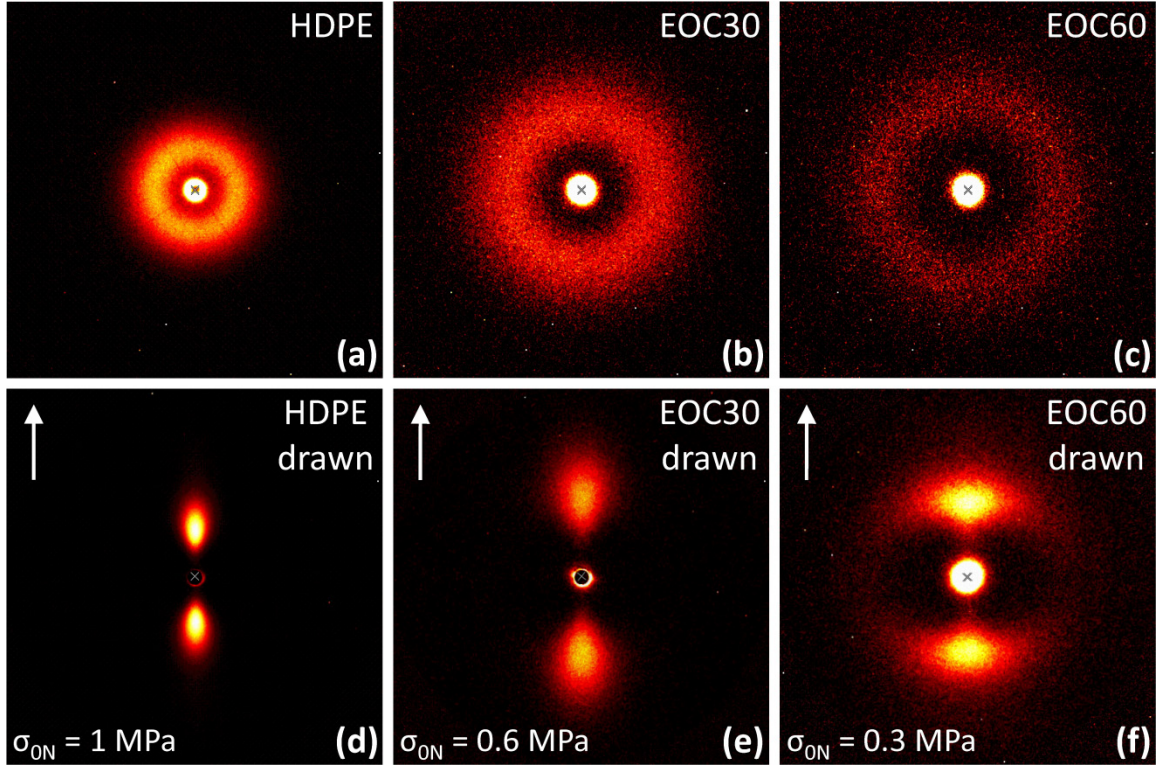


**Figure 23:** SAXS images of undeformed (a–c) and drawn crystallized under load during cooling stage of the two-way shape-memory cycle (d–f) samples of HDPE ( $v_c = 110 \text{ mol}\cdot\text{m}^{-3}$ ), EOC30 ( $v_c = 270 \text{ mol}\cdot\text{m}^{-3}$ ), and EOC60 ( $v_c = 190 \text{ mol}\cdot\text{m}^{-3}$ ). White arrows in figures (d–f) indicate the stretch direction.

On the contrary, the 2D images of drawn PEs under study in Figure 23d–f are an evidence that periodic crystalline structure is ordered such that a normal to the alternating crystalline and amorphous sublayers lies in the stretch direction. Note that Figure 23c has an only low contrast due to the low crystallinity of EOC60.

The plots of SAXS intensity  $I \cdot q^2$  as a function of scattering vector  $q = 2\pi/d$ , where  $d$  is the interplanar spacing, received by  $360^\circ$ -integration and curves of intensity  $I$  vs. azimuthal



angle  $\chi$  obtained at the maximum of the  $I \cdot q^2$ -curves by integration over a small  $\Delta q$  interval are shown in Figure 24.

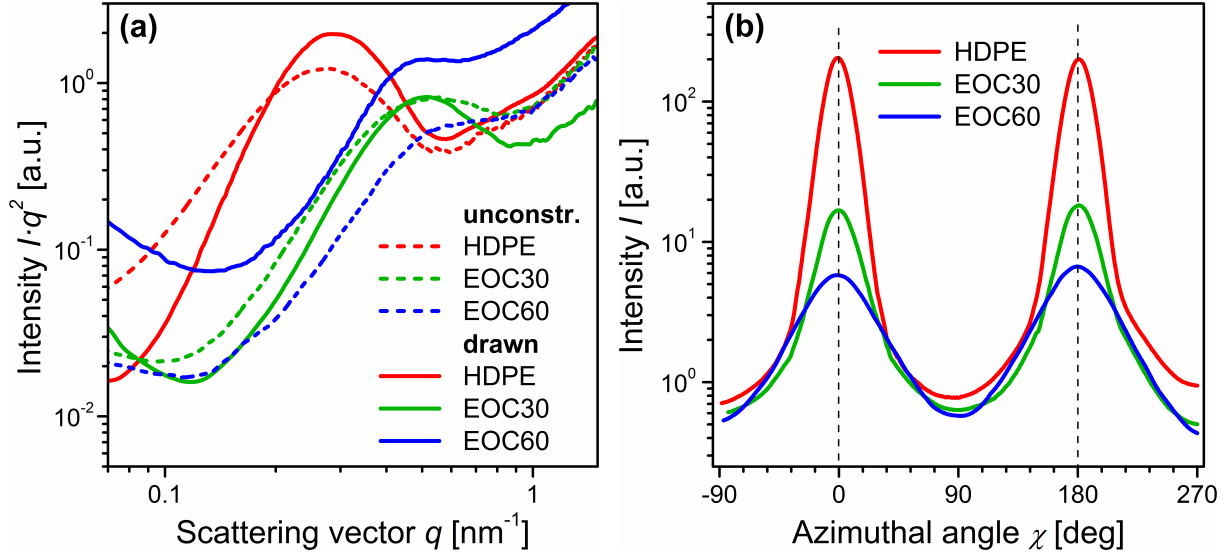


**Figure 24:** SAXS intensity  $I \cdot q^2$  vs. scattering vector  $q$  (a) obtained by  $360^\circ$ -integration of the SAXS images of crystallized unconstrained and crystallized under load samples of HDPE ( $v_c = 110 \text{ mol}\cdot\text{m}^{-3}$ ), EOC30 ( $v_c = 270 \text{ mol}\cdot\text{m}^{-3}$ ), and EOC60 ( $v_c = 190 \text{ mol}\cdot\text{m}^{-3}$ ) presented in Figure 23d–f as well as intensity  $I$  vs. azimuthal angle  $\chi$  (b) of the same drawn PEs.

Assuming that all crystalline and amorphous regions are arranged as sublayers in lamellar stacks, the crystals thickness  $L_c$  for all samples of PEs can be calculated by multiplying the long period  $L$  determined as the peak position of curves in Figure 24a by the corresponding crystallinity values obtained on the basis of DSC (Section 6.2.) and listed in Table 2.

The calculated values of crystal thickness  $L_c$ , the values of full width at half maximum (FWHM) of scattering curves presented in Figure 24b, and relative orientation degree  $\Theta_{\text{rel}} = (180^\circ - \text{FWHM})/180^\circ$  are listed in Table 6. Note that the values of calculated crystal thickness of PEs are in satisfactory agreement with the rough estimations obtained on the basis of TEM images presented in Figure 19. In addition, crystals in the stretched EOC30 and EOC60 samples are slightly thicker as compared to the undeformed samples that is logical consequence of stretching.

Based on the results of the orientation of the unit cell obtained from the WAXS images of drawn HDPE and EOC30 as well as on the data of the orientation of crystals determined from

**Table 6:** Crystal thickness of the undeformed and stretched samples of HDPE ( $v_c = 110 \text{ mol}\cdot\text{m}^{-3}$ ), EOC30 ( $v_c = 270 \text{ mol}\cdot\text{m}^{-3}$ ), and EOC60 ( $v_c = 190 \text{ mol}\cdot\text{m}^{-3}$ ) as determined by SAXS as well as the orientation of periodic crystalline structure of drawn PEs crystallized under load during cooling stage of the two-way shape-memory cycle.

Samples	Long period	Crystallinity	Crystal	FWHM	$\Theta_{\text{rel}}$	
	$L$	$\chi_c$ at 298 K (DSC)	thickness $L_c$			
	[nm]	[%]	[nm]	[°]	[-]	
HDPE	undeformed	23.2	50.4	11.7	–	–
	drawn	21.7	54.3	11.8	18.6	0.9
EOC30	undeformed	11.7	29.6	3.5	–	–
	drawn	12.6	30.8	3.9	25.6	0.86
EOC60	undeformed	11.3	12.4	1.4	–	–
	drawn	13.6	13.7	1.9	43.9	0.76

SAXS and TEM of these samples, it can be concluded that alternating crystalline and amorphous regions are arranged perpendicularly to the stretch direction  $Z$ . The basal surfaces of lamellae are orthogonal to  $Z$ , however, the crystalline structure of HDPE and EOC30 inside the lamellae owns a tilted arrangement so that the chain axis  $c$  makes an acute angle with  $Z$ . According to the WAXS results, the axis  $b$  of the unit cell is perpendicular to the stretch direction  $Z$ , whereas axes  $a$  and  $c$  make acute angles with  $Z$  and lie in one plane with  $Z$ . The sketch presented in Figure 25 shows one possible arrangement of lamellae stacks, axes of the unit cell, and the stretch direction  $Z$  relative to the X-ray beam line. In the entire sample volume rotated versions of lamellae stacks around  $Z$  should be taken into account as well. Thereby, the angles between axes of the unit cell and the stretch direction remain the same. The rotating arrow in Figure 25 exemplifies this circumstance.

Note that the axis of folded chains, i.e.  $c$ -axis of the unit cell, has been frequently sketched perpendicular to the basal surfaces of lamellae [85–86]. However, the folded chains tilted to the basal surfaces of the lamellae can be observed in oriented samples of HDPE and polyamide 6 after plastic shearing (slip) of crystallites under uniaxial compression at room temperature, as it was described in the review of Bowden and Young [119]. Though the

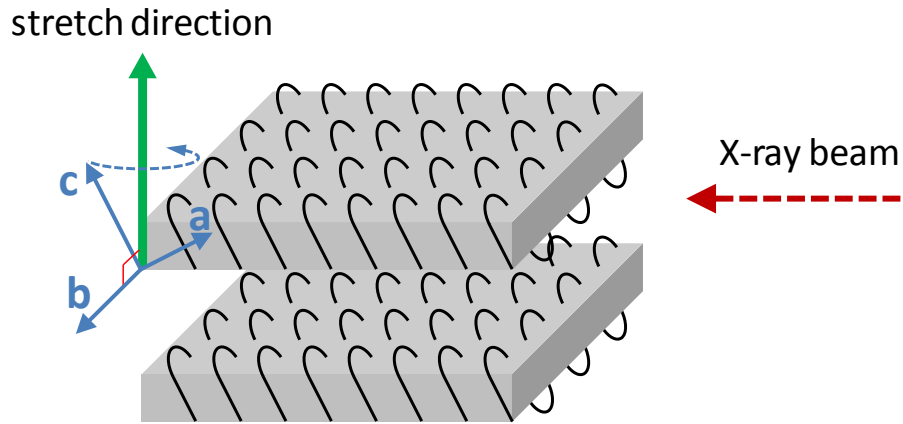


**Figure 25:** A sketch illustrating the orientation of lamellae and of the unit cell determined on the basis of WAXS and SAXS investigation in the stretched samples of HDPE and EOC30 crystallized under load during cooling stage of the two-way shape-memory cycle.

peculiar crystal structure investigated in the present work is similar to that reported by Bowden and Young, it was formed under quite different conditions, namely, under constant uniaxial load (extension) during non-isothermal crystallization at cooling. Thus, the mechanism of formation of such crystals is different than in the case described by Bowden and Young. Nevertheless, the reason for the generation of the crystalline structure shown in Figure 25 apparently lies behind the existence of a covalent polymer network. The possible molecular mechanism responsible for the formation of the aforementioned tilted crystal structure is as follows. So, the application of a constant force to the spatial covalent network inevitably results in both the uniaxial extension along the force direction and the compression in other two dimensions orthogonal to the force vector [87]. Obviously, the compression of the cross-sectional area is caused by the appearance of the stress components normal to the force direction. As soon as a real imperfect covalent network is considered, it can be assumed that the normal stress components acting on a microscopic level may become shearing ones. These microscopic shear stresses cause the tilt of network chains whereby after crystallization the folded chains become inclined to the basal surfaces of lamellae. Although the presented explanation needs a reliable experimental confirmation, it is quite convincing with the results obtained by Bowden and Young [119], since shear stress is assumed to be responsible for the tilt of folded chains inside lamellae in both cases.

## 6.6. Modeling the two-way shape-memory behavior

### 6.6.1. Linear high-density and branched polyethylenes

The theoretical description presented in *Section 4.2.2.* is used to model the crystal morphology and the orientation of crystals formed in covalent networks of HDPE and EOCs

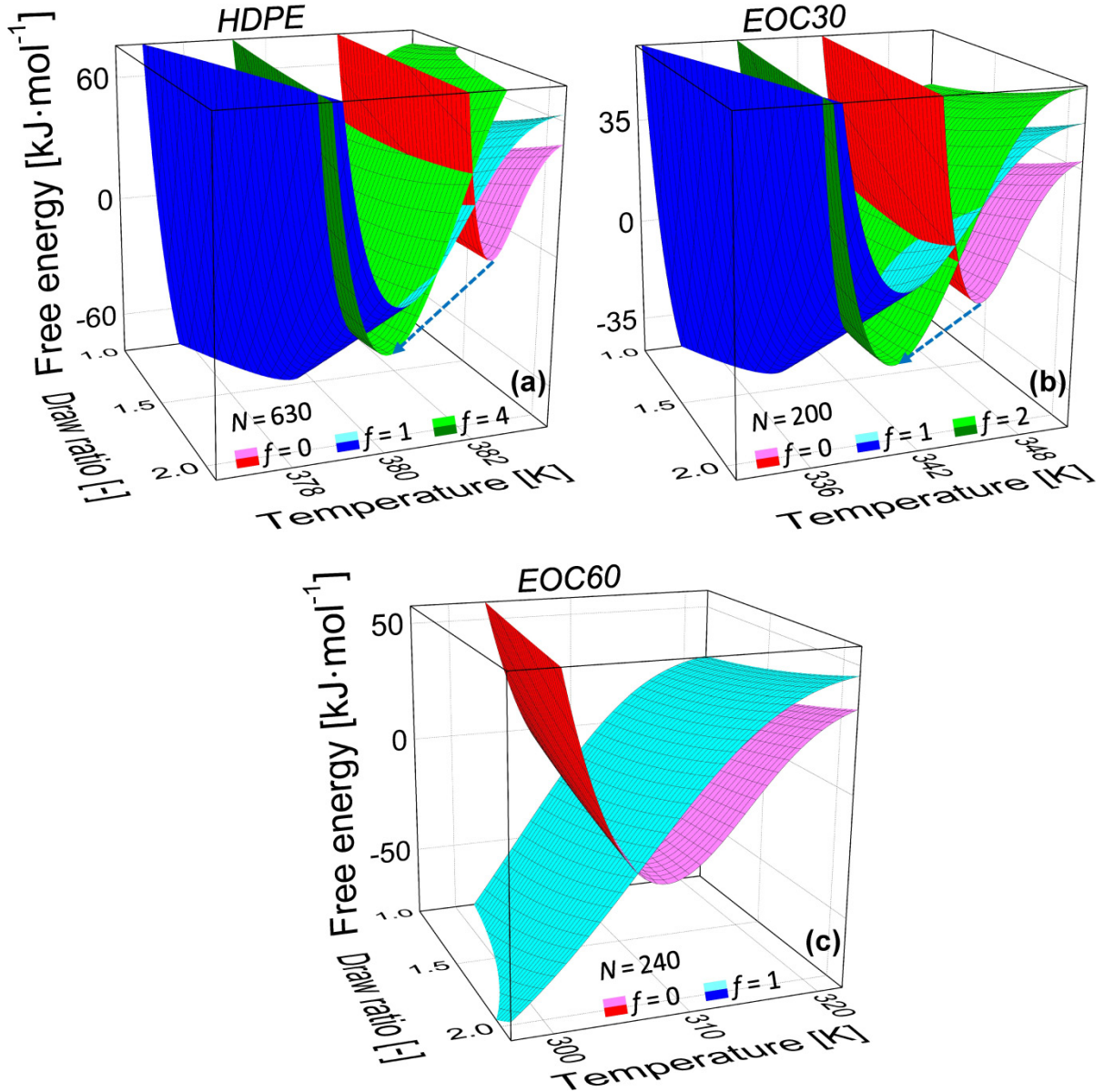


**Figure 26:** The free energies of crystallization  $\Delta F_f(T, \lambda)$  as a function of temperature and draw ratio calculated for HDPE with  $v_c = 110 \text{ mol}\cdot\text{m}^{-3}$  (a), EOC30 with  $v_c = 270 \text{ mol}\cdot\text{m}^{-3}$  (b), and EOC60 with  $v_c = 190 \text{ mol}\cdot\text{m}^{-3}$  (c) in case of different numbers of crystal folds  $f$ . Blue dashed arrows in figures (a) and (b) indicate the crystallization path at cooling.

during non-isothermal crystallization under constant load, i.e. in the course of cooling stage of the two-way SME. Thus, Equation (65) was taken to calculate the free energy of crystallization  $\Delta F_f(T, \lambda)$  as a function of temperature and draw ratio for cross-linked HDPE, EOC30, and EOC60 in case of different number of folds  $f$  using the following appropriate values for the parameters in Equation (65):

$$U_{em} = 13791.3 \text{ J}\cdot\text{mol}^{-1}, U_e = 13238.7 \text{ J}\cdot\text{mol}^{-1}, b_0 = 0.154 \text{ nm}, a_0 = 0.425 \text{ nm}, \\ \psi = 4, T_m^0 = 419 \text{ K}, \Delta H_\mu = 4140 \text{ J}\cdot\text{mol}^{-1}.$$

Results are presented in Figure 26. Numbers of chain links  $N$  were chosen so that they nearly correspond to the highest crosslink densities of PEs under study, namely,  $N = 630$  for HDPE ( $v_c = 110 \text{ mol}\cdot\text{m}^{-3}$ ),  $N = 200$  for EOC30 ( $v_c = 270 \text{ mol}\cdot\text{m}^{-3}$ ), and  $N = 240$  for EOC60 ( $v_c = 190 \text{ mol}\cdot\text{m}^{-3}$ ).  $\Delta F_f(T, \lambda)$  values corresponding to numbers of folds  $f = 2, 3$  and  $f > 4$  for HDPE,  $f > 2$  for EOC30 as well as  $f > 1$  for EOC60 are greater and so they are not shown in Figure 26.

The results indicate that the lowest free energy for EOC60 (Figure 26c) corresponds to the extended-chain morphology ( $f = 0$ ) oriented parallel to the direction of draw. Though the free energy of crystals with  $f = 1$  in case of EOC60 has lower values when  $T < 310 \text{ K}$ , it does not reach a minimum over the whole temperature range and reflects a nonequilibrium thermodynamic process that does not satisfy the initial assumptions, on which the developed theory is based (*Section 4.2.2.*), and therefore is not realized and will not be taken into further consideration. In the meantime, in case of HDPE and EOC30 (Figure 26a–b) the extended-chain morphology ( $f = 0$ ) has a lower free energy at the onset of crystallization, whereas further cooling results in formation of the folded-chain crystals ( $f = 2$  and  $4$ ) with the chain axis oriented in the stretch direction but not parallel.

Note that the correctness of number of fold links  $\psi = 4$  in case of polyethylene was confirmed by Keller [120] and Frank *et al.* [121]. In addition, Hoffman [122] has shown that crystals with regular chain folding possess the lower surface free energy in comparison with crystals with switchboard chain folding or bundle-like crystals. Furthermore, Hoffman established theoretically that the lower surface free energy results in the faster crystal growth. Thus, fast crystallization or, in other words, high crystallization kinetics is accompanied by regular chain folding [122]. As shown in Figure 15b in *Section 6.2.*, crystallization peaks of both undeformed and stretched HDPE are very narrow that explicitly reflects high crystallization kinetics and, correspondingly, points to regular folding. In addition, all shape-

memory experiments were carried out with cooling/heating rate of  $2 \text{ K}\cdot\text{min}^{-1}$  (Section 5.2.) that ensures observing quasi-equilibrium crystallization of PEs as also assumed during the theoretical consideration in Section 4.2.2. Besides, the assumption  $\psi = 4$  was employed for HDPE and EOC30. In the meantime, highly-branched EOC60 has crystals with the lowest free energy of crystallization corresponding to the extended-chain morphology ( $f = 0$ ).

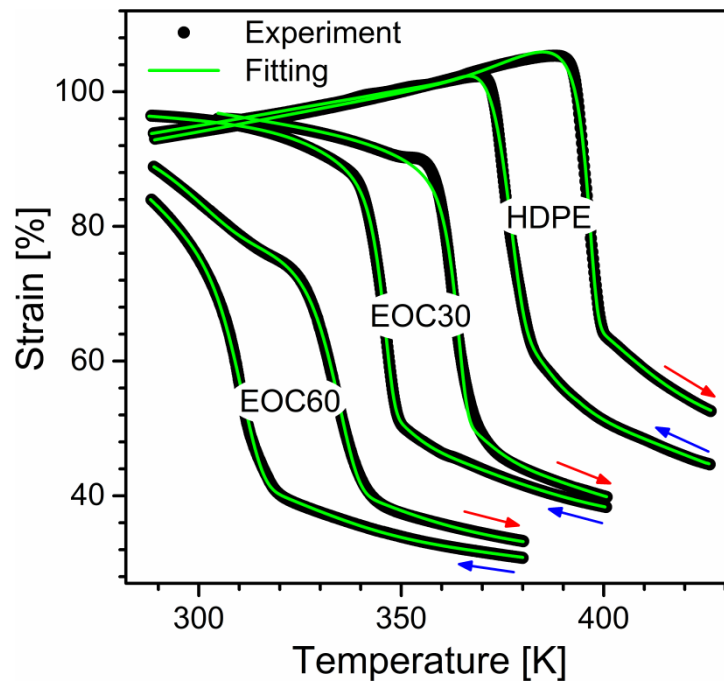


**Figure 27:** Experimental and fitting curves of the two-way SME obtained for cross-linked HDPE ( $v_c = 110 \text{ mol}\cdot\text{m}^{-3}$ ), EOC30 ( $v_c = 270 \text{ mol}\cdot\text{m}^{-3}$ ), and EOC60 ( $v_c = 190 \text{ mol}\cdot\text{m}^{-3}$ ) loaded by  $\sigma_{0N} = 1 \text{ MPa}$ ,  $\sigma_{0N} = 0.6 \text{ MPa}$ , and  $\sigma_{0N} = 0.3 \text{ MPa}$ , respectively. Blue and red arrows indicate cooling and heating runs, correspondingly.

Modeling the two-way SME as well as determination of material parameters were carried out using the experimental findings of HDPE, EOC30, and EOC60 obtained and corrected as clearly presented in Section 6.3.1. and Section 5.2., correspondingly. Based on equations (75) and (84) as well as on their respective detailed description, the temperature dependent strain was fitted by means of the Levenberg-Marquardt algorithm. The results are depicted in Figure 27. As can be seen in Figure 27, fitting curves computed on the basis of the theoretical description of the two-way SME derived in Chapter 4 demonstrates very good coincidence

with the experimental data. The values of relevant fitting and material parameters of PEs under study are listed in Table 7. The crystal thickness  $L_c$  was calculated in terms of obtained fitting parameters as follows:

$$L_c = \zeta \cdot b_0 = \frac{N \cdot \chi_{cf}}{(f+1)} b_0, \quad (92a)$$

$$L_c = \frac{1000}{\text{number of branches per } 1000C} b_0. \quad (92b)$$

**Table 7:** Relevant fitting and material parameters as well as calculated on their basis crystal thickness  $L_c$  for HDPE, EOC30, and EOC60.

Samples	$\varepsilon_{01}$ [%]	$\nu_e$ [mol· m <sup>-3</sup> ]	$V_h$ [nm <sup>3</sup> ]	$V_m$ [10 <sup>3</sup> · nm <sup>3</sup> ]	$U$ [kJ· mol <sup>-1</sup> ]	$N$ [-]	$\nu_c$ [mol· m <sup>-3</sup> ]	$f$ [-]	$\chi_{cf}$ [%]	$T_{sw}^c$ [K]	$T_{sw}^h$ [K]	$L_c$ [nm]
HDPE	5.2	89.5	2.1	4.2	105.7	630	110	4	57.4	375.8	396.6	11.1
EOC30	5.1	123.9	4.3	38.4	95.8	200	270	2	34.7	342.9	362.6	3.6
EOC60	4.9	144.4	4.5	68.3	77.8	240	190	0	18.5	310.1	333.5	2.6

Note that Equation (92a) can be reliably used only for linear and slightly branched polymers like HDPE and EOC30. The value  $L_c$  estimated for highly-branched EOC60 by Equation (92a) exceeds the chain length between two neighboring branches. Since it is assumed that short-chain branches cannot be incorporated into the crystal, crystal thickness  $L_c$  for EOC60 in Table 7 is calculated by the Equation (92b). Constants  $T_{sw}^c$  and  $T_{sw}^h$  in Table 7 determine the switching temperatures at cooling and heating, respectively.

The obtained values of crystal folds  $f$  (Table 7) indicate that according to the basic theoretical assumptions presented in Section 4.2.2., the chain axis  $c$  of folded-chain crystals in HDPE ( $f = 4$ ) makes the acute but larger angle with the stretch direction than that in EOC30 ( $f = 2$ ), whereas the extended-chain crystals in EOC60 are oriented parallel to the applied force. These results well correlate with the orientation of the chain axis  $c$  calculated on the basis of WAXS images of PEs under study listed in Table 5. In addition, this supports the statement that the anomalous elongation of cross-linked semicrystalline polymers under

constant load during non-isothermal crystallization is possible only when the  $c$ -axis of crystals is oriented parallel to the applied external force or makes a relatively small angle with it. Besides, the values of switching temperatures  $T_{sw}^c$  and  $T_{sw}^h$  are almost the same as the crystallization and melting temperatures  $T_c$  and  $T_m$  of the stretched samples of all PEs received from DSC and listed in Table 2. This additionally proves the hypothesis that exactly the crystallization of preliminarily drawn covalent network is responsible for the two-way shape-memory phenomenon. Moreover, the magnitudes of crystallinity  $\chi_{cf}$ , at which covalent network reaches the state with the lowest free energy (Table 7), surprisingly well correspond to the enthalpy-based crystallinity values determined from DSC in the first heating run of stretched samples (Table 2). Also, the crystal thickness  $L_c$  calculated on the basis of fitting parameters (Table 7) well coincides with the magnitudes  $L_c$  calculated from SAXS, which are listed in Table 6.

Fitting results show that the contribution of entangled slipped molecular chains (parameter  $\varepsilon_{01}$  in Table 7) to the total strain during the two-way SME is relatively small for all PEs under study. The consideration of this contribution provides more accurate modeling the experimental data, especially in the temperature range before the appearance of the anomalous elongation at cooling and after shape-memory recovery at heating. The values of material parameters of viscoelastic deformation of entangled macromolecules, such as the density of entangled slipped molecules  $\nu_e$ , the activation volume  $V_h$ , and the volume of flowing molecular chains  $V_h$  are higher for EOC30 and EOC60 as compared to HDPE that is expected because of the existence of short-chain branches.

### **6.6.2. Influence of loading**

Modeling the change of the crystal morphology of HDPE during the two-way shape-memory behavior under different loads is based on the calculation of the free energy of crystallization  $\Delta F_f(T, \lambda)$  as a function of temperature and draw ratio given by Equation (65). Values for the parameters in Equation (65) were the same as presented above. The results are shown in Figure 28. As before, the number of chain links  $N = 630$  was chosen so that it is in accordance with the crosslink density of HDPE  $\nu_c = 110 \text{ mol}\cdot\text{m}^{-3}$  listed in Table 1.

Furthermore, the ranges of draw ratio  $\lambda$  in Figure 28a–d were selected to correspond to the findings of the temperature dependent strain (Figure 16a, *Section 6.3.1.*) obtained experimentally in the course of non-isothermal crystallization of HDPE loaded by 0.9, 1, 1.1, and 1.2 MPa, respectively. Such a data representation enables the theoretical analysis of the



crystal structure and its orientation formed in HDPE during the two-way shape-memory experiments described in *Section 6.3.1.* and shown in Figure 16a. Note that  $\Delta F_f(T, \lambda)$  values of crystallites with numbers of folds  $f = 3$  and  $f > 4$  are greater than those presented in

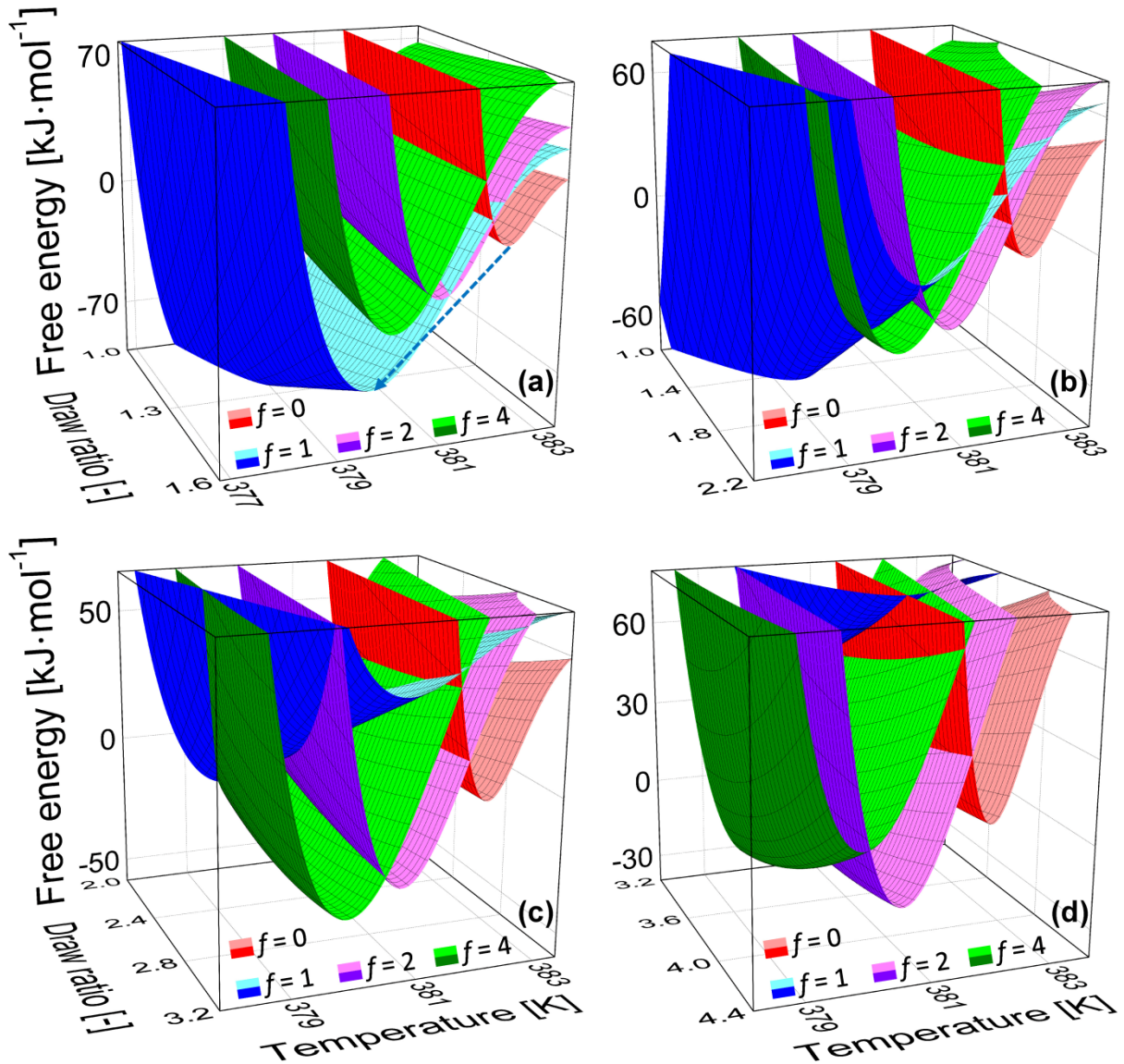


**Figure 28:** The free energy of crystallization  $\Delta F_f(T, \lambda)$  as a function of temperature and draw ratio calculated for HDPE with  $v_c = 110 \text{ mol}\cdot\text{m}^{-3}$  in case of different numbers of crystal folds  $f$ . The ranges of stretching correspond to the temperature dependent strain obtained experimentally for HDPE (Figure 16a) during the two-way shape-memory experiments under constant stress of 0.9 MPa (a), 1 MPa (b), 1.1 MPa (c), and 1.2 MPa (d). Blue dashed arrow in figure (a) serves as an example of common tangent line and indicates the crystallization path at cooling.

Figure 28 and therefore they are not shown.

The results indicate that whatever initial stretching is, the extended-chain crystallites ( $f = 0$ ) oriented parallel to the applied force possess a lower free energy at the onset of crystallization, whereas further cooling results in forming the folded-chain crystals oriented perpendicular ( $f = 1$ , Figure 28a) or nearly parallel ( $f = 2$  or 4, Figure 28b–d) to the stretch direction. These important theoretical findings will be used further to analyze the results of fitting. Also, the structural change from 4-fold to 2-fold crystals induced by increasing draw ratio (Figure 28c–d) points to a rise of crystallization temperature, since a minimum of  $\Delta F_2(T, \lambda)$  occurs at higher temperature than a minimum of  $\Delta F_4(T, \lambda)$ . Such a tendency completely correlates with the experimentally obtained rise of switching temperature  $T_{sw}^c$  with increasing load during the two-way SME in HDPE (Table 2) that additionally proves the correctness of the derived theoretical description.

Fitting the thermo-mechanical response during the two-way shape-memory cycle was performed on the basis of equations (75) and (84) using the experimental findings of HDPE at

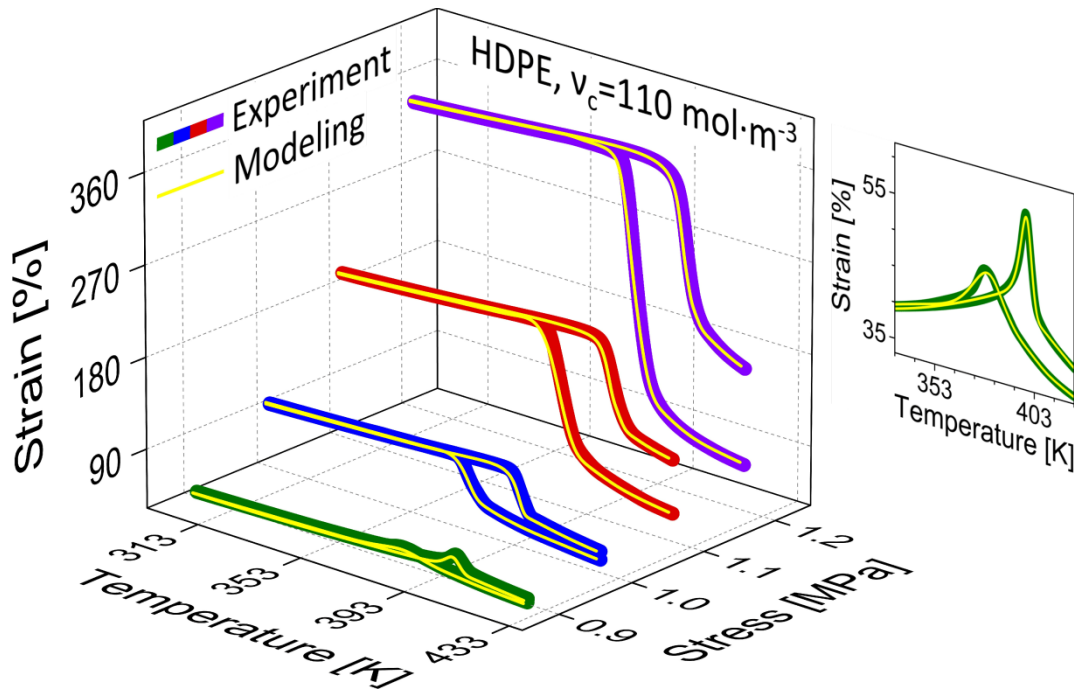


**Figure 29:** The experimental (bold) and fitting (thin yellow) curves of the two-way shape-memory behavior of HDPE with the crosslink density  $\nu_c = 110 \text{ mol}\cdot\text{m}^{-3}$  under different loads. The insert (right) enlarges the fitting of the thermo-mechanical response of HDPE loaded by 0.9 MPa.

**Table 8:** Influence of loading on relevant fitting and material parameters obtained for HDPE with the crosslink density  $\nu_c = 110 \text{ mol}\cdot\text{m}^{-3}$  and number of chain links  $N = 630$ .

$\sigma_{0N}$	$\varepsilon_{01}$	$\nu_e$	$V_h$	$V_m$	$U$	$f$	$\chi_{c0}$	$\chi_{cf}$	$T_{sw}^c$	$T_{sw}^h$
[MPa]	[%]	[ $\text{mol}\cdot\text{m}^{-3}$ ]	[ $\text{nm}^3$ ]	[ $10^3\cdot\text{nm}^3$ ]	[ $\text{kJ}\cdot\text{mol}^{-1}$ ]	[-]	[%]	[%]	[K]	[K]
0.9	2.7	88.2	2.1	4.1	105.4	1	3.3	54.4	377.8	397.9
1	5.2	89.5	2.1	4.2	105.7	4	2.3	57.4	375.8	396.6
1.1	9	88.9	2.1	4.5	108.7	4	1.5	58.1	383.8	402.6
1.2	28	89.7	2.2	4.6	109.4	2	1.1	61.5	384.1	403.9

different loads obtained as described in *Section 6.3.1*. The results are presented in Figure 29. The values of fitting and the material parameters are listed in Table 8. As can be seen in Figure 29, the used theoretical description demonstrates the extremely good coincidence with the experimental data.

Moreover, the presented theory allows describing even the peculiar mechanical behavior of HDPE loaded by 0.9 MPa (Figure 29, insert), which does not show the typical two-way SME. Based on the fitting results and the analysis of the free energy of crystallization illustrated in Figure 28a, it can be concluded that the specific thermo-mechanical response of HDPE at 0.9 MPa is caused by forming extended-chain crystallites with the  $c$ -axis lying in the stretch direction at the onset of crystallization, while at later stages of crystallization the extended-chain crystals transform into “one-fold crystals” oriented perpendicular to the direction of draw. Obviously, these different cases of crystal orientation lead to dramatically different mechanical behavior of the crystallizing covalent network. Indeed, as it is clearly seen from Figure 29 (insert), HDPE loaded by 0.9 MPa rapidly elongates at the beginning of crystallization, whereas further cooling results in the pronounced sample contraction within the temperature range of crystallization. The same behavior is observed at subsequent heating of the sample. On the contrary, according to the theoretical predictions, both extended- and folded-chain crystals with even number of folds ( $f = 2, 4$ ) oriented parallel or nearly parallel to the stretch direction should cause the elongation of pre-drawn covalent polymer network during non-isothermal crystallization. This is explicitly confirmed by fitting results obtained for typical well distinct two-way shape-memory curves of HDPE at 1, 1.1, and 1.2 MPa as shown in Figure 29 and Table 8.

As it follows from Table 8, the magnitudes of strain stored by entangled slipped molecules  $\varepsilon_{01}$  markedly increase with increasing load that is an evidence of rising involvement of viscoelastic deformation in the two-way shape-memory behavior. Though the contribution of entangled slipped molecular chains to the total strain during the two-way SME is relatively small, it provides more precise modeling the experimental behavior, especially in the temperature range before the appearance of the anomalous elongation at cooling and after shape-memory recovery at heating, as it also follows from the results of fitting presented in *Section 6.6.1*. Furthermore, the crystallinity values at which crystallization ceases  $\chi_{cf}$  gain with increasing load. This tendency is normally expected due to increasing initial strain  $\varepsilon_{ini}$  of HDPE (Table 3) and, consequently, higher ordering of polymer chains already in the amorphous state. The enthalpy-based crystallinity of undeformed and drawn HDPE calculated from DSC and listed in Table 2 confirms these fitting results. Additionally, a rise of crystallinity with increasing stretching observed experimentally in HDPE has been previously reported as well [115].

Besides, the activation energy values  $U$  increase with increasing load. Apparently, the cause of such a trend is that crystallization/melting of the covalent network suppresses/induces to some extent slipping of the entangled macromolecules. Since both crystallization and melting temperatures of HDPE rise with increasing load, as discussed in *Section 6.3.1.*, the viscous flow of the entangled macromolecules also occurs at higher temperatures and requires higher activation energy.

The received values of fitting parameters allow calculating the angle  $\varphi_{c,Z}$  between the  $c$ -axis of folded-chain crystals formed at cooling in the course of the two-way shape-memory experiment and the stretch direction  $Z$  as follows:

$$\varphi_{c,Z} = \tan\left(\frac{f \cdot a_0}{\zeta \cdot b_0}\right) = \tan\left(\frac{f \cdot (f+1) \cdot a_0}{N \cdot \chi_{cf} \cdot b_0}\right). \quad (93)$$

The calculated magnitudes of  $\varphi_{c,Z}$  along with those obtained from WAXS (Table 5) are plotted in Figure 30 as a function of applied stress. The difference between calculated and experimentally obtained  $\varphi_{c,Z}$  values is explained by the rather wide molecular weight distribution of HDPE (Table 1) and the inhomogeneous distribution of crosslink points as mentioned in *Section 5.1.*, whereas the theory was derived in case of monodisperse network chains.

However, both dependences of  $\varphi_{c,Z}$  on the applied stress change *quasi-discretely* with increasing load. Such a distinct correlation evinces that stronger orientation of  $c$ -axis towards

the stretch direction arises not only from rotating the crystals but also from the change of crystal structure that, correspondingly, results in elevated values of strain increment/decrement  $\Delta\varepsilon_{inc}/\Delta\varepsilon_{dec}$  and of the two-way shape-memory effectiveness factor  $\gamma_{eff}$ , especially for HDPE at 1.2 MPa as discussed in *Section 6.3.1*. Indeed, according to Equation (60b) and to the results presented in Figure 28d and 29 as well as Table 8, loading by 1.2 MPa and respective initial stretching entails forming the crystals with 2 folds and increasing crystallinity that, consequently, leads to a considerable rise of crystal thickness as compared to HDPE at 1 and 1.1 MPa where crystallites consist of 4 folds. The increase of crystal thickness, obviously, causes the drastic rise of strain increment/decrement values during the two-way SME in HDPE loaded by 1.2 MPa (Table 3).

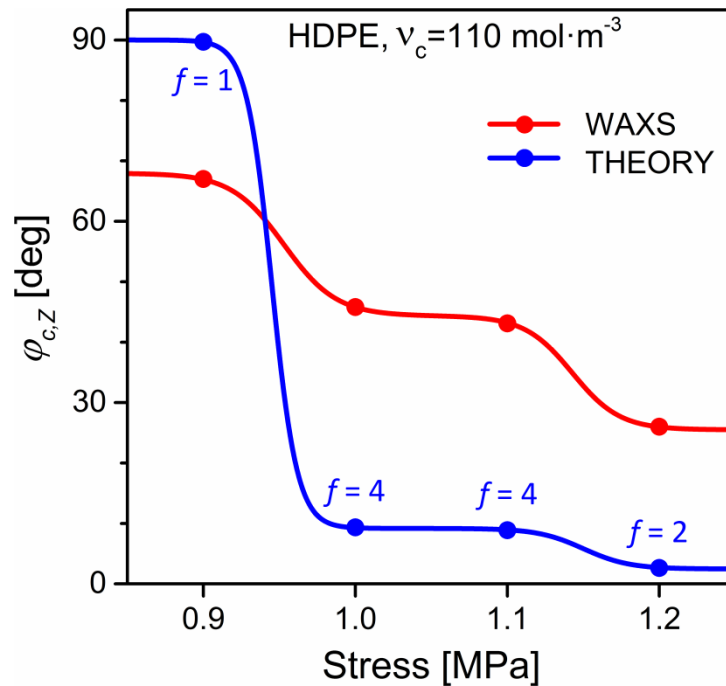


**Figure 30:** The calculated (blue dots and line) from fitting parameters and obtained experimentally from WAXS (red dots and line) values of the angle between the c-axis of crystals formed at cooling during the two-way SME in HDPE and the stretch direction Z as a function of applied constant stress.

It has to be mentioned, that in fact it is difficult to verify the real number of folds formed in a network chain, since the experimental investigation of the crystal structure in stretched

HDPE performed in the framework of this work (Figure 19) and before [119,123] predominantly discloses lamellae, which comprise the folded-chain crystallites formed in *numerous* neighboring network chains. Therefore, the theoretical assumption that the number of crystal folds strictly correlates with the orientation of crystals formed in the pre-drawn covalent network has been previously interpreted rather as a formalism enabling the consideration of different cases of the crystal orientation related to the applied external force. However, the findings demonstrated in Figure 30 prove the consistency and correctness of the aforementioned theoretical assumption as the change of number of crystal folds predicted theoretically evidently reflects the change of crystal structure formed at cooling during the two-way SME in HDPE loaded by different stresses. Such an important conclusion serves as a reliable evidence that the theory of the two-way SME derived in this work captures the key features of the thermo-mechanical behavior of the covalent polymer network under load in the course of non-isothermal crystallization and melting as well as clearly discloses the physical mechanism underlying the two-way shape-memory behavior of cross-linked polymeric materials.

## 7. Application aspects

The results presented in this work prove a high potential of both linear high-density and short-chain branched PEs for manifold practical applications as stimuli-responsive sensors and actuators. So, due to sufficiently high storage modulus and remarkably large reversible cyclic actuation, HDPE, EOC30, and shape-memory composites on their basis can advantageously replace traditional self-deploying techniques or even shape-memory alloys currently using in deployable structures in space engineering. In particular, HDPE- and EOC30-based shape-memory actuators can be used as sought [9,14] actively moving elements of solar sails and arrays, deployable reflector systems, spring-lock trusses for large boom structures, nano-rover wheels, chassis, rods, tubes, etc. Furthermore, as shown in *Sections 6.2.* and *6.3.*, a variation of both degree of branching and crosslink density results in a considerable change of switching temperatures of PEs under study from about 400 to 310 K that provides a broad range of their space applications to requirements.

Also, another high-tech application involves the use of cross-linked HDPE and EOC30 for aircraft morphing, e.g. folding, wings. Thereupon, shape-memory PEs could serve as a skin material that recovers its initial shape when heated above the switching temperature, whereby it sets in motion the underlying structural elements and the wings take the shape I. When the stimulus is terminated and temperature is lowered below the switching point, a skin returns to the temporary shape while the wings become of the shape II. In order to thermally activate the shape-memory skin, conductive wire springs embedded in the PEs matrix can be the case [14]. Here, an electrical current passed through the conductive wire springs actuates such PEs-based shape-memory composite by direct Joule heating.

Though EOC60 demonstrates lower values of storage modulus below crystallization temperature, decreased reversible deformation and the specific work done against the external load as compared to HDPE and EOC30, it can nevertheless find applications in smart textile and various micro-electromechanical systems as fine sensor and actuator. Thus, cross-linked EOC60 in this connection can be used in liquid cooling systems designed to remove waste heat produced by such components of integrated circuits as central processing unit (CPU), chipset, etc. So, heating above the CPU critical temperature associated with the switching temperature of EOC60-based couplings results in the reversible actuation of the latter, which allows a cold fluid (water) to pass in the cooling system and to reduce the CPU temperature by convective heat transfer. In the meantime, a reduction of the CPU temperature is

accompanied by lowering the temperature of EOC60-based couplings below the switching point. Thereby shape-memory couplings return to the initial “locked” state and prevent further cooling the CPU maintaining its appropriate temperature regime.

In addition, confirmed biocompatibility of PE [124] enables its smart application in medicine as elements for drug-delivery systems, biomedical devices, thermo-responsive stents, catheters, implants, sutures, etc. Because the switching temperature of EOC60 at cooling amounts about 310 K (*Section 6.3.*) and is close to human body temperature, cross-linked highly-branched PEs seem to be rather applicable in the biomedical use than HDPE and medium-branched ethylene-copolymers.

Generally, cross-linked PEs can find applications in many other areas, where mechanical actuation is required. The remarkable ability of PEs under study to reversible cyclic thermally responsive deformation and to perform useful work against external forces, as it was proved in the framework of this work, can potentially be used in designing various heat engines and energy storage devices. The particularly interesting material in this regard is HDPE able to store large amounts of energy and to perform exceedingly high mechanical work of about  $1.8 \text{ MJ}\cdot\text{m}^{-3}$ . Finally, low costs and well-developed processing make cross-linked HDPE and EOCs especially attractive shape-memory materials for industrial scale production.

Based on the experimental and theoretical results presented in this work, it can be given some directions for further optimization of the appearance of the two-way SME. Firstly, the distinct step-like change of deformation of PEs during cooling and heating stages of the two-way shape-memory experiment occurs rather for monodisperse network chains. Therefore, crystallizable polymers with narrow molecular weight distribution are preferable to observe the two-way SME. Besides, cross-linking via high energy electrons irradiation ensures more homogeneous distribution of crosslink points than that via peroxide that results in narrower molecular weight distribution of chains in a covalent polymer network, i.e. enhanced monodispersity of network chains. Secondly, as it follows from modeling the crystal morphology of pre-drawn crystallized covalent network supported by the experimental investigation of the two-way SME in PEs, higher crosslink density  $\nu_c$  enables an occurrence of the two-way shape-memory behavior under lower load and its better reproducibility. However, values of strain increment  $\Delta\varepsilon_{inc}$  and decrement  $\Delta\varepsilon_{dec}$  caused by non-isothermal crystallization and melting, respectively, in this case are decreased too as compared to PEs having lower  $\nu_c$  magnitudes and being subjected to the same load. Thus, each special case of the application of shape-memory polymers requires a precise link between processing conditions as well as structural parameters of materials, on the one hand, and their shape-



memory properties, on the other hand. Such a link gives a theory of the two-way SME developed in this work. So, the stress-strain-temperature relationships given by equations (72) and (81) can advantageously be used to model the two-way shape-memory performance of a crystallizable covalent network in order to determine processing conditions needed to get desired shape-memory properties. Nevertheless, a general condition for the observation of pronounced two-way SME is sufficiently high crystallinity of a sample.

Note that the theoretical description presented in this work was derived for a general case of cross-linked semicrystalline polymer. Therefore, the theory can be applied to model the one- and two-way shape-memory behavior of other crystallizable polymer networks. In particular, PCL attracts a special attention here as promising shape-memory material for likely biomedical applications due to its relatively high crystallinity, biocompatibility and biodegradability [2,49–50,54].

Although the developed theoretical approach was used to model the two-way SME in such single polymers as HDPE, EOC30, and EOC60, it opens broad prospects for modeling the shape-memory phenomena in cross-linked blends of crystallizable polymers. First of all, the theoretical approach derived in this work is accurate, physically grounded, and focused on the

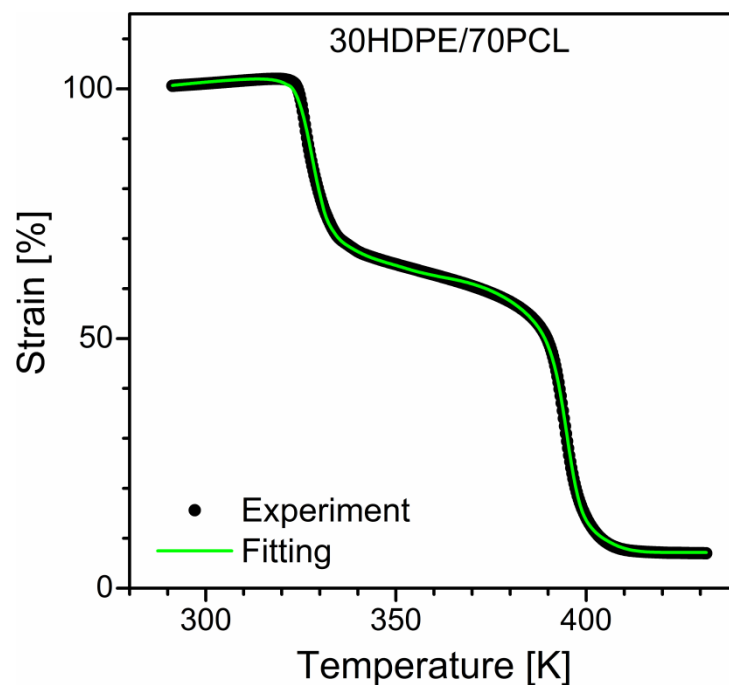


**Figure 31:** Experimental and fitting curves of multiple one-way shape-memory recovery obtained for 30HDPE/70PCL blend cross-linked by 1.3 wt% DHBP [32].

fundamental molecular mechanisms, which are involved in the two-way shape-memory behavior of both single polymers and polymer blends. In order to model the shape-memory performance of polymer blends on the basis of presented theory, an account of interaction of blend components, phase morphology, and its appropriate theoretical description are only needed. A potential of the present theoretical approach in modeling the one-way multiple shape-memory behavior of heterogeneous covalent networks was verified for 30HDPE/70PCL blend cross-linked by 1.3 wt% DHBP [32]. As it is seen from Figure 31, the fitting curve very good coincides with the experimental findings. This encourages further development of the theoretical description of shape-memory materials on the basis of polymer blends, which can point the operating ways to improve shape-memory behavior of polymer networks by means of tailoring their structure and morphology.

## 8. Summary

The present work focuses on the theoretical and experimental analysis of the two-way invertible shape-memory behavior of cross-linked linear high-density and short-chain branched PEs. A strong accent was placed on the appearance and origin of the principal manifestation of the two-way SME – the anomalous elongation of the samples under constant load initiated by non-isothermal crystallization at cooling and the following contraction triggered by melting of the crystalline phase at heating. The special attention was given to the morphology and orientation of the crystal structure generated in covalent networks of PEs under constant load in the course of non-isothermal crystallization at cooling.

The theory explaining the origin of the two-way SME in cross-linked semicrystalline polymers was developed on the basis of three-element mechanical model by taking into consideration the viscoelastic deformation of entangled slipped molecules and crystallization/melting of covalent polymer network as two basic mechanisms involved in the shape-memory performance. However, it was emphasized that crystallizing/melting covalent network plays a key role in the two-way SME being suggested responsible for both the anomalous elongation and successive contraction of a sample under loaded during non-isothermal crystallization at cooling. Based on the theory of stress-induced crystallization it was derived a thermodynamic description of the thermo-mechanical behavior of pre-drawn crystallizable covalent network. The analysis of the free energy of crystallization derived herein enabled prediction of the crystal structure and the orientation of crystals generated in covalent network in case of different number of chain links and applied deformation. It was determined that the anomalous elongation during the two-way SME is only possible when the orientation of crystals formed at cooling is such that crystal chains are parallel to the direction of the external force or make an acute angle with it.

The influence of loading on the two-way shape-memory performance was analyzed in cross-linked linear high-density and short-chain branched PEs. The analysis of the experimental data of the two-way SME enabled introduction and estimation of such important characteristics of the two-way shape-memory behavior as initial strain at loading  $\varepsilon_{ini}$ , crystallization- and melting-induced strain increment  $\Delta\varepsilon_{inc}$  and decrement  $\Delta\varepsilon_{dec}$ , respectively, the two-way shape-memory effectiveness  $\gamma_{eff}$  and two-way shape-memory recovery  $\gamma_{rec}$  factors. Based on the obtained results, it was determined that the two-way

shape-memory performance of covalent polymer networks essentially depends on the applied stress  $\sigma_{0N}$  and markedly increases with increasing  $\sigma_{0N}$  for all PEs under study, but in particular for HDPE revealing remarkable  $\Delta\varepsilon_{inc}$ ,  $\Delta\varepsilon_{dec}$  and  $\gamma_{eff}$  values. Furthermore, a rise of load results in an elevated kinetics of the two-way SME, in other words, higher stress causes both faster elongation of a sample at cooling and faster contraction at heating. The specific work  $W_{sp}$  done by a sample against external force in the course of the two-way shape-memory recovery also rises with increasing load indicating great potential of PEs to store mechanical energy and to be used as thermally induced actuators. Particular attention in this connection should be drawn to HDPE able to realize extremely high mechanical work of about  $1.8 \text{ MJ}\cdot\text{m}^{-3}$ . In the meantime, though EOC60 possesses relatively low  $W_{sp}$  values in comparison with HDPE, it demonstrates the pronounced two-way SME already at 0.15 MPa having a high effectiveness factor  $\gamma_{eff}$  of 0.95. In addition, because of much lower switching temperatures as compared to HDPE, EOC60 is also promising material that could find various engineering, medical, and other applications.

The study of the effect of crosslink density  $\nu_c$  on the two-way shape-memory behavior of short-chain branched PEs along with results described above allowed concluding that:

- good perfection of covalent networks in EOC30 and EOC60 can be achieved even at crosslink densities of  $140$  and  $120 \text{ mol}\cdot\text{m}^{-3}$ , respectively;
- crosslink density  $\nu_c$  strongly affects the two-way shape-memory performance of covalent polymer networks, which rises with increasing  $\nu_c$  values;
- crystallinity  $\chi_c$  of a sample plays a crucial role in the two-way shape-memory performance, since  $\chi_c$  magnitude mainly determines both the capacity to reveal the two-way SME and the ability of covalent network to realize useful work in the course of the two-way shape-memory experiment;
- the two-way shape-memory effectiveness  $\gamma_{eff}$  and recovery  $\gamma_{rec}$  factors are essential and properly introduced parameters because they strongly reflect the productivity and perfection of covalent polymer network, correspondingly.

Besides, strong correlation between dependencies of the switching temperatures and crystallization/melting temperatures on  $\nu_c$  additionally confirms that exactly crystallization and melting are responsible for the principal manifestation of the two-way SME.

The crystallization/melting behavior, morphology, size, and orientation of crystals formed during non-isothermal crystallization under constant load were systematically investigated in

cross-linked linear high-density and short-chain branched PEs. TEM study showed that drawn samples of HDPE and medium branched EOC30 crystallized under load during cooling stage of the two-way shape-memory cycle contain lamellae with basal surface oriented nearly perpendicular to the stretch direction, whereas the crystalline phase of highly-branched EOC60 consists of small crystallites. SAXS findings of long period accompanied by enthalpy-based crystallinity values determined from DSC enabled calculating the crystal thickness of both undeformed and drawn PEs under study.

WAXS revealed preferred orientation of crystal chains in loaded PEs under study stretched nearly to the same extent of about 90–100% after crystallization in the course of the two-way shape-memory experiment. As determined, the  $c$ -axis of the unit cell in HDPE at 1 MPa and EOC30 at 0.6 MPa makes an angle of approximately  $46^\circ$  and  $35^\circ$  with the applied force, while  $c$ -axis in EOC60 at 0.3 MPa lies parallel to the stretch direction. Besides, HDPE was chosen to study an evolution of the orientation of the crystals formed at cooling under different loads. Thereby, it was found that uniform increase of applied constant stress results in *quasi-discrete* change of the orientation of the  $c$ -axis of folded-chain crystals in stretched HDPE.

Modeling the two-way SME performed for HDPE and EOCs on the basis of derived theoretical approach revealed excellent coincidence between fitted curves and experimental findings. The material parameters obtained by fitting allowed calculating the thickness of crystals, which very well correspond to those received from SAXS. The theoretical conclusions on crystal morphology of cross-linked linear and short-chain branched PEs were qualitatively confirmed on the basis of experimental results received from TEM.

The two-way SME in HDPE under different loads was modeled as well. The fitting curves demonstrated excellent accordance with experimental findings. Moreover, the theoretical analysis enabled consistent explanation of the peculiar thermo-mechanical behavior of HDPE loaded by 0.9 MPa in terms of crystal structure and its orientation. The fitting parameters were used to calculate the angle  $\varphi_{c,Z}$  between the  $c$ -axis of the unit cell and the stretch direction  $Z$ . The distinct correlation between calculated and obtained from WAXS  $\varphi_{c,Z}$  values pointed out that quasi-discrete change of the orientation of the chain axis  $c$  with increasing load arises from the change of crystal structure. The received results confirmed the correctness of the developed theory and its high potential in qualitative and quantitative description of the two-way SME in cross-linked semicrystalline polymers.

---

## References

---

1. Kleinhans, G.; Starkl, W.; Nuffer, K. Structure and mechanical properties of shape memory polyurethane. *Kunststoffe* **74**, 445–449 (1984).
2. Lendlein, A.; Schmidt, A.; Langer, R. AB-polymer networks based on oligo( $\epsilon$ -caprolactone)-segments showing shape-memory properties. *Proc. Natl. Acad. Sci. U.S.A.* **98** (3), 842–847 (2001).
3. Mather, P.T.; Luo, X.; Rousseau, I.A. Shape memory polymer research. *Annu. Rev. Mater. Res.* **39**, 445–71 (2009).
4. Ölander, A. An electrochemical investigation of solid cadmium-gold alloys. *J. Am. Chem. Soc.* **54** (10), 3819–3833 (1932).
5. Chang, L.C.; Read, T.A. Plastic deformation and diffusionless phase changes in metals – the gold-cadmium beta phase. *Trans. AIME*, **189**, 47–52 (1951).
6. Buehler, W.J.; Gilfrich, J.W.; Wiley, R.C. Effect of low-temperature phase changes on the mechanical properties of alloys near composition TiNi. *J. Appl. Phys.* **34** (5), 1475–1477 (1963).
7. Otsuka K.; Wayman C.M. Shape memory materials. Cambridge University Press, Cambridge CB2 1RP, UK (1998).
8. Lendlein, A.; Kelch, S. Shape-memory polymers. *Angew. Chem. Int. Ed.* **41** (12), 2034–2057 (2002).
9. Liu, C.; Qin, H.; Mather, P.T. Review of progress in shape-memory polymers. *J. Mater. Chem.* **17**, 1543–1558 (2007).
10. Behl, M.; Lendlein, A. Shape-memory polymers. *Mater. Today* **10** (4), 20–28 (2007).
11. Behl, M.; Lendlein, A. Actively moving polymers. *Soft Matter* **3** (1), 58–67 (2007).
12. Rousseau, I.A. Challenges of shape memory polymers: A review of the progress toward overcoming SMP's limitations. *Polym. Eng. Sci.* **48** (11), 2075–2089 (2008).
13. Leng, J.; Lu, H.; Liu, J.; Huang, W.M.; Du, S. Shape-memory polymers – A class of novel smart materials. *MRS Bulletin* **34** (11), 848–855 (2009).
14. Leng, J.; Du, S. Shape memory polymers and multifunctional composites. CRC Press, Boca Raton, USA (2010).
15. Huang, W.M.; Zhao, Y.; Wang, C.C.; Ding, Z.; Purnawali, H.; Tang, C.; Zhang, J.L. Thermo/chemo-responsive shape memory effect in polymers: a sketch of working mechanisms, fundamentals and optimization. *J. Polym. Res.* **19** (9), 9952 (2012).

- 
- 
16. Cho, J.W.; Kim, J.W.; Jung, Y.C.; Goo, N.S. Electroactive shape-memory polyurethane composites incorporating carbon nanotubes. *Macromol. Rapid Commun.* **26** (5), 412–416 (2005).
  17. Sahoo, N.G.; Jung, Y.C.; Cho, J.W. Electroactive shape memory effect of polyurethane composites filled with carbon nanotubes and conducting polymer. *Mater. Manuf. Process.* **22** (4), 419–423 (2007).
  18. Sahoo, N.G.; Jung, Y.C.; Yoo, H.J.; Cho, J.W. Influence of carbon nanotubes and polypyrrole on the thermal, mechanical and electroactive shape-memory properties of polyurethane nanocomposites. *Compos. Sci. Technol.* **67** (9), 1920–1929 (2007).
  19. Mohr, R.; Kratz, K.; Weigel, T.; Lucka-Gabor, M.; Moneke, M.; Lendlein, A. Initiation of shape-memory effect by inductive heating of magnetic nanoparticles in thermoplastic polymers. *Proc. Natl. Acad. Sci. U.S.A.* **103** (10), 3540–3545 (2006).
  20. Razzaq, M.Y.; Anhalt, M.; Frommann, L.; Weidenfeller, B. Thermal, electrical and magnetic studies of magnetite filled polyurethane shape memory polymers. *Mat. Sci. Eng. A – Struct.* **444** (1–2), 227–235 (2007).
  21. Razzaq, M.Y.; Anhalt, M.; Frommann, L.; Weidenfeller, B. Mechanical spectroscopy of magnetite filled polyurethane shape memory polymers. *Mat. Sci. Eng. A – Struct.* **471** (1–2), 57–62 (2007).
  22. Lendlein, A.; Jiang, H.Y.; Junger, O.; Langer, R. Light-induced shape-memory polymers. *Nature* **434**, 879–882 (2005).
  23. Yang, B.; Huang, W.M.; Li, C.; Lee, C.M.; Li, L. On the effects of moisture in a polyurethane shape memory polymer. *Smart Mater. Struct.* **13** (1), 191–195 (2004).
  24. Huang, W.M.; Yang, B.; An, L.; Li, C.; Chan, Y.S. Water-driven programmable polyurethane shape memory polymer: Demonstration and mechanism. *Appl. Phys. Lett.* **86** (11), 114105 (2005).
  25. Yang, B.; Huang, W.M.; Li, C.; Li, L. Effects of moisture on the thermomechanical properties of a polyurethane shape memory polymer. *Polymer* **47** (4), 1348–1356 (2006).
  26. Yang, B.; Huang, W.M.; Li, C.; Li, L.; Chor, J.H. Qualitative separation of the effects of carbon nano-powder and moisture on the glass transition temperature of polyurethane shape memory polymer. *Scripta Mater.* **53** (1), 105–107 (2005).

- 
- 
27. Leng, J.S.; Lv, H.B.; Liu, Y.J.; Du, S.Y. Comment on “water-driven programmable polyurethane shape memory polymer: Demonstration and mechanism” [Appl. Phys. Lett. 86, 114105, (2005)]. *Appl. Phys. Lett.* **92** (20), 206105 (2008).
  28. Li, F.; Chen, Y.; Zhu, W.; Zhang, X.; Xu, M. Shape memory effect of polyethylene/nylon 6 graft copolymers. *Polymer* **39** (26), 6929–6934 (1998).
  29. Li, F.; Zhu, W.; Zhang, X.; Zhao, C.; Xu, M. Shape memory effect of ethylene–vinyl acetate copolymers. *J. Appl. Polym. Sci.* **71** (7), 1063–70 (1999).
  30. Bellin, I.; Kelch, S.; Langer, R.; Lendlein, A. Polymeric triple-shape materials. *Proc. Natl. Acad. Sci. U.S.A.* **103** (48), 18043–18047 (2006).
  31. Behl, M.; Bellin, I.; Kelch, S.; Wagermaier, W.; Lendlein, A. One-step process for creating triple-shape capability of AB polymer networks. *Adv. Funct. Mater.* **19** (1), 102–108 (2009).
  32. Kolesov, I.; Dolynchuk, O.; Radusch, H.-J. Shape-memory behavior of cross-linked semi-crystalline polymers and their blends. *eXPRESS Polym. Lett.* **9** (3), 255–276 (2015).
  33. Luo, X.; Mather, P.T. Triple-shape polymeric composites (TSPCs). *Adv. Funct. Mater.* **20** (16), 2649–2656 (2010).
  34. Kolesov, I.S.; Radusch, H.-J. Multiple shape-memory behavior and thermal-mechanical properties of peroxide cross-linked blends of linear and short-chain branched polyethylenes. *eXPRESS Polym. Lett.* **2** (7), 461–473 (2008).
  35. Radusch, H.-J.; Kolesov, I.S.; Gohs, U.; Heinrich, G. Multiple shape-memory behavior of polyethylene/polycyclooctene blends cross-linked by electron irradiation. *Macromol. Mater. Eng.* **297** (12), 1225–1234 (2012).
  36. Cuevas, J.M.; Rubio, R.; German, L.; Laza, J.M.; Vilas, J.L.; Rodrigues, M.; Leon, L.M. Triple-shape memory effect of covalently crosslinked polyalkenamer based semicrystalline polymer blends. *Soft Matter* **8** (18), 4928–4935 (2012).
  37. Xie, T. Tunable polymer multi-shape memory effect. *Nature* **464**, 267–270 (2010).
  38. Zhao, J.; Chen, M.; Wang, X.; Zhao, X.; Wang, Z.; Dang, Z.-M.; Ma, L.; Hu, G.-H.; Chen, F. Triple shape memory effects of cross-linked polyethylene/polypropylene blends with cocontinuous architecture. *Appl. Mater. Interfaces* **5** (12), 5550–5556 (2013).



- 
- 
39. Bai, Y.; Zhang, X.; Wang, Q.; Wang, T. A tough shape memory polymer with triple-shape memory and two-way shape memory properties. *J. Mater. Chem. A* **2** (13), 4771–4778 (2014).
  40. Madbouly, S.A.; Lendlein, A. Degradable polyurethane/soy protein shape-memory polymer blends prepared via environmentally-friendly aqueous dispersions. *Macromol. Mater. Eng.* **297** (12), 1213–1224 (2012).
  41. Karger-Kocsis, J.; Keki, S. Biodegradable polyesterbased shape memory polymers: Concepts of (supra)molecular architecturing. *eXPRESS Polym. Lett.* **8** (6), 397–412 (2014).
  42. Ratna, D.; Karger-Kocsis, J. Recent advances in shape memory polymers and composites: A review. *J. Mater. Sci.* **43** (1), 254–269 (2008).
  43. Flory, P.J. Role of crystallization in polymers and proteins. *Science* **124** (3211), 53–60 (1956).
  44. Oth, J.F.M.; Flory, P.J. Thermodynamics of shrinkage of fibrous (racked) rubber. *J. Am. Chem. Soc.* **80** (6), 1297–1304 (1958).
  45. Mandelkern, L.; Roberts, D.E.; Diorio, A.F. Reversible contractile processes in fibrous macromolecules. *J. Am. Chem. Soc.* **80** (2), 500 (1958).
  46. Mandelkern, L.; Roberts, D.E.; Diorio, A.F.; Posner, A.S. Dimensional changes in systems of fibrous macromolecules: Polyethylene. *J. Am. Chem. Soc.* **81** (16), 4148–4157 (1959).
  47. Chung, T.; Romo-Uribe, A.; Mather, P.T. Two-way reversible shape-memory in a semicrystalline network. *Macromolecules* **41** (1), 184–192 (2008).
  48. Lee, K.M.; Knight, P.T.; Chung, T.; Mather, P.T. Polycaprolactone–POSS chemical/physical double networks. *Macromolecules* **41** (13), 4730–4738 (2008).
  49. Pandini, S.; Passera, S.; Messori, M.; Paderni, K.; Toselli, M.; Gianoncelli, A.; Bontempi, E.; Riccò, T. Two-way reversible shape memory behaviour of crosslinked poly( $\epsilon$ -caprolactone). *Polymer* **53** (9), 1915–1924 (2012).
  50. Pandini, S.; Baldi, F.; Paderni, K.; Messori, M.; Toselli, M.; Pilati, F.; Gianoncelli, A.; Brisotto, M.; Bontempi, E.; Riccò, T. One-way and two-way shape memory behaviour of semi-crystalline network based on sol-gel cross-linked poly( $\epsilon$ -caprolactone). *Polymer* **54** (16), 4253–4265 (2013).

- 
- 
51. Kolesov, I.; Dolynchuk, O.; Borreck, S; Radusch, H.-J. Morphology-controlled multiple one- and two-way shape-memory behavior of cross-linked polyethylene/poly( $\epsilon$ -caprolactone) blends. *Polym. Adv. Technol.* **25** (11), 1315–1322 (2014).
  52. Kolesov, I.S.; Kratz, K.; Lendlein, A.; Radusch, H.-J. Kinetics and dynamics of thermally-induced shape-memory behavior of crosslinked short-chain branched polyethylenes. *Polymer* **50** (23), 5490–5498 (2009).
  53. Kolesov, I.S.; Radusch, H.-J. Investigation on the performances of the peroxidic initiated network in shape-memory materials on the basis of ethylene-1-octene-copolymers and their blends with HDPE by means of deformation behavior and stress relaxation. “*Proceeding of 24th Annual Meeting of Polymer Processing Society (PPS-24). Salerno, Italy*”, S22-1184 (2008).
  54. Zotzmann, J.; Behl, M.; Hofmann, D.; Lendlein, A. Reversible triple-shape effect of polymer networks containing poly(pentadecalactone)- and poly( $\epsilon$ -caprolactone)-segments. *Adv. Mater.* **22** (31), 3424–3429 (2010).
  55. Basit, A.; L’Hostis, G.; Pac, M.J.; Durand, B. Thermally activated composite with two-way and multi-shape memory effects. *Materials* **6** (9), 4031–4045 (2013).
  56. Imai, S. Operating methods for two-way behavior shape memory polymer actuators without using external stress. *IEEJ Trans. Elec. Electron. Eng.* **9** (1), 90–96 (2014).
  57. Westbrook, K.K.; Mather, P.T.; Parakh, V.; Dunn, M.L.; Ge, Q.; Lee, B.M.; Qi, H.J. Two-way reversible shape memory effects in a free-standing polymer composite. *Smart Mater. Struct.* **20** (6), 065010 (2011).
  58. Wu, Y.; Hu, J.; Han, J.; Zhu, Y.; Huang, H.; Li, J.; Tang, B. Two-way shape memory polymer with “switch–spring” composition by interpenetrating polymer network. *J. Mater. Chem. A* **2** (44), 18816–18822 (2014).
  59. Behl, M.; Kratz, K.; Noechel, U.; Sauter, T.; Lendlein, A. Temperature-memory polymer actuators. *Proc. Natl. Acad. Sci. U.S.A.* **110** (31), 12555–12559 (2013).
  60. Behl, M.; Kratz, K.; Zotzmann, J.; Nöchel, U.; Lendlein, A. Reversible bidirectional shape-memory polymers. *Adv. Mater.* **25** (32), 4466–4469 (2013).
  61. Dolynchuk, O.; Kolesov, I.; Radusch, H.-J. Shape-memory actuators on the basis of binary and ternary blends of polyethylenes. “*Proceeding of 30th Annual Meeting of Polymer Processing Society (PPS-30). Cleveland, USA*”, S02-184 (2014).
  62. Tobushi, H.; Okumura, K.; Hayashi, S.; Ito, N. Thermomechanical constitutive model of shape memory polymer. *Mech. Mater.* **33** (10), 545–554 (2001).

- 
- 
63. Liu, Y.; Gall, K.; Dunn, M.L.; Greenberg, A.R.; Diani, J. Thermomechanics of shape memory polymers: Uniaxial experiments and constitutive modeling. *Int. J. Plasticity* **22** (2), 279–313 (2006).
  64. Barot, G.; Rao, I.J. Constitutive modeling of the mechanics associated with crystallizable shape memory polymers. *Z. angew. Math. Phys. ZAMP* **57** (4), 652–681 (2006).
  65. Barot, G.; Rao, I.J.; Rajagopal, K.R. A thermodynamic framework for the modeling of crystallizable shape memory polymers. *Int. J. Eng. Sci.* **46** (4), 325–351 (2008).
  66. Chen, Y.-C.; Lagoudas, D.C. A constitutive theory for shape memory polymers. Part I: Large deformations. *J. Mech. Phys. Solids* **56** (5), 1752–1765 (2008).
  67. Chen, Y.-C.; Lagoudas, D.C. A constitutive theory for shape memory polymers. Part II: A linearized model for small deformations. *J. Mech. Phys. Solids* **56** (5), 1766–1778 (2008).
  68. Qi, H.J.; Nguyen, T.D.; Castro, F.; Yakacki, C.M.; Shandas, R. Finite deformation thermo-mechanical behavior of thermally induced shape memory polymers. *J. Mech. Phys. Solids* **56** (5), 1730–1751 (2008).
  69. Husson, J.M.; Dubois, F.; Sauvat, N. A finite element model for shape memory behavior. *Mech. Time-Depend. Mat.* **15** (3), 213–237 (2011).
  70. Böl, M.; Reese, S. Micromechanical modelling of shape memory polymers. *Adv. Sci. Tech.* **54**, 137–142 (2008).
  71. Sinha, R.P.; Jarali, C.S.; Raja, S. Modelling the thermomechanical behaviour of shape memory polymer materials. *Indian J. Eng. Mater. S.* **18** (1), 15–23 (2011).
  72. Yu, K.; Xie, T.; Leng, J.; Ding, Y.; Qi, H.J. Mechanisms of multi-shape memory effects and associated energy release in shape memory polymers. *Soft Matter* **8** (20), 11098–11105 (2012).
  73. Ge, Q.; Yu, K.; Ding, Y.; Qi, H.J. Prediction of temperature-dependent free recovery behaviors of amorphous shape memory polymers. *Soft Matter* **8** (43), 5687–5695 (2012).
  74. Ge, Q.; Luo, X.; Rodriguez, E.D.; Zhang, X.; Mather, P.T.; Dunn, M.L.; Qi, H.J. Thermomechanical behavior of shape memory elastomeric composites. *J. Mech. Phys. Solids* **60** (1), 67–83, (2012).

- 
- 
75. Ge, Q.; Luo, X.; Iversen, C.B.; Mather, P.T.; Dunn, M.L.; Qi, H.J. Mechanisms of triple-shape polymeric composites due to dual thermal transitions. *Soft Matter* **9** (7), 2212–2223 (2013).
  76. Morshedian, J.; Khonakdar, H.A.; Rasouli, S. Modeling of shape memory induction and recovery in heat-shrinkable polymers. *Macromol. Theory Simul.* **14** (7), 428–434 (2005).
  77. Khonakdar, H.A.; Jafari, S.H.; Rasouli, S.; Morshedian, J.; Abedini, H. Investigation and modeling of temperature dependence recovery behavior of shape-memory crosslinked polyethylene. *Macromol. Theory Simul.* **16** (1), 43–52 (2007).
  78. Wang, Z.D.; Li, D.F.; Xiong, Z.Y.; Chang, R.N. Modeling thermomechanical behaviors of shape memory polymer. *J. Appl. Polym. Sci.* **113** (1), 651–656 (2009).
  79. Heuchel, M.; Cui, J.; Kratz, K.; Kosmella, H.; Lendlein, A. Relaxation based modeling of tunable shape recovery kinetics observed under isothermal conditions for amorphous shape-memory polymers. *Polymer* **51** (26), 6212–6218 (2010).
  80. Westbrook, K.K.; Parakh, V.; Chung, T.; Mather, P.T.; Wan, L.C.; Dunn, M.L.; Qi, H.J. Constitutive modeling of shape memory effects in semicrystalline polymers with stretch induced crystallization. *J. Eng. Mater. Technol.* **132** (4), 041010 (2010).
  81. Ghobadi, E.; Heuchel, M.; Kratz, K.; Lendlein, A. Simulating the shape-memory behavior of amorphous switching domains of poly(L-lactide) by molecular dynamics. *Macromol. Chem. Phys.* **214** (11), 1273–1283 (2013).
  82. Ghobadi, E.; Heuchel, M.; Kratz, K.; Lendlein, A. Influence of the addition of water to amorphous switching domains on the simulated shape-memory properties of poly(L-lactide). *Polymer* **54** (16), 4204–4211 (2013).
  83. Ghobadi, E.; Heuchel, M.; Kratz, K.; Lendlein, A. Atomistic simulation of the shape-memory effect in dry and water swollen poly[(*rac*-lactide)-*co*-glycolide] and copolyester urethanes thereof. *Macromol. Chem. Phys.* **215** (1), 65–75 (2014).
  84. Strobl, G.R. The physics of polymers: Concepts for understanding their structures and behavior. Springer, Berlin, Germany (2007).
  85. Wunderlich, B. Macromolecular physics: Crystal Nucleation, Growth, Annealing, Vol. 2. Academic Press, New York, USA (1976).
  86. Gedde, U.W. Polymer physics. Chapman & Hall, London, UK (1995).
  87. Treloar, L.R.G. The physics of rubber elasticity, 3rd ed. Clarendon Press, Oxford, UK (1975).

- 
- 
88. Krausz, A.S.; Eyring, H. Deformation kinetics. Wiley-Interscience, New York, USA (1975).
  89. Ziabicki, A. Theoretical analysis of oriented and non isothermal crystallization. *Colloid Polym. Sci.* **252** (3), 207–221 (1974).
  90. Kolesov, I.; Dolynchuk, O.; Radosch, H.-J. Modeling of shape-memory recovery in crosslinked semicrystalline polymers. *Adv. Sci. Tech.* **77**, 319–324 (2012).
  91. Kolesov, I.; Dolynchuk, O.; Radosch, H.-J. Theoretical description of unconstrained thermally induced shape-memory recovery in crosslinked polyethylenes. *J. Polym. Sci. B Polym. Phys.* **52** (12), 815–822 (2014).
  92. Dolynchuk, O.; Kolesov, I.; Radosch, H.-J. Thermodynamic description and modeling of two-way shape-memory effect in crosslinked semicrystalline polymers. *Polym. Adv. Technol.* **25** (11), 1307–1314 (2014).
  93. Dolynchuk, O.; Kolesov, I.; Radosch, H.-J. Theoretical description of an anomalous elongation during two-way shape-memory effect in crosslinked semicrystalline polymers. *Macromol. Symp.* **346** (1), 48–58 (2014).
  94. Gordeyev, S.A.; Ward, I.M. Time dependent recovery of oriented polyethylene. *J. Mater. Sci.* **34** (19), 4767–4773 (1999).
  95. Polyanin, A.D.; Zaitsev, V.F. Handbook of exact solutions for ordinary differential equations, 2nd ed. Chapman & Hall/CRC, Boca Raton, USA (2003).
  96. Gradshteyn, I.S.; Ryzhik, I.M. Table of integrals, series, and products (Eds.: Jeffrey, A.; Zwillinger, D.), 7th ed. Academic Press, Oxford, UK (2007).
  97. Hazewinkel, M.; Ed., Encyclopaedia of Mathematics, Vol. 5. Kluwer Academic Publishers, Dordrecht, Netherlands (1990).
  98. Gaylord, R.J.; Lohse D.J. Morphological changes during oriented polymer crystallization. *Polym. Eng. Sci.* **16** (3), 163–167 (1976).
  99. Gaylord, R.J. A theory of the stress-induced crystallization of crosslinked polymeric networks. *J. Polym. Sci. Polym. Phys. Ed.* **14** (10), 1827–1837 (1976).
  100. Wang, M.C.; Guth, E. Statistical theory of networks of non-gaussian flexible chains. *J. Chem. Phys.* **20** (7), 1144–1157 (1952).
  101. Ozawa, T. Kinetics of non-isothermal crystallization. *Polymer* **12** (3), 150-158 (1971).
  102. Mark, J. E.; Eds. Polymer Data Handbook. Oxford University Press, New York, USA (1999).

- 
- 
103. Flory, P.J.; Rehner, J. Statistical mechanics of cross-linked polymer networks I. Rubberlike elasticity. *J. Chem. Phys.* **11** (11), 512–520 (1943).
  104. Flory, P.J.; Rehner, J. Statistical mechanics of cross-linked polymer networks I. Swelling. *J. Chem. Phys.* **11** (11), 521–526 (1943).
  105. Sajkiewicz, P., Phillips, P.J. Peroxide crosslinking of linear low-density polyethylenes with homogeneous distribution of short chain branching. *J. Polym. Sci. A Polym. Chem.* **33** (5), 853–862 (1995).
  106. Smedberg, A.; Hjertberg, T.; Gustafsson, B. Effect of molecular structure and topology on network formation in peroxide crosslinked polyethylene. *Polymer* **44** (11), 3395–3405 (2003).
  107. Bensason, S.; Minick, J.; Moet, A.; Chum, S.; Hiltner, A.; Baer E. Classification of homogeneous ethylene-octene copolymers based on comonomer content. *J. Polym. Sci. B Polym. Phys.* **34** (7), 1301–1315 (1996).
  108. Wunderlich, B. The ATHAS database on heat capacities of polymers. *Pure Appl. Chem.* **67** (6), 1019–1026 (1995). ATHAS data bank <http://athas.prz.edu.pl/>, M. Pyda (Ed.) (2009).
  109. Mathot, V. B. F.; Scherenberg, R. L.; Pijpers, M. F. J.; Bras, W. Dynamic DSC, SAXS and WAXS on homogeneous ethylene-propylene and ethylene-octene copolymers with high comonomer contents. *J. Therm. Anal.* **46** (3–4), 681–718 (1996).
  110. Reiter, G.; Strobl, G.R.; Eds. Progress in Understanding of Polymer Crystallization. *Lect. Notes Phys.* **714**, Springer, Berlin Heidelberg, Germany (2007).
  111. Androsch, R. Melting and crystallization of poly(ethylene-co-octene) measured by modulated d.s.c. and temperature-resolved X-ray diffraction. *Polymer* **40** (10), 2805–2812 (1999).
  112. Androsch, R.; Wunderlich, B. A study of annealing of poly(ethylene-co-octene) by temperature modulated and standard differential scanning calorimetry. *Macromolecules* **32** (21), 7238–7247 (1999).
  113. Alizadeh, A.; Richardson, L.; Xu, J.; Marand, H.; Cheung, Y.W.; Chum, S. Influence of structural and topological constrains on the crystallization and melting behavior of annealing of polymers. 1. Ethylene/1-octene copolymers. *Macromolecules* **32** (19), 6221–6235 (1999).

- 
- 
114. Kolesov, I.S.; Androsch, R.; Radusch, H.-J. Non-isothermal crystallization of polyethylenes as function of cooling rate and concentration of short-chain branches. *J. Therm. Anal. Cal.* **78 (3)**, 885–895 (2004).
  115. Kitamaru, R.; Hyon, S.-H. Structure and properties of lightly crosslinked crystalline polymers crystallized or processed under molecular orientation. *J. Polym. Sci. Macromol. Rev.* **14 (1)**, 207–264 (1979).
  116. Minick, J.; Moet, A.; Hiltner, A.; Baer, E.; Chum, S.P. Crystallization of very low density copolymers of ethylene with  $\alpha$ -olefins. *J. Appl. Polym. Sci.* **58 (8)**, 1371–1384 (1995).
  117. Kolesov, I.S.; Androsch, R.; Radusch, H.-J. Effect of crystal morphology and crystallinity on the mechanical  $\alpha$ - and  $\beta$ -relaxation processes of short-chain branched polyethylene. *Macromolecules* **38 (2)**, 445–453 (2005).
  118. Alexander L.E. X-ray diffraction methods in polymer science, 2nd ed. Robert E. Krieger Publishing Company, Huntington, New York, USA (1979).
  119. Bowden, P.B.; Young, R.J. Deformation mechanisms in crystalline polymers. *J. Mater. Sci.* **9 (12)**, 2034–2051 (1974).
  120. Keller, A. Polymer single crystals. *Polymer* **3**, 393–421 (1962).
  121. Frank, F.C.; Tosi, M. On the theory of polymer crystallization. *Proc. R. Soc. Lond. A* **263 (1314)**, 323–339 (1961).
  122. Hoffman, J.D. Theoretical aspects of polymer crystallization with chain folds: Bulk polymers. *Polym. Eng. Sci.* **4 (4)**, 315–362 (1964).
  123. Young, R.J.; Bowden, P.B. The structure of high-density polyethylene with a single-crystal texture. *J. Mater. Sci.* **8 (8)**, 1177–1184 (1973).
  124. Final report on the safety assessment of polyethylene. *Int. J. Toxicol.* **26 (Suppl. 1)**, 115–127 (2007).

---

---

### **Declaration under Oath**

I declare under oath that this thesis is my own work entirely and has been written without any help from other people. I used only the sources mentioned and included all the citations correctly both in word or content. The thesis has not been previously submitted by me or any other at this or any other university in order to achieve an academic degree.

Merseburg, 27.05.2015

Oleksandr Dolynchuk



---

---

## CURRICULUM VITAE

### Personal information

*Name* *Oleksandr Dolynchuk*  
*Gender* *male*  
*Present academic degree* *M.Sc.*  
*Date of birth* *14.04.1987*  
*Place of birth* *Ternivka, Ukraine*  
*Nationality* *Ukraine*

### Academic profile

*2012–2015* *Ph.D. at Center of Engineering Sciences*  
*Martin Luther University Halle-Wittenberg, Germany*  
*Title: Experimental and theoretical description of two-way*  
*shape-memory behavior of cross-linked linear high-density*  
*and short-chain branched polyethylenes*

*2011–2012* *Visiting scientist at Center of Engineering Sciences*  
*(DAAD scholarship)*  
*Martin Luther University Halle-Wittenberg, Germany*

*2008–2009* *M. Sc. Solid State Physics (summa cum laude)*  
*Dnipropetrovsk National University, Ukraine*

*2004–2008* *B.Sc. Physics (summa cum laude)*  
*Dnipropetrovsk National University, Ukraine*

*1993–2004* *Elementary school and secondary education (summa cum laude)*